LUND UNIVERSITY

Development of Optically Communicating Nanowire-based III-V Devices

Optical broadcasting for artificial neural networks

Flodgren, Vidar

2025

Document Version:
Publisher's PDF, also known as Version of record

Development of Optically Communicating Nanowire-based III-V Devices

Optical broadcasting for artificial neural networks

ATLI VIDAR MÁR FLODGREN
DEPARTMENT OF PHYSICS | FACULTY OF SCIENCE | LUND UNIVERSITY

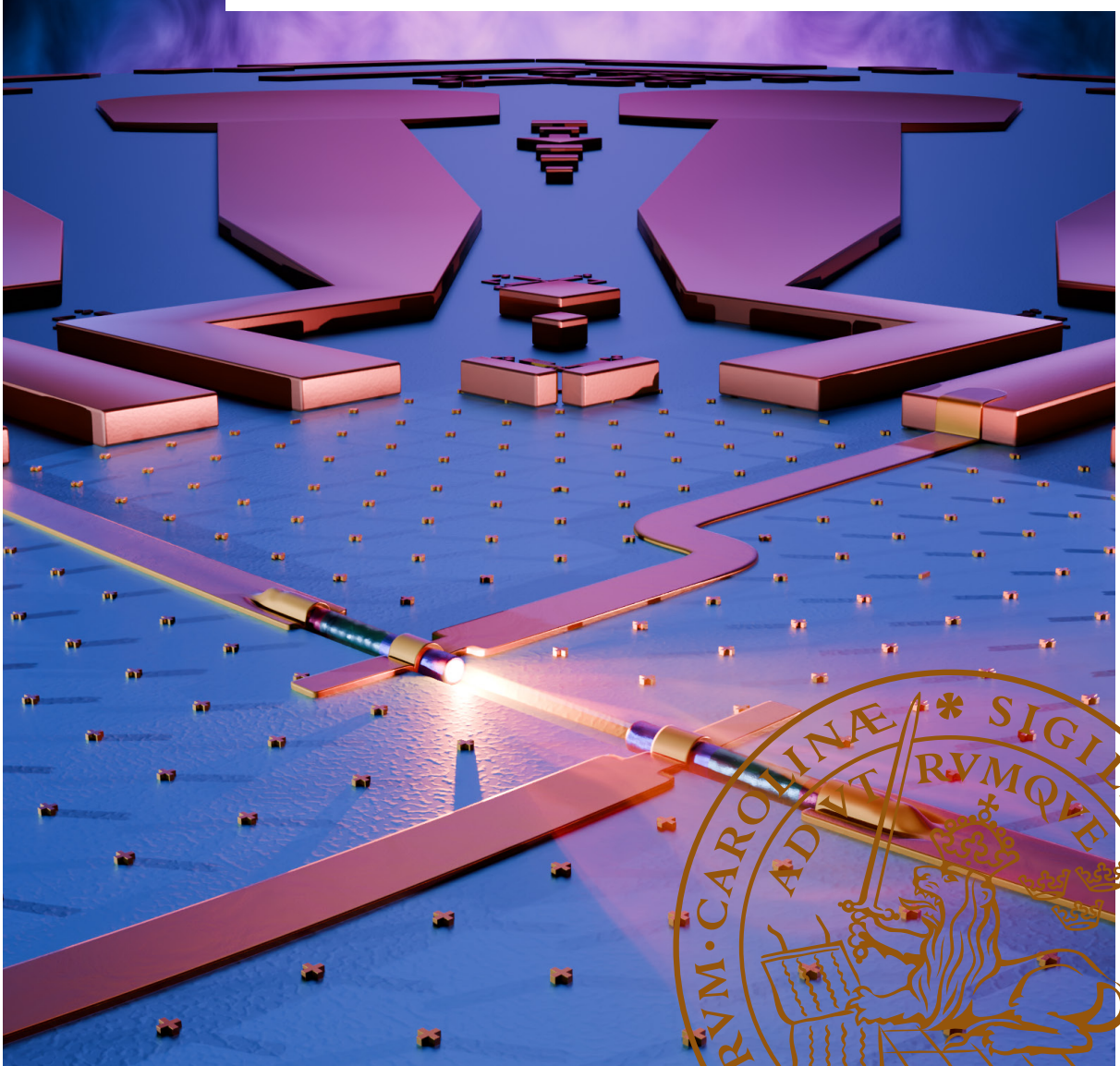

Development of Optically Communicating Nanowire-based III-V Devices

Optical broadcasting for artificial neural networks.

by Atli Vidar Már Flodgren

LUND
UNIVERSITY

Thesis for the degree of Doctor of Philosophy in Physics
Thesis advisors: Anders Mikkselsen, Cord Arnold, Heiner Linke, Edvin Lundgren
Faculty opponent: Michael J. Strain

To be presented, with the permission of the Faculty of Science of Lund University, for public criticism in the Rydberg lecture hall (Rydbergsalen) at the Department of Physics on Thursdady, the 12th of June 2025 at 13:15.

Organization
LUND UNIVERSITY

Department of Physics
Synchrotron Radiation Research
Box 118
SE-221 00 Lund, Sweden

Document name
DOCTORAL DISSERTATION

Date of disputation
2025-06-12

Sponsoring organization

Author(s)
Atli Vidar Már Flodgren

Title and subtitle
Development of Optically Communicating Nanowire-based III-V Devices:
Optical broadcasting for artificial neural networks.

Abstract
This thesis presents the development and study of a flexible and Silicon-chip compatible integration of III–V nanowire (NW) optoelectronic components in network circuits, where communication is done via the broadcasting of light signals. This includes an investigation into how neural processing behaviours can be emulated using on-chip photonic circuits. Both experimental works that demonstrate the first on-chip communication between nano-optoelectronic components, and modelling of the optical field emission from such components are presented. Through the development and characterisation of indium phosphide (InP) NW device pairs, optical communication across separations of up to 3 µm in air is experimentally demonstrated, which is the first step towards larger broadcasting networks. We estimate that significantly larger communication distances are possible through component performance optimisation, and by embedded waveguide materials. With yields up to 80%, the presented fabrication pipeline allows scalable assembly of heterogeneous NWs, precisely positioned in designed assemblies of tens to hundreds. We also explore the integration of photochromic dye as an all-optical localised memory medium in between the optoelectronic III-V NWs. The optically responsive behaviour of the prototype devices suggests their potential as synaptic memory elements in nanowire-based neurons. Simulated work complements these developments by exploring how the NW optoelectronic components can form the basis of various broadcasting networks. In randomly oriented assemblies placed on a hexagonal grid, simulated InP emitter-receiver nodes were used a trainable echo-state network (ESNs), capable of mimicking a chaotic time series after minimal training. Both temporal and amplitude components of the time-series were preserved in larger networks, with smaller networks mostly replicating the frequency. The further use of directional Yagi-Uda metal nanoantenna, with added asymmetric director components, enables the directing and splitting of light from NW emitters, allowing for tuneable weights between them. This can be used to create compact layers of neural nodes with complex patterns of inhibiting and exciting weights between the nodes. Together, these results demonstrate the feasibility of integrating nanophotonic components into either geometrically structured or trainable neural networks, building towards circuits that can for example mimic important navigation functions of the insect brain.

Key words
III-V, Nanowire, Optoelectronics, Nanofabrication

Classification system and/or index terms (if any)

Supplementary bibliographical information

Language
English

ISSN and key title

ISBN
978-91-8104-555-0 (print)
978-91-8104-556-7 (pdf)

Recipient's notes

Number of pages
260

Price

Security classification

Development of Optically Communicating Nanowire-based III-V Devices

Optical broadcasting for artificial neural networks.

by Atli Vidar Már Flodgren

LUND
UNIVERSITY

Cover illustration front: A blender cycles conceptual render illustrating an on-chip emitter-receiver nanowire device pair mid-communication. Modelling, texturing, compositing and editing by Atli Vidar Már Flodgren.

Cover illustration back: Write-field image from a dense collection of nanowire device pairs on a chip of original design. SEM image was imported into blender, elevated using the luminosity as a height map, which also acted as the basis for the false colour. Modelling, texturing, compositing and editing by Atli Vidar Már Flodgren.

Funding information: A majority of the work presented in this thesis was financially supported by the European Innovation Council through the InsectNeuroNano Project.

Faculty of Science, Department of Physics

ISBN: 978-91-8104-555-0 (print)
ISBN: 978-91-8104-556-7 (pdf)

Printed in Sweden by Media-Tryck, Lund University, Lund 2025

Media-Tryck is a Nordic Swan Ecolabel certified provider of printed material. Read more about our environmental work at www.mediatryck.lu.se

MADE IN SWEDEN

Dedicated to my parents, my siblings, my friends and my partner.
To give thanks once is not nearly enough!

Contents

List of Papers

Publications Included in this Thesis

This thesis is based on the following publications, referred to by their Roman numerals:

I **Direct on-Chip Optical Communication between Nano Optoelectronic Devices**
V. Flodgren, A. Das, J. E. Sestoft, D. Alcer, T. K. Jensen, H. Jeddi, H. Pettersson, J. Nygård, M. T. Borgström, H. Linke, and A. Mikkelsen
ACS Photonics 2025, 12, 655–665
I performed a significant share of the end-stage fabrication and device characterisation measurements. Device characterisation was done according to an extensive python-based data extraction and analysis tool that I developed. I performed all FDTD simulations supporting the device characterisation data from which I calculated the EQE. I was the main responsible for writing the paper.

II **Flexible fabrication of aligned multi-nanowire circuits for on-chip prototyping**
V. Flodgren, A. Das, J. E. Sestoft, N. Löfström, D. Alcer H. Jeddi, M. Borgström, H. Pettersson, J. Nygård, and A. Mikkelsen
Manuscript Submitted
I performed the initial testing, including nanowire placement methods, evaporation, etching tests, patterned design and fabrication, device characterisation in several setups. I held a significant responsibility for the continued development of new device generations. I wrote the python GUI for the automatic extraction and categorisation of data, and the tools for characterisation of device ideality. I performed all relevant FDTD simulations that guided the work. I was the main responsible for writing the paper.

III **Controlling the Optical Coupling Strength in Optoelectronic Neu-ral Networks with Modified Yagi-Uda Nanoplasmonic Antennas**
V. Flodgren, A. Mikkelsen
Manucript in Writing
I performed all FDTD simulations, wrote all the scripting tools, analysed all the data, and was the main responsible for writing the paper.

IV **Integrating Molecular Photoswitch Memory with Nanoscale Optoelectronics for Neuromorphic Computing**
David Alcer*, N. Zaiats*, T. K. Jensen*, A. M. Philip, E. Gkanias, N. Ceberg, A. Das, **V. Flodgren**, S. Heinze, M. T. Borgström , B. Webb, B. W. Laursen, and A. Mikkelsen
Commun Mater 6, 11 (2025)
I was responsible for providing pre-characterised single nanowire devices for the DASA dye testing and discussions on single device measurements. I took part in the continuous discussions surrounding the experiments and project.

V **Neural network connectivity by optical broadcasting between III-V nanowires**
K. Draguns,**V. Flodgren**, D. Winge, A. Serafini, A. Atvars, J. Alnis, and Anders Mikkelsen
Manuscript Submitted
I provided feedback and discussed the FDTD simulations. I was responsible for evaluating the performance of nanowire network configuration by training the defined echo state network. I performed all numerical analysis from the training output, producing the figures for, and writing the related parts of the paper.

Publications not included in this thesis:
I contributed to the following publications during my PhD, but they are outside the scope of this thesis.

VI **Few-cycle lightwave-driven currents in a semiconductor at high repetition rate**
F. Langer, Y. Liu, Z. Ren, **V. Flodgren**, C. Guo, J. Vogelsang, S. Mikaelsson, I. Sytcevich, J. Ahrens, A. L'Huillier, C. L. Arnold, and A. Mikkelsen
Optica 7, 276-279 (2020)
I fabricated all devices used for all measurements, took a major part in designing and implementing the electrical measurement setup, and I participated in discussions and contributed with feedback on the manuscript. I wrote my Master's Thesis on the work predating this publication.

VII **Atomic Hydrogen Annealing of Graphene on InAs Surfaces and Nanowires: Interface and Morphology Control for Optoelectronics and Quantum Technologies**
S. F. Mousavi, Y. Liu, G. D'Acunto, A. Troian, J. M. Caridad, Y. Niu, L. Zhu, A. Jash, **V. Flodgren**, S. Lehmann, K. A. Dick, A. Zakharov, R. Timm, and A. Mikkelsen
ACS Applied Nano Materials (2022) 5 (12), 17919-17927
I purpose-designed and fabricated a sample template pattern that was necessary for locating target samples in the beamline. I contributed minor feedback to the manuscript.

VIII **Switching Dynamics and Interface Chemistry of Ferroelectric Hafnia Devices**
A. Irish, A. E. O. Persson, **V. Flodgren**, R. Athle, L.E. Wernersson, and R. Timm
Manuscript Submitted
I attended two beamtimes relating to this work. At each occasion, I was responsible for device handling after fabrication, including wire-bonding and assistance with electrical characterisation. For the second beamtime, I advised on device architecture redesign to improve measurement yield in the operando setup. I contributed minor feedback to the manuscript.

IX **Self-selective bismuth growth on GaAs zincblende/wurtzite heterostructure nanowires**
R. Yadav, S. Lehmann, S. Benter, **V. Flodgren**, E. Golias, A. Zakharov, K. D. Thelander, A. Mikkelsen, and R. Timm
Manuscript In Writing
I purpose-designed and fabricated a sample template pattern that was necessary for locating target samples in the beamline. I will contribute associated materials detailing this aspect in the manuscript.

Acknowledgements

The last few years of my PhD have been a real roller coaster. My own projects found a solid foundation to stand on, accelerating with exciting opportunities just beyond the horizon. I've had the chance to work with so many incredibly talented people from all across the world, encountering new and fascinating research at every turn. It was only when I had to sit down and actually write that I realised how difficult it was going to be to do justice to the people I've met along the way.

First of all, I want to thank my main supervisor, Anders Mikkelsen, for all the guidance throughout my time as a PhD student. You consistently gave me the freedom to focus on the aspects of each project that I found most meaningful and to explore other topics that piqued my interest. But when necessary, you always had the foresight to let me know when a project needed to be wrapped up. Your door was always open for questions, and I can't count the number of times meetings went on a bit too long because we found something more interesting to discuss. I don't think I could have asked for a better supervisor. I also thank my co-supervisor, Heiner Linke, for your invaluable insights during the photodetector meetings and discussions on the ongoing molecular detection scheme project. I'm looking forward to seeing it progress. To my co-supervisor, Cord Arnold. With the regrettable halt to project work incurred by COVID, I wish there was more time to explore the potential avenues for a revised project, like what we discussed at CLEO. Thanks to my co-supervisor, Edvin Lundgren, for the insightful discussions we had at the division, even though we didn't work directly on the same project. Finally, I would like to thank Dan Hessman for his thorough feedback during the internal review of my thesis.

Now comes the most difficult part, because I have far too many people I want to thank. The past few years have been absolutely phenomenal, and they would not have been the same without everyone at the division, through fika, kickoffs, after-work gatherings, barbecues, and everything in between. First of all, I'd like to thank Yen-Po, whose absence has been felt for far too long by more than just me. I don't think I've ever met a kinder, more helpful or enthusiastic person. The beginning of my PhD would not have been nearly as enjoyable without you. Next, to the one with whom I shared my cleanroom woes, Nils. Whether it was grabbing a quick coffee, discussing current events, complaining about tool downtimes, or hitting the gym. You haven't even been gone that long before my defence, and the division already feels different without you. To Abhijit, it's been a real pleasure working with you on these projects towards the end. I couldn't have managed much of it without your support. To Rohit, for all the fun times at the pub and solid workouts at the gym. Stay strong, man. To Ahmed, our resident strongman, for your wise words and encouragement. To Nelia, and special thanks to your office couch, for all the great gossip, beers, and wonderful INN travels. Next, I want to thank my local bouldering crowd: Alfred, Dima, and Andrea. Always excellent company at the wall, and naturally at the pub too. To Nishant, our first beamtime together may not have been great for research, but at least Paris was lovely. I hear we have unfinished business there still? And to Hari, for the good chats and banter, especially about Nils. To Oskar, smoker of meats, drinker of beer,

master of the barbecue. Always a good time, man. And thanks to everyone else who makes our division the best it can be. Thank you, Auden, Ulrike, Mehran, Zisheng, Huaiyu, Ziyun, Zephyr, Fatemesh, Ajsa, Runqing, Yuhe, Yi Liu, Hanna, Ekaterina, Megan, Mahesh, Jesper, Rainer, Elizabeth, Pablo, Matias, and Mathieu. With special thanks to Patrik, funny and helpful, with office hours sponsored by the sound of Sabaton.

I'd also like to thank those involved in the InsectNeuroNano project. To Joachim, maker of extremely good coffee, and whose favourite method is always the one that works. To Nathaniel, who endured measurements of our devices over the summer for the greater good. To David, who convinced us all to take the extremely memorable journey to Portugal by train together, I won't forget it. To Thomas, for all the good times in the lab, where sometimes the solution might just be shorting the ends of a high voltage cable with solder wire. And to Magnus, who was often one step ahead of the rest of us when solving fabrication issues, allowing us to take many shortcuts as a result.

I also want to give extra thanks to the NanoLund staff: Alexander, Anders, Natalia, Peter, and Sarah, for doing the hard work necessary to keep the cleanroom running. These projects would not have made nearly as much progress without your outstanding efforts.

I want to extend special thanks to the friends I made during my bachelor's, who have stuck with me through thick and thin. It's hard to believe it's been almost eleven years since we first met. I want to thank Tim, for helping me get started with the gym during COVID, for the climbing sessions, and for the movie nights. Thanks to Daniel, who should know that leaving the lab late to hang out with you after work was probably the best way to end a day. Be like Daniel. Be cool. To Yoana, for never letting a party go by without your baked goods. I'm deeply thankful for the unwavering support of Meng, always ready to lend a hand, even while preparing for your own defence. You were always a voice of reason. I want to thank Karl, for all the magic and late board game nights, always running late because we just had to play one. more. game. And I also want to thank you again for helping us move out when our downstairs neighbour was going off the rails. Had we stayed any longer, I think it really would have impacted my thesis. To the two of you, I say: for the Emperor! And I also want to thank Ace, for being such a good dog when we looked after him.

Some friends may be nearby, but distance is no stranger to lasting friendship. I want to thank my friends from the UK: Alex, Michael, and Harry, for being my long-standing bruvs for over fifteen years. Time flies, doesn't it?

Finally, I want to thank my parents and my siblings, for always supporting me. You already know how much I appreciate you, and if I wrote it all here it'd never end. I also want to thank Vivi, for helping proofread my thesis. And last but by no means least, my partner Martin, who I thank dearly for being there for me every day, and for enduring through these final months of my thesis writing of loud mechanical keyboard clacking, especially through all those long late nights.

Thank you all! And you especially, dear reader, for making it this far! There's only 100 pages more to go, over 250 if you got a paper copy!

Popular summary in English

Recent developments in artificial intelligence, colloquially known just as AI, are beginning to push against the limits of what our energy systems can reasonably support. Consider that generative AI will use about 0.25 kWh to create a summary of this 100 page thesis, which is like fully charging your phone 20 times over. As such, there is a need to investigate into alternative device architectures that can perform the tasks of a neural network more efficiently. This thesis focuses primarily on the study and development of the optoelectronic components necessary to realise one such system.

Much of the work in this thesis is inspired on a recently developed model, that we will call the Stone model, emulating the navigational function of bees. When they fly out from the nest, get lost in the wind, run into new obstacles, they still somehow always find their way back home. In a single day, their brains can perform these calculations all while using less than 1/200th of energy in a single grain of sugar. In the creation of this model, they found that bees have a compass like arrangement of neurons connected to their senses, that can see and remember the polarisation of sky light, informing them of their cardinal orientation during flight. Combine this with the ability to measure distance, and this allows them to perform something known as path tracing, which is where all legs of its journey are summed up to calculate a single line, drawn from its current location to home. This ability is innate, and hard-wired into their brains. What's more exciting still, is that the way these neurons are laid out, and how strongly they communicate with one another, can be mirrored using the emission pattern from similarly positioned light emitting nanowires. This resemblance opens the door to replicating the same principles using entirely artificial components. By replacing neurons with a collection of light-emitting and absorbing nanowires, and introducing a responsive material that stores signal history, we can begin to emulate the same kind of memory-based navigation system.

A nanowire, as the name suggests, is an extremely small wire whose diameter is on the order of 10–100 nanometres, over a thousand times thinner than a strand of human hair, with a length typically 10–100 times greater than its diameter. Unlike traditional silicon, which is inefficient at emitting or detecting light, III-V materials like indium phosphide (InP) and indium gallium nitride (InGaN) perform much better. While these materials are typically too expensive for large-scale electronics, nanowires can be grown layer by layer, using just small amounts of these high-performance materials, making them more accessible for practical use. This method also means grown wires can be engineered to all be standalone transistors, solar cells, or light emitting diodes (LEDs). What's more, because their diameter is on the same scale as visible light, their interactions with light are particularly strong. For example, they can act like light-guiding optical fibres along their length, making them efficient directional emitters and absorbers. This unique combination of properties would allow us to create a light-based communication network, similar to the signalling systems found in bees' neural networks, using nanowires to transmit and receive optical signals. The question then is, how does one place wires thousands of times smaller than a human hair from different grown arrays of nanowires onto a chip in a specific design, while also ensuring all components work as intended? Turns out, the difficulty of answering this

question is why even the simplest device design composed of an emitter-receiver pair, had not yet been made prior to this work.

This thesis presents one of the first experimental demonstrations of light-based signalling between individual III-V nanowires, forming the basic building blocks of a photonic neural network. We demonstrate a flexible high-yield fabrication process that can produce complex assemblies of any number of different nanowires. This is achieved combining trenches, just wider than a nanowire, etched directly into our silicon chip, with an extremely precise robot assisted probe capable of picking up and placing individual nanowires anywhere on the chip. Trench design guides the placement from the probe, with nanowires attracted to the inside of the trench like static, allowing us to control placement and separation for up to hundreds of nanowires. When electrically connected, we can send a current through one to induce light emission, which can then be measured at another. In greater assemblies, these can replicate the signals sent between neurons in the insect brain.

However, like the bees, we cannot navigate home without a memory. For this, we evaluated the use of a photochromic dye, a substance that gradually becomes more transparent when exposed to high-intensity light. This transparency doesn't just change the look of the material, but it physically alters how much light can pass through it. When paired with polarisation-sensitive detectors, this dye could serve as a form of tuneable optical filter, adjusting how strongly different signals are received. Crucially, this change is retained for a long time, encoding the history of light exposure in a way that mimics how the real neurons reinforce or forget connections.

Building on this emitter–receiver platform, the second part of this thesis explores how networks of nanowires might do even more. We simulate a kind of artificial brain known as an echo state network. Imagine tossing a pebble into a pond, ripples form, bounce off obstacles, overlap, and slowly fade. In much the same way, light pulses travel through a jumble of loosely connected nanowires, with each one echoing the signal it just received. The result is a constantly shifting pattern that holds a short memory of what just happened. We demonstrate that the resulting memory space, called the reservoir, is rich enough that even a simple output layer can be trained to predict future values of a chaotic time series.

Finally, we simulate a more structured nanowire layout, resembling the architecture of a convolutional neural network. In this case, nanowire emitter nodes are each paired with a nanoscale Yagi-Uda antenna, a scaled-down version of the standard rooftop TV antennas. These antennas use reflectors and directors to shape and steer light in a specific direction. By tweaking the final directors, such as adding angled wings to make a V-antenna, we can control the direction and strength of light each nanowire sends forward. This tuneability shows how more complex broadcasting behaviour can be engineered into future nanowire-based networks.

Together, these advancements bring us closer to experimentally realising a new type of artificial neural network, one that might eventually emulate the Stone model's biologically inspired navigation system using optoelectronic nanowire devices in a broadcasting scheme.

Vísindaleg samantekt fyrir almenning

Nýlegar framfarir í gervigreind, daglega þekkt sem AI, eru farnar að reyna á mörk þess sem orkukerfi okkar þola. Íhugaðu að AI myndi þurfa um 0,25 kilówattstundir til að búa til samantekt af þessari doktorsritgerð, sem mótsvarar því að hlaða farsíma að fullu 20 sinnum. Þess vegna er brýn þörf á að rannsaka aðrar hannanir á þess konar tæknilegum tauganetum sem gætu framkvæmt tölvunarverkefni á skilvirkari hátt. Þessi ritgerð beinist fyrst og fremst að rannsóknum og þróun ljósfræðilegra eininga sem nauðsynlegar eru til að raungera slík kerfi.

Mikið af verkinu í þessari ritgerð er innblásið af nýþróuðu líkani, sem við köllum „the Stone model“. Líkanið hermir eftir leiðsögukerfi býflugna. Þegar þær fljúga úr hreiðrinu, týnast í vindinum, rekast á hindranir, þá finna þær samt einhvern veginn alltaf leiðina heim. Á einum degi getur þetta kerfi framkvæmt þessa útreikninga og notað minna en 1/200 af orkunni í einu sykurkorni. Líkanið byggir á þeirri uppgötvun að býflugur hafa áttavitalíka uppröðun taugafruma sem tengjast skynfærum þeirra, skynfæra sem geta séð og munað skautun himinljóssins og upplýst þær um stefnu þeirra á meðan þær fljúga. Með því að sameina þetta við hæfileikann til að mæla fjarlægð, þá geta þær framkvæmt eitthvað sem kallast leiðarmæling („path tracing”), þar sem allir áfangar ferðalagsins eru teknir saman til að reikna út eina línu frá núverandi staðsetningu til heimahaga. Þessi hæfileiki er meðfæddur og innbyggður í heila þeirra.

Það sem er ennþá meira spennandi er að hægt er að herma eftir hvernig þessar taugafrumur eru staðsettar og hversu sterk samskipti þær eiga við hver aðra með því að nota útgeislunarmynstur frá svipað staðsettum ljósgeislandi nanóþráðum. Þessi líkindi opna dyrnar fyrir því að herma sömu meginreglur með tæknilegum hætti. Með því að skipta út taugafrumum fyrir safn af ljósgeislandi og ljósgleypandi nanóþráðum og kynna til leiks viðbragðshæft efni sem geymir merkjasögu, getum við byrjað að herma eftir sams konar minnisbundnu leiðsögukerfi.

Nanóþráður, eins og nafnið gefur til kynna, er agnarlítill vír sem er á bilinu 10–100 nanómetrar í þvermál, meira en þúsund sinnum þynnri en hár úr mannshári, og er yfirleitt 10–100 sinnum lengri en þvermál hans. Ólíkt hefðbundnu sílikoni, sem er ekki sérstaklega skilvirkt hvað varðar að gefa frá sér eða greina ljós, þá virka III-V efni eins og indíumfosfíð (InP) og indíumgallíumnítríð (InGaN) mun betur. Þó að þessi efni séu yfirleitt of dýr fyrir stórfellda rafeindatækniframleiðslu, er hægt að rækta nanóþræði lag fyrir lag með örlitlu magni af þessum afkastamiklu efnum, sem gerir hagnýta notkun mögulega. Þessi aðferð gerið það mögulegt að rækta þræði sem virka eins og sjálfstæðir smárar, sólarsellur eða ljósdíóður (LED). Þar að auki, vegna þess að þvermál þeirra er á sama skala og sýnilegt ljós, er vixlverkun þeirra við ljós sérstaklega sterk. Til dæmis geta þeir virkað eins og ljósleiðarar sem gerir þá að skilvirkum stefnugeislandi og ljósgleypandi efnum. Þessi einstaka samsetning eiginleika myndi gera okkur kleift að búa til ljósbundið samskiptanet, svipað og merkjakerfin sem finnast í tauganetum býflugna, með því að nota nanóþræði til að senda og taka á móti sjónmerkjum. Spurningin er, hvernig er hægt að setja þræði þúsund sinnum minni en mannshár úr mismunandi ræktuðum vigrum af nanóþráðum á örgjörva í tiltekinni hönnun, en jafnframt tryggja að allir hlutar virki eins og til er ætlast? Svo vítt sem við

vitum þá er þetta verkefni það fyrsta nokkru sinni til að að framleiða tæki af þessari tegund, þ.e.a.s. pörum af sendanda og móttakara.

Þessi ritgerð kynnir eina af fyrstu tilraununum sem sýnt hefur fram á möguleikann á ljósbundnum merkjasendingum milli einstakra III-V nanóþráða, og þar með sannreyna eina tegund grunnbyggingareiningar i ljósfræðilegu tauganeti. Við sýnum fram á sveigjanlegt og afkastamikið framleiðsluferli sem getur framleitt flóknar samsetningar af hvaða fjölda mismunandi nanóþráða sem er. Þetta er gert með því að sameina skurði, örlítið breiðari en nanóþráður, sem eru skornir í kísilörgjörva, og með aðstoð vélmennis koma fyrir einstökum nanóþráðum hvar sem er á örgjörvanum. Hönnun skurðarins stýrir staðsetningu þráðanna, þar sem nanóþráðar laðast að innanverðum skurðinum vegna stöðurafmagns. Það gerir okkur kleift að stjórna staðsetningu og aðskilnaði allt að hundruða nanóþráða. Þegar þeir eru tengdir rafmagni getum við sent straum í gegnum einn til að örva ljósgeislun, sem síðan er hægt að mæla í öðrum. Í stærri samsetningum geta þessir þræðir endurtekið merki eins og þau sem eru send milli taugafrumna í heila skordýra.

En alveg eins og býflugur, getum við ekki ratað heim án minnis. Í þeim tilgangi rannsökuðum við notkun ljóslitarefnis sem verður smám saman gegnsærra þegar það verður fyrir miklu ljósi. Þetta gegnsæi breytir ekki aðeins útliti efnisins, heldur líka hversu mikið ljós getur farið í gegnum það. Þegar þetta litarefni er parað við skautunarnæma skynjara gæti það þjónað sem eins konar stillanleg ljóssía, sem aðlagar hversu sterk mismunandi merki berast. Mikilvægast er að þessi breyting endist í langan tíma og kóðar sögu ljósáhrifa á þann hátt að það líkir eftir því hvernig raunverulegar taugafrumur styrkja eða gleyma tengingum.

Byggt á þessum sendanda-móttakara verkvangi, kannar annar hluti þessarar ritgerðar hvernig net nanóþráða gætu gert enn meira. Við hermum eftir eins konar gerviheila sem kallast bergmálsnet. Ímyndaðu þér að kasta steini í tjörn, öldur myndast, endurkastast af hindrunum, skarast og hverfa hægt. Á svipaðan hátt ferðast ljóspúlsar í gegnum hrúgu af lauslega tengdum nanóþráðum, þar sem hver og einn endurómar merkið sem hann var að taka við. Niðurstaðan er stöðugt breytilegt mynstur sem geymir stutt minni um það sem gerðist. Við sýnum fram á að minnisrýmið sem myndast, kallað geymirinn („the reservoir“), er nógu ríkt til að jafnvel einfalt umkóðunarnet geti verið þjálfað til að spá fyrir um framtíðargildi óreiðukenndrar tímaraðar.

Að lokum hermum við eftir skipulögðu nanóþráðasniði sem líkist arkitektúr vafins tauganets. Í þessu tilfelli eru nanóþráðahnútar („nanowire emitter nodes“) paraðir við Yagi-Uda loftnet á nanóskala, sem er örsmá útgáfa af venjulegum þaksjónvarpsloftnetum. Þessi loftnet nota endurskinsmerki og ljósleiðara til að móta og stýra ljósi í ákveðna átt. Með því að fínstilla lokaljósleiðarana, svo sem að bæta við skásettum vængjum til að búa til V-loftnet, getum við stjórnað stefnu og styrk ljóssins sem hver nanóþráður sendir áfram. Þessi stillingarhæfni sýnir hvernig hægt er að hanna flóknari útsendingarhegðun í framtíðar nanóþáðanetum.

Samantekið færa þessar framfarir okkur nær því að þróa nýja tegund af gervitauganeti, sem gæti að lokum hermt eftir því líffræðilega leiðsögukerfi sem gaf innblásturinn að Stone líkaninu. Neti sem byggir á ljósleiðandi nanóþráðatækni.

Populärvetenskaplig Sammanfattning på Svenska

Senaste utvecklingarna inom artificiell intelligens, mer känt som AI, har börjat tänja på gränserna för vad vår elproduktion klarar av. Att be en generativ AI sammanfatta den här avhandlingen på 100 sidor använder cirka 0.25 kWh, vilket är lika mycket energi som behövs för att ladda din mobil till fullt 20 gånger. Därför finns det ett behov att utforska alternativa kretsarkitekturer som utför samma uppgifter som ett neuralt nätverk, fast mer energieffektivt. Den här avhandlingen fokuserar på utvecklingen av de optoelektroniska komponenter som krävs för ett sådant system.

En stor del av arbetet i den här avhandlingen inspireras av en ny modell som vi här kallar Stone-modellen, som försöker efterlikna binas navigationsförmåga. Bin kan orientera sig tillbaka hem till sina bon även fast de stöter på starka vindar, hinder och långa flygturer. Vid skapandet av den här modellen upptäckte de att bin har en kompassliknande struktur av neuroner kopplade till deras sinnen, som kan se och minnas polarisationen av ljuset från himlen, vilket informerar dem om deras väderstreck under flygning. Tillsammans med deras förmåga att mäta avstånd kan de räkna ut den exakta vägen hem. Detta kallas för path tracing som är medfött och hårdkodat i deras hjärnor. Denna process förbrukar mindre än 1/200 av energin i ett enda sockerkorn per dag. Det mest spännande är att denna neurala struktur påminner starkt om hur ljus kan styras och sändas via nanotrådar. Vilket är extremt tunna trådar av ljusavgivande material. Genom att ersätta nervceller med ljusemitterande och absorberande nanotrådar, tillsammans med ett material som minns tidigare signaler, kan vi börja efterlikna samma typ av navigationssystem men med helt konstgjorda komponenter.

Nanotrådar har en diameter på bara 10–100 nanometer vilket är över tusen gånger tunnare än ett hårstrå men med en längd 10-100 gånger större än dess egna bredd. Till skillnad från vanlig kisel, som är dålig på att interagera med ljus, fungerar III-V-material som indium phosphide (InP) och indium gallium nitride (InGaN) mycket bättre. Dock är dessa material ofta för dyra för att rättfärdiga deras användning inom storskalig elektronik. Det är där nanotrådar kommer in i bilden. Eftersom nanotrådar kan byggas upp lager för lager krävs bara små mängder av dessa material, vilket gör dem mer praktiskt användbara. Dessutom kan enskilda nanotrådar konstrueras så att de fungerar som transistorer, solceller eller lysdioder (LED). De fungerar både som sändare och mottagare av ljus, nästan som fiberoptik och kan därmed användas som ett ljusbaserat kommunikationsnät, ungefär som i binas hjärnor. Men hur placerar man trådar som är tusentals gånger tunnare än ett hårstrå på rätt plats på ett chip och samtidigt säkerställer att varje komponent fungerar som den ska? Det är just den här utmaningen som gjort att ingen lyckats bygga den enklaste komponent av den här typen innan det här arbetet.

I den här avhandlingen visas ett av de första experimenten där ljussignaler skickas mellan individuella nanotrådar. Med en kombination av etsade spår direkt i kisel-chipet ungefär lika breda som nanotrådarna tillsammans med en robotassisterad prob kan trådarna placeras med hög precision. Nanotrådar faller ner i spåren som om de drogs dit av statisk elektricitet, vilket möjliggör kontrollerad placering av hundratals trådar. Genom att skicka ström genom en av trådarna ger den av ljus, som kan sen mätas i en annan tråd. I större

system kan dessa egenskaper användas för att efterlikna de signaler som skickas i en insektshjärna.

Men precis som bina behöver även våra artificiella system minne för att navigera. Därför testades en fotokromatisk färg vilket är ett material som blir mer genomskinligt vid starkt ljus. Denna förändring påverkar hur mycket ljus som släpps igenom och fungerar som ett justerbart filter. Eftersom förändringen består över tid, kan materialet lagra information om tidigare ljusnivåer på ett sätt som liknar hur biologiska neuroner förstärker eller glömmer kopplingar.

I den andra delen av avhandlingen byggs dessa grundläggande koncept vidare på för att undersöka hur ett större nätverk av nanotrådar kan utföra mer komplexa funktioner. Vi simulerar ett så kallat "echo state network", där varje ljuspuls som skickas genom nätverket skapar en form av eko. Tänk dig att du kastar en sten i en damm, små vågor sprider sig, reflekteras mot hinder, överlappar varandra och försvinner långsamt. Detta ger systemet ett korttidsminne som kan användas för att förutse kaotiska tidsserier.

Slutligen undersöks ett mer organiserat nanotråds-nätverk som liknar arkitekturen i ett konventionellt neuralt nätverk. Här paras varje ljuskälla med en liten Yagi-Uda-antenn som är en slags riktantenn inspirerad av TV-antenner. Genom att justera de sista delarna av antennen, till exempel genom att lägga till vinklade "vingarför att skapa en V-formad antenn, kan vi kontrollera både riktning och styrkan på ljuset varje nanotråd skickar vidare. Denna anpassningsbarhet visar hur mer avancerade sändningsbeteenden kan byggas in i framtida nätverk baserade på nanotrådar.

Sammanfattningsvis för denna avhandling oss ett steg närmare att skapa ett nytt slags artificiellt neuralt nätverk inspirerat av biologiska system med hjälp av optoelektroniska komponenter byggda av nanotrådar.

Abbreviations

Al_2O_3	Aluminium Oxide
HfO_2	Hafnium Oxide
SiO_2	Silicon Oxide
AI	Artificial intelligence
ALD	Atomic layer deposition
ANN	Artificial neural network
BCB	Benzo cyclobutane
CAD	Computer-assisted design
CMOS	Complementary metal-oxide-semiconductor
CMP	Chemical mechanical polishing
CNN	Convolutional neural network
CPU	Central processing unit
DASA	Donor–acceptor Stenhouse adduct
DC	Direct current
DFR	Device Frankenstein
DI	Deionised water
E-beam	Electron beam
EBL	Electron beam lithography
EQE	External quantum efficiency
ESN	Echo state network
EUV	Extreme ultraviolet
FDTD	Finite-Difference Time-Domain
FET	Field effect transistor
GAA	Gate-all-around
GDS	Graphic Design System
GPU	Graphics processing unit
InAs	Indium arsenide
InGaP	Indium gallium phosphide
InP	Indium gallium arsenide
InP	Indium phosphide
IPA	Isopropyl alcohol
ITO	Indium tin oxide
IV	Current-Voltage
LED	Light emitting diode
Lor	Lift-off resist
MIBK	Methyl isobutyl ketone
MLA	Maskless aligner
MOS	Metal-oxide-semiconductor
MOSFET	Metal-oxide-semiconductor field effect transistor
MOVPE	Metalorganic vapour-phase epitaxy
NW	Nanowire
Pabs	Power absorption

PEC	Perfect electric conductor
PMC	Perfect magnetic conductor
PML	Perfectly matched layer
PMMA	Poly(methyl methacrylate)
RAM	Random-access memory
RF	Radio frequency
RIE	Reactive ion etching
RNN	Recurrent neural network
rpm	Revolutions per minute
SAG	Selective area growth
SEM	Scanning electron microscope
SMU	Source measure unit
STM	Scanning tunelling microscope
TE	Transverse electric
TM	Transverse magnetic
TMA	Tetrakisdimethylamidohafnium
TMA	Trimethylaluminum
TSFS	Total-Field Scattered-Field
UV	Ultraviolet
VLS	Vapour-liquid-solid

CHAPTER 1

Introduction

'Pleasure to me is wonder—the unexplored, the unexpected, the thing that is hidden and the changeless thing that lurks behind superficial mutability.'
—H. P. Lovecraft, The Call of Cthulhu

Moore's law, the prediction that transistor counts on integrated circuits will double every two years[1], has held its ground for several decades. Scaling down transistor size, beyond just reducing the material cost from an increased integrated circuit density, comes with several other benefits. One of the important ones, but perhaps less well known in the public eye, is Dennard scaling, stating that the power density remains proportional to the area occupied by the transistor devices on the integrated circuit[2, 3]. With that in mind, ever since its inception in the early 1960s, we have continuously seen scaling improvements to the silicon-based metal-oxide-semiconductor (MOS) field-effect transistor (FET, or together as MOSFET) through the use of the device architecture known as the complementary metal-oxide-semiconductor (CMOS) platform with no end in sight, until recently. Today, chipmakers Samsung and TSMC both have a 3 nm transistor process that is in early stages of mass production. To keep scaling according to Moore's law, more complex architectures have been introduced, such as FinFET[4] and, more recently, gate-all-around (GAA) [5], both of which can be seen in Figure 1.1. The only way to target

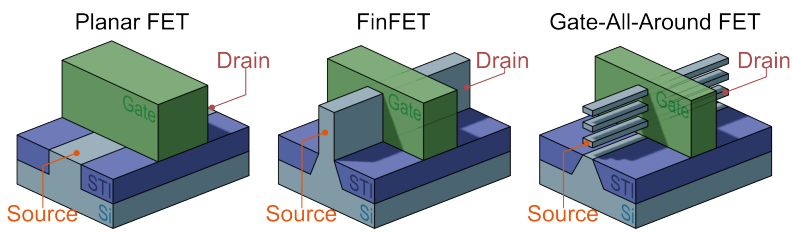

Figure 1.1: Series of diagrams illustrating planar, Fin, and GAA FET architectures, listed in order of increasing performance. Note that the GAA architecture uses nanowire channels.

this 3-5 nm range of transistor gate width, is with highly advanced immersion lithography equipment, like the extreme ultra violet (EUV) systems developed only by ASML[6]. As a consequence, improving the power performance of traditional chip technology is getting

much more complicated and expensive, both in terms of chip design and manufacturing. As a result, fundamentally different architectures and new semiconductors beyond silicon (Si) are being considered for more and more applications.

Interest in reducing energy consumption in computing is now also driven by recent developments of artificial neural networks (ANN) for machine learning, more colloquially also called artificial intelligence (AI), that has taken the world by storm. For some, these large language models offer assistance, possible short-cuts, and sometimes complete replacements for their work. They serve as source of entertainment through image, sound and audio generation, to which the ethical questions are raised over how the training data is obtained. At a surface level, this technology has limitless potential applications, but it comes at a shockingly high energy cost, with global estimates suggesting that 4.5% of energy resources will be wholly allocated to its use by 2028[7]. This, as a whole, has brought the energy efficiency for use in AI applications of modern CMOS technology into question. To reduce this energy footprint, NVIDIA, for instance, is already developing new types of CMOS graphics processing unit (GPU) components called tensor cores, whose purpose is to solve 4x4 matrix multiplication with mixed accuracy, resulting in a higher throughput[8]. In spite of this, it is still a brute-force approach to deep learning, the efficiency of which could be greatly bolstered by seeking alternatives to the architecture behind its computation. In particular the idea to design hardware specifically mimicking traits of biological neural structures has gained traction in the form of neuromorphic computing. A wide variety of alternative physical mechanisms for this type of computation are being considered[9], one of them being the use of nanophotonic circuits. Photonics has a variety of potential advantages in both high speed, low energy consumption and signal multiplexing[10–14]. Significant recent progress has been realized, although it is still very much in an exploratory stage.

Si being the dominant player in the semiconductor industry is no surprise in some sense, seeing as it the second most abundant element in the Earth's crust. While this makes it both cheap and easily obtainable, combine this with the added benefit of its broad range of good physical properties, and ability to form good defect free interfaces, and you have the reason why it has been the undisputed leader in standard electronic circuits for computation ever since the first transistor was made from it. Branching out from an extremely well established industry, with decades worth of developed high-yield nanofabrication processes, requires a use-case where Si is not enough. In particular, the part that Si will play in the future of active components converting between photon and electrons, namely optoelectronics, is more limited. The indirect nature of Si's 1.12 eV bandgap results in lowered efficiency of recombination and photon excitation[15]. Si's absorption efficiency under the solar spectrum[16, 17], is also quite low compared to the far more expensive group III and V semiconductor alloys. However, these materials still remain far more expensive, and therefore most commercial solar cells still use Si, where the ease of fabrication, and low production costs, make up for the lower efficiency. III-V based solar cells have exceeded efficiencies of their Si counterparts since the early 90s[18, 19], prompting ongoing efforts

to develop cost-effective strategies for incorporating these materials into next-generation photovoltaic architectures. Among the various approaches under investigation, the semiconductor nanowire (NW), a slender, cylindrical structure with diameters typically ranging from 10 to several hundred nanometers and a few micrometers in length, has emerged as a particularly promising form factor for both photovoltaic and LED applications. NW growth can be tailored to serve a wide range of applications, from tuning the absorption cross-sections for increased photocurrent generation in solar cells and photodetectors[20], to enabling controlled radial and lateral compositions for direct formation of doping profiles in transistors and p-n junctions[21–23], facilitating even the creation of complex heterostructure designs[24–28].

In large arrays, standing III-V NWs are the ideal candidate for achieving high solar cell and LED efficiency without the cost normally associated with the conventional top-down approach. On the other hand, building transistors or other analogue components of single/few nanowires have been suggested for both on chip optical communication[29], quantum technology[30–32], and neuromorphic computing[14, 33–36]. For the latter, the idea is to make use of their efficient light emission and absorption in a broadcasting scheme, not unlike how neurons in the brain send signals, which has not been done previously.

As such, we wish to specifically explore how the innate properties of NW-based III-V photovoltaic and LED devices can be used together, both in on-chip and externally coupled systems. In doing so, we are taking the first steps toward creating biologically inspired ANNs based on analogue weight instead of the schemes which are essentially based on efficient dependence on matrix multiplication. We mean to achieve this using light broadcasting from laterally assembled systems of NWs, emulating the low-energy cost of biological neuron activation mechanisms[9, 37, 38]. And by creating a CMOS compatible fabrication pipeline, we can avoid making a complete departure away from silicon wafers, and instead use the well established NW growth techniques for photovoltaic and LED application alike,to supplement established CMOS architecture.

1.1 Artificial Neural Networks Inspired by Nature

To aid our nanoscale hardware design, it is a good approach to identify specific neural networks from nature that can be described by a mathematical model. The network should be simple, allowing us to eventually create all necessary components to emulate a complete system, but advanced enough so it can carry out a relevant task. Here insects neurobiology is particularly interesting, since their simpler neural structure, when compared to mammals, are hierarchical in nature and contain hardwired subcircuits[39]. Due to the Rayleigh scattering of light through the Earth's atmosphere, skylight has a defined polarisation pattern that many insects rely on for navigation and orientation. Recently, a biologically constrained computational model, that we will call the Stone Model, was developed from measured neuron activity in a bee. The goal was to reproduce the navigational

memory and consequent path tracing they perform during the flight out from the nest, and for their navigation home[40]. It was found that these insects have a compass-like array of neurons, visualised in Figure 1.2 (a) as the green inner ring. Together, these neurons form a ring attractor, which is a type of recurrent neural network with, as the name suggests, a circular topology, with each node representing a discrete direction around the azimuth. These networks are commonly used to model directional or spatial encoding in biological systems, like the brains internal compass often known as the head-direction[41]. In this case, the ring attractor receives external input from polarisation sensitive heading neurons, whose magnitude input is modified by a speed neuron that measures optical flow. For the insect, during navigation, these neurons encode navigational information into memory as a cardinal amplitude, the sum of which when processed by the network can produce a directional home vector. For the flight back to its nest, the compass neurons remain active, continuously informing the insect where it needs to go in order to reach the location at which the resultant directional vector stored in its navigational compass is zero once more. This means that if it would meet with any obstacles or deviations, then these detours are encoded into memory, readjusting where the zero-vector point can be found.

Now, you might be wondering how all of this ties into III-V NW semiconductor

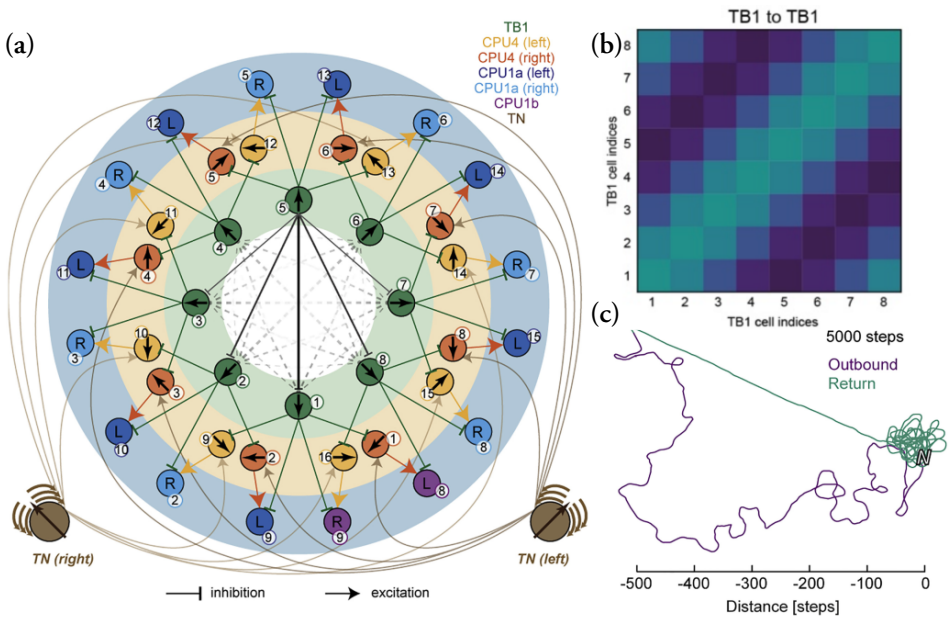

Figure 1.2: (a) Visualisation of the Stone model's ring-like topology for the proposed path integration circuit. The green TB1 ring represents the compass neurons that make up the ring attractor network, and are equivalent to the network also shown in Figure 1.3. (b) Attractor ring inhibitory node weights, with the x and y axes representing input and output of said cell index respectively. (c) An example of the python based Stone Model using the weights from (b) being set free after a random travel signal input was simulated, and fed to the node network, resulting in the successfully path-traced travel back to the home node labelled N. Figures reproduced from [40] with permission.

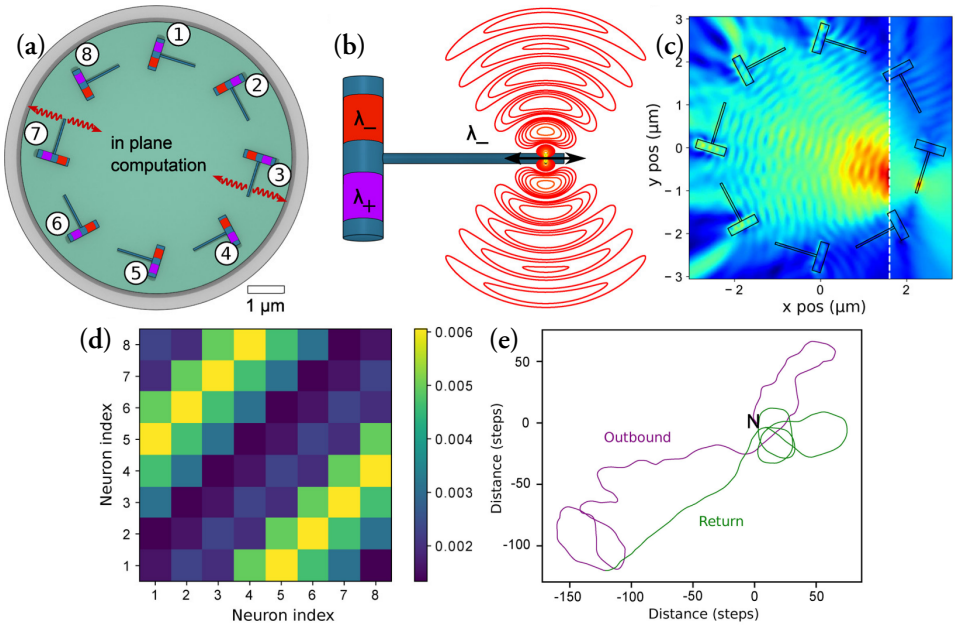

Figure 1.3: (a) Top down illustration of the conceptual ring NW network, where each neuron node is represented by a branched tandem NW, a close-up of which is shown in (b), whose ends act as inhibiting and activating segments. Panel (c) shows what the electric field intensity looks like within the waveguided system. (d) Shows the same type of inhibiting weight distribution as in Figure 1.2 (b), where the asymmetry around the diagonal is due to the asymmetric design of the NW neuron. (e) Shows the navigational performance these weights produce when used in the python-based implementation of the Stone model, as a comparison to Figure 1.2 (c). All figures were reproduced from [33]

devices. The key to the connection lies in the pilot study[33] on which many developments presented in this thesis build upon, which created a NW broadcasting network based on the ring attractor of the stone model. This network is visualised in Figure 1.3, where a branched NWs, whose theoretical heterojunction base is both polarisation sensitive[42] and has two segments designed to absorb two specific wavelengths of light. An externally coupled specifically polarised light source, representing the input from heading and speed neurons described earlier, act as the activating signal, whereas in-plane signals broadcast from the emitter segment act as the inhibiting signal, just like in the Stone model. The resultant inhibiting weights produced by the in-plane nodes of this network can be seen in Figure 1.2 (b), compared to the physically derived weights from the Stone model in (d). When these weights are used together with simulated input data, a python version of the model developed in [40] could be applied, resulting in near identical results, as compared in panels (c) and (e).

This pilot study is what led to the creation of the InsectNeuroNano[43] project, a large scale collaboration effort funded by the European Innovation Council as a bid to lead the physical development and eventual implementation of this technology. This thesis will focus mainly on my contributions to this project, including, but not limited to, the

development and characterisation of the core optically communicating NW components necessary to realise the network described in the pilot study, in addition to expanding on additional simulated broadcasting networks.

1.2 Thesis Outline

In this thesis, I will discuss the multi-faceted approach for the simulation, fabrication and characterisation of the components necessary to realise optical broadcasting schemes purposed for use in physically defined neural networks. Since the work is split between nanofabrication, electrical characterisation, and simulation, we have a substantial amount of theory to cover. To start off with, Chapter 2 will be a brief overview of semiconductor theory, with a focus on the III-V materials that have been used in our devices. Chapter 3 will go over nearly all nanofabrication techniques and tools used in the nanoscale processing performed for all devices discussed in the thesis. Following this, Chapter 4 marks the end of background theory, and will cover how finite-domain time-difference (FDTD) simulations can be used to produce accurate models of optical systems, allowing for the estimate of cross-sections, forward scattering, and total power absorption between components in emitter-receiver systems.

The second half of this thesis will cover the contents of Papers I-V, starting in Chapter 5 with the combined fabrication, and characterisation, of on-chip NW emitter-receiver optoelectronic systems, assembled from indium phosphide (InP) p-i-n junction NWs, capable of optical communication. These components act as a proof-of-concept step towards realising the more complex networks illustrated in Figure 1.3. This will cover Papers I and II. To highlight the significance of this work it is important to state that, to our knowledge, this type of on-chip optical communication has never before been physically demonstrated. We expand on the idea of optical communication by presenting the possible use of photochromic dyes, presented in paper IV, as a memory component. The progressive photobleaching of the dye demonstrates the ability to induce an altered photoresponse from an encapsulated single InP NW, showcasing how this could be used in on-chip applications, further building towards the components necessary to realise the biologically inspired neural network that InsectNeuroNano strives to achieve.

Following this, Chapter 6 will focus solely on FDTD simulated findings. From Paper III, we will discuss the implementation of nanoscaled Yagi-Uda antennas, whose function is not only to improve signal strength between nodes in a similar network as in Figure 1.3, but also to act as elements to split and redirect the emission pattern in order to produce tunable analogue weights. We also detail and demonstrate the function of an alternative device architecture reliant on the idea behind echo state networks. Here, simulations were done between paired NWs at varying relative orientations, the result from which can be randomly assigned in a huge random NW network. The weight matrix produced by this system was consequently used to successfully train a python based implementation of an echo state network to reproduce a chaotic time series.

CHAPTER 2

Semiconductors and III-V Materials

'To succeed, planning alone is insufficient. One must improvise as well.'
—Isaac Asimov, Foundation

As global energy consumption continues to rise, especially now with the widespread adoption of energy-inefficient large language model AI, the demand for more efficient nanoelectronics has become more critical than ever. This has fostered an increasingly growing interest in the development of semiconductor devices based on III-V materials, with with recent developments in photovoltaics, LEDs, high-frequency photodetectors, and low supply voltage transistors. This section will outline the essential theoretical background needed to understand how doped semiconductor devices operate, with an emphasis on p-n and p-i-n junction diodes, which make up the fundamental building blocks for the modern optoelectronics. I will introduce the primary III-V materials used in our multi-NW assemblies, detailing the intended role of each component.

2.1 Semiconductors

Semiconductors are a group of materials uniquely characterised by their conductive behaviour, falling somewhere between that of conductors and insulators. Semiconductor materials often refer to the individual elements, like Si or Germanium (Ge), or their alloys, which can be composed of two or more elements, like indium phosphide (InP) or indium gallium arsenide (InGaAs), called binary and ternary alloys respectively. A large number of atoms brought together in a lattice results in a distribution of states with energies E and crystal momentum k, called the band structure, which can be occupied by electrons[44]. Within this distribution, there also exist regions of forbidden states that cannot be occupied, known as bandgaps. These states are filled with electrons from lowest to highest energy, eventually reaching a point where the bands cannot be filled any more, following the Fermi-Dirac distribution function. Conventionally, at 0 K, this highest occupied state is known as the Fermi level E_F, but we will use the convention where E_F shares its definition with chemical potential μ, in the Fermi-Dirac distribution, which describes the energy at which there is a 50% probability that an occupied state will be found. We make this distinction because in semiconductors and insulators, the Fermi level is found within

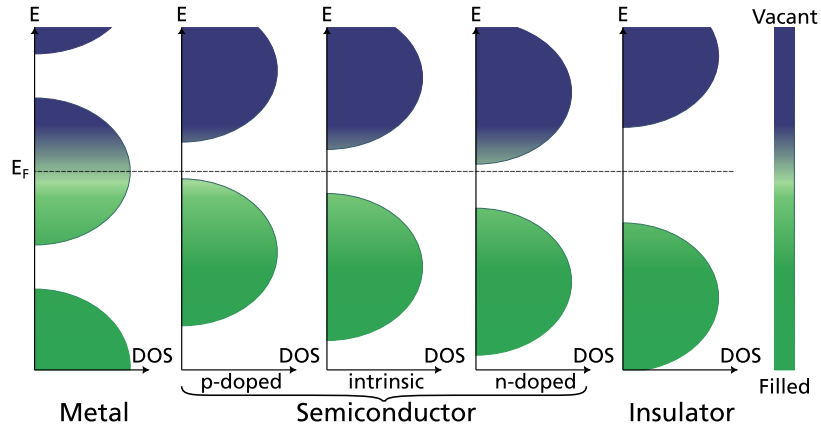

Figure 2.1: Density of states illustrating the differences between metals, types of doped semiconductors, and insulators in terms of the relation between each materials valence and conduction band relative to the Fermi level. Here, filled states are green, empty states are blue[45].

the energy range of forbidden states, making the highest occupied state less useful as a description. Specific names are given to the bands nearest to the Fermi level in the case that its situated in the bandgap. The first band below the Fermi level, or the highest energy band before the bandgap, is known as the valence band, whereas the first band above the Fermi level, or the lowest energy band above the bandgap, is known as the conduction band, with the energy difference between them being known as the bandgap E_g. From this, metals are distinguished from semiconductors and insulators, as illustrated in Figure 2.1.

Semiconductors and insulators, alike in that their Fermi level is found in the middle of the bandgap, are traditionally differentiated from one another by the size of their bandgap. From this, I would have liked to provide a strict definition of how large a material's bandgap would need to be to classify it as an insulator, but even for this there's debate about where to draw the line. Most cases seem to settle on the semiconductor-insulator cut-off as being between $E_g = 3 \rightarrow 4$ eV[46–48]. However, since some materials both within and outside of this range, like gallium nitride (3.4 eV)[49] and even diamond(5.47 eV)[50], are sometimes referred to as wide bandgap semiconductors due to their use in semiconductor applications[51, 52], this definition becomes less useful. An alternative to this, would be to instead define semiconductors as materials with a bandgap, whose electronic properties and band structure can beneficially be modified, such as through doping and control over alloy stoichiometric, to enable their use in semiconductor applications.

2.1.1 Semiconductor Doping

The amount of electrons in the conduction band and the number of missing electrons in the valence band (called holes, treated as positively charged particles) are the carriers that will be able to move around in the semiconductors, enabling them to carry a current. The

carrier concentrations of electrons and holes are referred to as n and p respectively. In an intrinsic semiconductor, meaning it has not been doped, at thermal equilibrium, these are both equal to the intrinsic carrier concentration n_i.

As illustrated in Figure 2.1, dopants, such as impurities or vacancies, modify the Fermi level of a material by altering the charge carrier concentration by removing or adding free electrons, and are consequently categorised by the number of valence electrons they have relative to the semiconductor material being doped.

As an example, let's discuss this in the scope of what many consider to be their favourite semiconductor. Si is a group IV semiconductor, which means that it has four valence electrons, and as such we want our dopants to be in either group III or V due to their valence electron number adjacency. Here, the group III material, let's say In, is known as

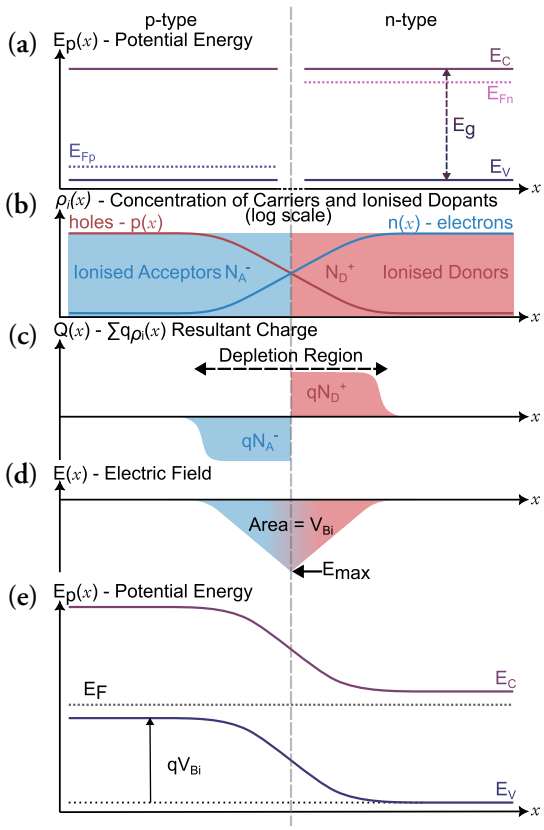

Figure 2.2: A sequence of x-axis aligned graphs showing (a) potential energy band diagrams of two fully isolated doped segments. (b) Concentrations of charge carriers p and n, and ionised acceptor-donor dopant concentrations N_A^- and N_D^+. (c) Resultant charge from summation of carriers and ionised dopants. Charge neutral regions are where $p = N_A^-$ and $n = N_D^+$. (d) Electric field induced by resultant charge in depletion region, whose area represents the built in potential V_{Bi}. (e) Potential energy diagram showing band bending that results in the alignment of each segment's Fermi level across the created p-n junction at equilibrium.

an acceptor, introducing vacant energy levels near the valence band. These intermediate states significantly lower the energy required, compared to the full bandgap in intrinsic silicon, for the thermal excitation of valence band electrons to result in the creation of mobile hole charge carriers, leading to an increased carrier concentration. Conversely, the group V material, let's say P, is known as a donor, instead introducing filled energy levels near the conduction band, which instead produce mobile electron charge carriers from the reduced energy required to 'donate' these electrons into the conduction band. We say that the type of doping resulting from acceptor materials is p-type, and those from donors is n-type. A nice way to remember this is that p-type doping produces positive charge carriers, and n-type doping produces negative charge carriers, and if two sequential segments of a semiconductor are differently doped, we get one of the more well-known semiconductor devices, namely the p-n junction diode.

At thermal equilibrium, the Fermi level in each doped segment of a p-n junction diode must be aligned, but since the Fermi level in each doped segment has been altered by doping, the bands must bend to let these meet. With reference to Figure 2.2, we will now go over this. The introduction of acceptor levels in p-doping facilitates the creation of hole carriers in the valence band by accepting electrons from it. Conversely, n-doping introduces donor levels, which readily donate electrons into the conduction band. In each case, the Fermi level moves relative to which band has experienced an increase in carrier concentration as a result of doping: towards the valence band in p-doping, and towards the conduction band in n-doping. When not in equilibrium, it is common to refer to each doped segment's individual Fermi level as the quasi-Fermi level, labelled as E_{Fp} and E_{Fn} for the p- and n-doped segments respectively in the figure. Majority carrier concentrations at sufficient levels of doping can be assumed equal to the concentration of ionised dopants, but where the doped segments meet, recombination between holes and electrons occur causing a rapid drop in carrier concentrations, exposing the dopant ions in that area, as can be seen in (b). This results in the formation of a region in depleting of carriers, aptly known as either the depletion region or the space charge region, where an electric field forms between the negatively charged acceptor ions in the p-type material, and the positively charged donor ions in n-type region. This electric field results in a drift current that keeps the region clear of charge carriers. The width and magnitude of the electric field of this segment is dependent on the applied bias V_{app}, the dopant concentrations N_A and N_D and the dielectric constant of the semiconductor material ε_s[45, 52].

Sufficient doping is required to achieve adequate carrier concentrations for device operation. In particular, a high doping increases the availability of mobile charge carriers, which directly influences junction behaviour. If one side is more lightly doped, or not doped at all, then the depletion region extends primarily into this side. As an interesting side-note, in the extreme case where e.g. $N_D >> N_A$, and where $N_A >> n_i$, the n-doped region will behave almost like a metal, causing the junction exhibit characteristics of a metal–semiconductor interface, also known as a Schottky diode[45]. While this offers benefits such as unidirectional conduction and fast switching speeds, it lacks the carrier

populations required for efficient light absorption or emission. Since our optically communicating devices require both efficient light absorbers and emitters, we will next discuss the two types of single junction doping strategies most commonly used for these purposes.

2.1.2 P-N and P-I-N Junction Devices

We now move our focus to the function that p-n and p-i-n diodes serve in the context of this work. Figure 2.3 shows simplified diagrams of a p-n junction at varying applied bias, each paired with a band diagram that shows how each of the labelled properties change in response. At no applied bias, in the short circuit case shown in (b), we see how the equilibrium band bending places the potential energy of the p-type conduction band above the n-doped region as a result of E_{Fn} and E_{Fp} aligning at E_F. This also means that drift and diffusion currents are equal. In comparison, at reverse bias in (a), the applied bias increases the potential barrier height so substantially that the drift current dominates, since most electrons no longer have sufficient energy to diffuse over the barrier. This also increases the depletion region width. Conversely, at forward bias in (c), we see a lowered barrier height, resulting in increased diffusion current over the junction, the characteristics of which we will discuss in the next section, and a reduction in the depletion region width.

If selecting materials and dopants carefully, devices tailored to efficiently perform one of several beneficial light-matter interactions can be created. The first, and arguably most significant for its potential applications in sustainable energy, is the electron-hole pair generation from photon absorption. The second, already commonplace in displays and LEDs, is the radiative electron-hole pair recombination, resulting in the emission of a photon whose energy matches the bandgap. Both of these concepts are illustrated in Figure 2.4.

For single-junction LED applications, a bandgap in the range 1.68 - 3.26 eV would

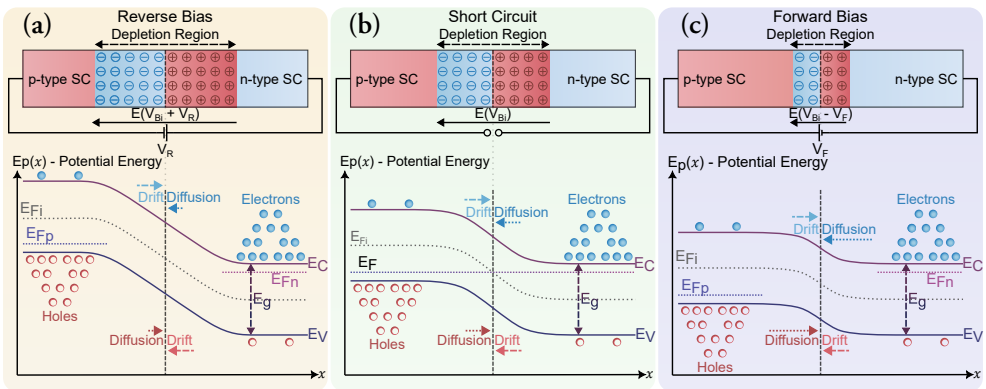

Figure 2.3: Simplified three part diagram illustrating how the properties of a p-n junction changes when the circuit is (a) reverse biased (b) set as a short circuit (c) forward biased. Each diagram shows how the locations of quasi-Fermi levels E_{Fn} and E_{Fp}, drift and diffusion currents, the electric field, and the depletion region width have changed in relation to the intrinsic Fermi level and the conduction and valence band positions in the equilibrium state.

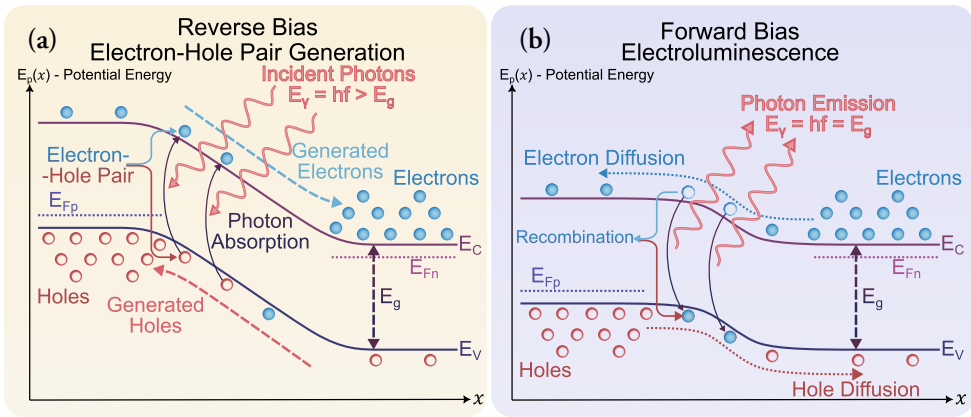

Figure 2.4: (a) Electron-hole pair generation in a reverse biased p-n junction. (b) Radiative recombination in a forward biased p-n junction.

produce visible light. On the other hand, the compositional stoichiometry of ternary and quaternary semiconductor alloys can be tuned in order to achieve a range of bandgaps suitable for targeted emission, as can be seen in Figure 2.5. This concept also applies to single-junction solar cells, where the bandgap should be tuned to achieve maximum possible photon-electron conversion from the irradiance of a target light source. Normally, this would be the sun, but in our case it will be a NW light emitter on the same chip.

A forward biased p-n junction, with its short depletion region width and high diffusion current, promotes radiative recombination through a high concentration of electrons and

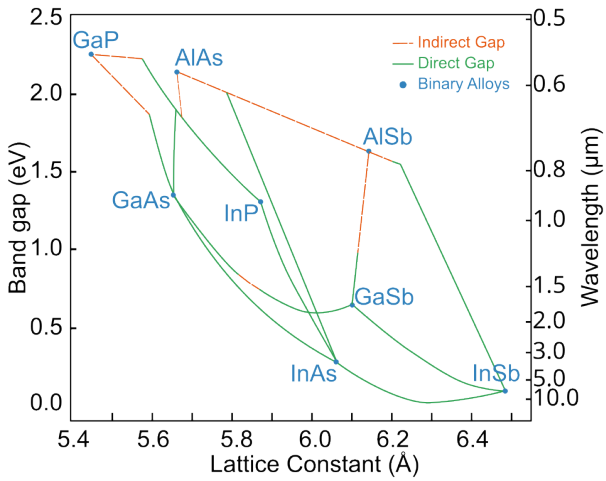

Figure 2.5: Bandgap as a function of the lattice constants of several III-V semiconductor compounds and their ternary and quaternary alloys. Redrawn based on data in [53, 54]

holes at the junction centre, while also minimising self-absorption. However, this configuration is not well suited for solar cell or photodetector applications, since we want to provide a sufficiently large absorption volume where electron-hole pair generation can be induced by photon absorption. This is usually solved by separating each doped segment with an intrinsic one, which greatly increases the depletion region width. Not only does this increase the absorption volume, but it provides a better long-wavelength response in bulk semiconductors, which can be further improved by the use of a sandwich like sequence of heterojunctions[55, 56].

We envision combining multiple light-emitting and absorbing nanoscaled device components with different target bandgaps such that we create what can effectively be described as energy-tiered multiplexing. If we wish to limit wider bandgap materials from communicating with lower bandgap components, we can either tune the absorption cross-section[20] or the relative orientation to the emitter, altering the photocurrent generation due to the change in polarisation sensitivity[57, 58].

2.1.3 Diode IV Characterisation

The current through an ideal p-n or p-i-n junction diode can be described by Shockley's ideal diode equation[59]

$$I_D = I_S \left(e^{\frac{qV}{nk_BT}} - 1 \right) - I_\gamma \tag{2.1}$$

where I_D is the diode current, I_S is the dark saturation current, n is the ideality factor, and I_γ is the induced photocurrent under illuminated conditions, which is otherwise considered to be zero. Figure 2.6 (a) shows the general diode characteristics under illuminated and dark conditions, including a threshold known as the breakdown voltage, normally culminating the rapid onset and exponential growth of the reverse current in an avalanche breakdown[60], something which Equation (2.1) does not account for. A so-called 'ideal' diode, as described by Equation (2.1), has an ideality factor $n = 1$. This corresponds to a device capable of achieving large output currents due to minimal recombination losses, thereby preserving most of the drift current through the junction. In practice, however, the ideal output from many types of diode devices will not be achieved at $n = 1$, such as LEDs whose primary function relies on radiative carrier recombination. Additionally, trap states resulting from crystal imperfections also contribute to an increased ideality factor, as they raise overall recombination rates in the junction, radiative or not[15]. Consequently, the ideal LED will have an ideality factor closer to $n = 2$[61], whereas ideal solar cells and photodetectors, whose junction recombination losses are detrimental to their performance, will have ideality factors closer to $n = 1$. From this, we can see that determining the ideality factor is an important metric for identifying the primary recombination mechanisms in diode devices. We normally determine n by fitting Equation (2.1) to the measured dark

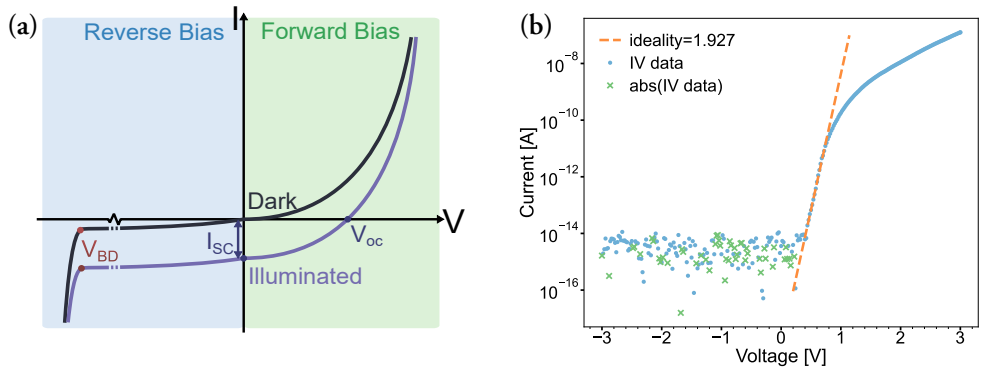

Figure 2.6: (a) Labelled forward and reverse IV characteristics of a p-i-n junction diode under dark and illuminated conditions. Properties like the breakdown voltage V_{BD}, short-circuit current I_{sc}, and short circuit voltage V_{oc} are clearly labelled. (b) Shows the log scale plot of a dark IV curve from a measured InP device, demonstrating which region of the data that Equation 2.1 is normally used for the fit.

current within a narrow range just beyond the forward voltage, an example of which can be seen in Figure 2.6 (b).

2.1.4 III-V Semiconductor Nanowires

NWs are a hot topic in current research due to their many potential applications for quantum-[30–32], sensing-[62–64], low power transistor-[65, 66], LED-[67, 68] and solar technologies[21, 23, 69–72] in subwavelength nanoelectronics. As we will discuss briefly in the next section, NW growth uses far less of the costly III-V materials, while facilitating direct control over the morphology, composition and doping profiles during synthesis. This enables the incorporation of a wide range of dopant- and material-defined junctions on each single NW, allowing for a variety of semiconductor devices to be directly grown along its length. Different junctions can also be combined sequentially in tandem NWs to efficiently target different parts of the solar spectrum[24–26, 73], or even the wavelength of another light emitting on-chip component. Morphological control over the diameter and length can increase the absorption cross-section for a target wavelength[69, 70], or can enhance polarisation sensitivity at higher aspect ratios[33, 74].

NWs, for optical applications, are most commonly grown standing in compact uniform planar arrays, and when electrically interconnected in parallel via a transparent conductive layer can function collectively as a solar cell. In this configuration, each NW acts as an independent photovoltaic unit, scaling the total output power with the number of contributing nanowires. This results in a high fault resistance, as damage to parts of the array only marginally reduces the power output, making them particularly suited for space applications[24, 75], since remote repair is impossible.

InP based NW solar cells have already shown high efficiencies in both single-junction[21, 72, 76], and multi-layer tandem[26, 77] structures. For us, the high single junction per-

formance of InP NW photovoltaics is what led us to pursue their use as receivers, and to some extent as emitters, in our bid to create an optical broadcasting network. To replicate the synapse response described in [40], an ongoing project aims to make use of single InAs NWs as the channel in a MOSFET device, gated by two oppositely connected InP NWs acting as the activating and inhibiting ends respectively. Being a narrow bandgap (0.35 eV) material that retains electron mobilities almost a magnitude greater than Si [78, 79] while in a NW form factor, it already meets several requirements necessary to replicate synapse spiking behaviour. It has already been used to demonstrate a sigmoid switching response from a 0.1 V 230 fJ spiking event[80], where the biological equivalent is 30 fJ per synapse event, and 60 pJ per spike[9, 37, 38]. This low voltage requirement, beyond being comparable to nature, is also necessary due to the low expected signal from the InP NW receiver pair, whose summed activation and inhibition response will gate the eventual MOSFET in the ongoing project.

Finally, an ongoing continuation of the work done in Paper IV, which we will discuss more of at the end of Chapter 5, intends to make use of grown $In_{0.427}Ga_{0.572}P$ LEDs[1], with a centre emission wavelength of 650 nm, as an on-chip photobleaching agent. This stoichiometric composition was chosen to target the wavelength at which the rate of photobleaching was greatest in the dye. While an external light source was used for the photobleaching in Paper IV, establishing a proof-of-concept memory based on only on-chip components would move us one step closer to realising a device inspired by the neural architecture of the Stone model[40] summarised in the introduction.

[1]Grown by Mariia Lamers

CHAPTER 3

An Overview of The Principles of Nanofabrication

'On ne saurait faire d'omelette sans casser des œufs.'
—François de Charette

From the bygone era of vacuum tube assemblies[81], Jack Kilby's first integrated circuits device[82], and the hand-drawn masks on Rubylith[83], integrated device design has advanced so far that optical microscopes can no longer be used to observe the finest of features. On an industrial level, the state of the art tools that can simultaneously achieve nanoscale and macroscale resolutions in one step exist[6], but are so prohibitively expensive and specialised that they are unfeasible for use in research, where rapid iteration and prototyping is necessary for advancement. Naturally, one could easily make the assumption that we, in this work, are resolution-limited as a consequence of the cost, but alternatives exist; we can combine the large-scale processing of diffraction limited optical techniques with the fine nanoscaled precision achievable with electron beam-based techniques. Together, these allow us to achieve industrial level precision compatible with all other fabrication techniques. This chapter will discuss the design principles, fundamental fabrication methods and the theoretical background of the process by which nanoscale device architecture is defined for on-chip applications.

3.1 Lithography

Lithography is the selective pattern transfer from one planar medium to another. Unlike the printing press, where pattern transfer is done by the arrangement of ink soaked letter stamps in a frame to be pressed directly into paper, the concept of lithography relies on how the surface treatment modifies the transfer substrate in such a way that only the intended regions can pattern transfer. Invented in 1796 by Aloys Senefelder, the original scheme involved 'patterning' a limestone slab with an oil based substance, then treating it with a weak acid and gum arabic, making all parts outside of the pattern hydrophilic. For pattern transfer, the entire slab would be soaked in water, causing all of the non-patterned region to become water-saturated, and oil repelling, such that when the ink is applied to

everything, only the patterned region would retain the oil, allowing the pattern transfer of the ink-covered patterned region to another surface[84].

Modern fabrication still relies greatly on a variety of lithographic techniques, the most common of which make use of specific polymers, known as a resists, whose state of solubility is altered when exposed to a specific type of radiation. Resists that become soluble after exposure are known as positive resists, whereas those that become insoluble are known as negative resists. In combination with intricate masks, pattern transfer is done through the selective exposure of the resist, such that when a chemical known as a developer is exposed to the sample, all resist material made, or remained, soluble during the exposure will be removed. Material deposition can either be done after development, where the resist removal process, also known as lift-off, sees only the material deposited on top of the resist being removed. Or, alternatively, material deposition can be done before resist coating, where the mask pattern transfer reveals areas that are to be removed by wet chemical etching. As a consequence, these resist types can be used interchangeably simply by inverting the mask, although it is typical to use the resist and accompanying mask that exposes the smallest area of the sample. This, in conjunction with metal evaporation, lays the foundation for how metal contacts are defined on a substrate, which is one of the fundamental bases from which nearly all device chips are made today. There are various types of lithography used for nanofabrication, but for this work, we will limit discussion to two main methods, namely photolithography and electron beam lithography (EBL), due to how their combined use is a requirement for nanoscale development in research. All mask patterns are created using a computer aided design (CAD) software, which in our case is the open source KLayout[85]. For the remainder of this thesis, we will be referring to digital mask files by the database file format used to store them, namely the Graphic Design System (GDS) file (technically GDSII). This is an industry standard for electronic design automation and integrated circuit layout.

3.1.1 Lift-Off Technique

The main method used for pattern transfer in this work is called lift-off. Due to the methodological overlap between photolithography and EBL, we will first discuss shared features, before delving into specifics. Figure 3.1 illustrates the complete procedure by which metal contacts can be defined on a sample by photolithography or EBL, culminating in this lift-off which leaves behind device contacts in regions defined by the mask.

All processing begins with an extensive cleaning step, where the substrate sample is treated in a sonicator while submersed in a solvent, usually for a minute each. For us, this meant once in acetone, and then twice in two separate beakers of isopropyl alcohol (IPA), after which the sample is baked on a hotplate at 180 °C for 5 minutes. The stronger solvent, acetone, removes most organic residues and oils left on the sample, with added sonication shaking loose any adsorbed or weakly attached materials from the substrate. The main pur-

pose of the IPA is to dilute and remove the acetone, which would otherwise leave residues after drying. Baking the sample at high temperature on a hotplate ensures that no solvents remain on the substrate. After this cleaning process, any number of required resist layers can be spin coated onto the sample.

Spin coating is the process by which a substrate wafer, or small chip, can have a thin film of a liquid evenly coated over its surface. The sample is attached by vacuum to a hopper mounted on the motor arm of a spin coater and the polymer is pipetted to sufficiently coat the surface. In this tool, the ramp speed, max rotations per minute (rpm), and duration can be modified so that a thin film of desired thickness and uniformity can be produced from the deposited material. It is this process that most requires the absence of debris and oils, since any particulates will cause non-uniform streaks to form over the surface, which is suboptimal for both exposure and lift-off. After each resist is spin-coated onto the sample, it must be baked at a specific temperature for a sufficient period of time for it to dry out, increasing stability and adhesion to the substrate, and permitting subsequent layers to be added without mixing.

We make use of two consecutive layers of resist in both UV and EBL methods in order to form an overhang such that the metal deposited on the substrate and on the resist do not fuse before lift-off, as this would cause them to also be erroneously removed together with the resist. For UV lithograhpy, our first layer is known as a lift-off resist (Lor), specifically designed as a first layer that does not have its solubility to the developer altered by the exposure, which is what causes the overhang to form during development, as can be seen in Figure 3.1-5. This does mean that the development is time-sensitive, requiring sample submersion in a stopper solution, typically deionised water (DI) or IPA, to end the process. For EBL, as noted in step 4c, the overhang is achieved by similar means, where the first layer, while still an E-beam resist, has a lower dose requirement and is more readily soluble in the developer solution even before exposure. This means during development, exposed regions of both resists will develop immediately, but the unexposed first layer will partially dissolve more than the second layer, resulting in a similar type of overhang. The most commonly used type of E-beam resist is Poly(methyl methacrylate) (PMMA).

Table 3.1 contains the resist materials used for nearly all final processing pipelines in papers I, II, and IV, the function of each being tailored to the process performed. Once developed, the risk of resist residues remaining on the substrate surface is high, requiring the use of an oxygen plasma asher. This tool, rather amusingly, is often a modified microwave oven, containing a makeshift vacuum chamber with oxygen (O_2) and nitrogen (N_2) gas intakes for plasma formation and rapid inert-state cooling respectively. For this process, the sample is placed inside the chamber covered by a Faraday cage, the tool is pumped down to 50 Pa before the oxygen valve is opened until the pressure reaches 500 Pa, after which the microwave is turned on for 15-30 seconds depending on the observed development results. This top-down resist etching method relies on the generation of an oxygen plasma by the direct ionisation of the O_2 by high power 2.45 GHz radiation, the same output as a microwave, at low pressure, creating ionised species of O_2 and free radicals,

which directionally sputter onto the resist to remove it from the surface.

With no resist residues left in the patterned region of the sample, we can finally perform contact metallisation. There are several viable methods that result in a uniform deposition of metal species onto a substrate, but in this work we exclusively used evaporation-based deposition. One such system is the AVAC, which is a thermal evaporator in the form of a large drum-shaped vacuum chamber that utilises a carousel of tungsten boats that can be loaded with small beads of the target materials. Passing a high current through the boat

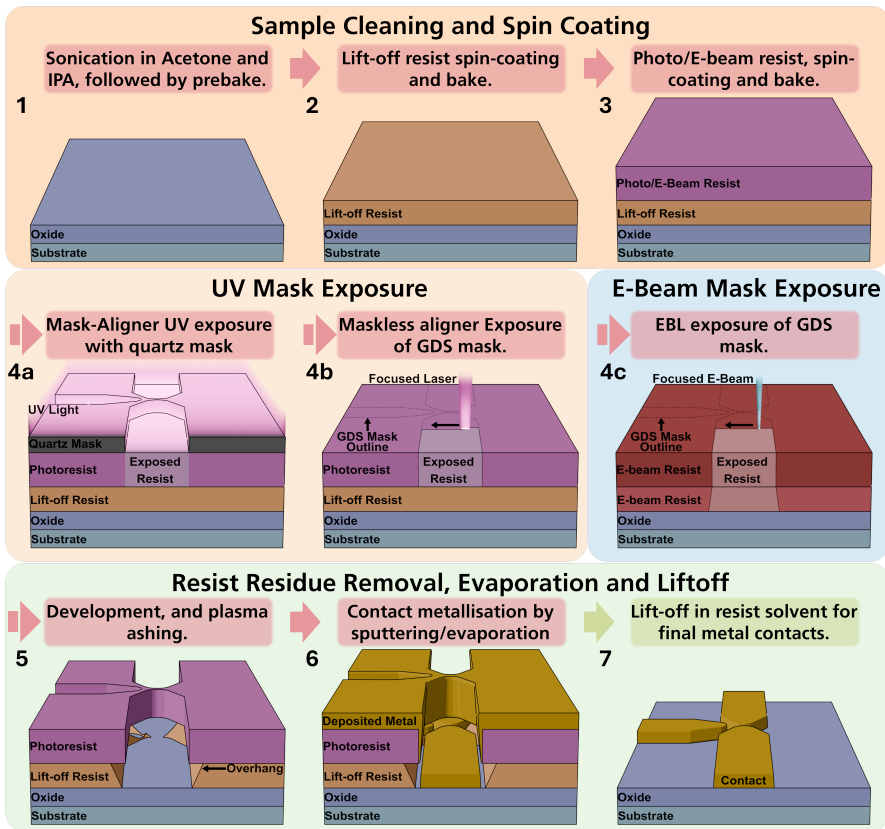

Figure 3.1: Multi-step illustration showing the complete fabrication pipeline for a bilayer UV/E-Beam lithography lift-off procedure. 1 - Substrate cleaning done by sonication once in a beaker of acetone, then twice in two separate beakers of IPA, after which the sample is baked on a hotplate. This removes biological residues, dust, and evaporates adsorbed liquids from the sample surface. 2 - Lift-off resist is spin-coated onto the sample, and then baked on a hotplate. For EBL, this would be a shorter chain length electron beam (E-beam) resist compared to the next layer. 3 - Photo/E-beam resist is spin-coated onto the sample, then baked on a hotplate. 4 - Exposure variants depending on resists used. 4a - Photoresist mask exposure utilising a mask aligner and a pre-fabricated quartz mask. 4b - Photoresist mask exposure utilising an MLA, where the mask layout is provided as a GDS file. 4c - E-beam resist exposure with an EBL, where the layout is provided by as a GDS file, where the overhang generated is caused by the lower chain length E-beam resist having a lower dose requirement, causing overexposure. 5 - Resist is submersed in matching developer solution for a set period of time, if mask pattern transfer appears complete under a microscope, the sample can then be treated in an oxygen plasma asher to remove any resist residues. For the E-beam resists, this outcome is similar. 6 - Contact metallisation via evaporation or sputtering. 7 - Lift-off by sample submersion into a solvent (usually acetone or remover 1165) that dissolves both bilayer resists, leaving only the metal contacts deposited directly on the substrate.

Table 3.1: A table containing the main resist polymers used in the published works.

Resist Name	Type	Purpose
Lor10b	Lift-off Resist	Promotes creation of an overhang during development.
S1813	Photoresist	Mask transfer.
PMMA 5A 200k	E-Beam Resist	Promotes creation of an overhang during development.
PMMA 6A 950k	E-Beam Resist	Mask transfer.
ARP-6200	E-Beam Resist	Used oxide etching, due to its resistance to ion etching techniques.

induces resistive heating, which is manually altered to achieve a desired metal evaporation and deposition rate at low pressure. This carousel can be rotated between evaporation steps, allowing several sequential material layers to be deposited. This tool was used mainly to evaporate Zinc (Zn), since its high vapour pressure at low temperatures causes it to readily re-evaporate, meaning that once it's inside any evaporator, it will continue to contaminate other films[86]. For most other evaporation recipes, we instead used the more advanced Temescal E-Beam Evaporator (in which Zn is forbidden), which can automatically execute user recipes for any combination of allowed materials. Here, evaporation is achieved by a focused electron beam, that heats the target material deposited in a motor controlled crucible until it vaporises, automatically adjusting the source to achieve a target rate of thin film condensation on the substrate surface, stopping once the target thickness has been reached.

3.1.2 Photolithography

As the name suggests, photolithography uses light as the main means of pattern transfer onto the light-sensitive photoresist. The conventional approach utilises a so-called photomask, shown in Figure 3.1-4a, which is most commonly a slab of quartz where the desired pattern has been defined on its surface as a light absorbing film composed either of chromium or iron(III) oxide[87]. Since sequential layers of a fabrication pipeline might be needed, it is essential that the sample can be re-aligned so each layer of the device design can be matched between masks. This is done manually in a tool known as a mask aligner, where markers on the substrate (if any) can be lined up with matching markers on the mask by manipulating the rotation and translation of the micro-stage. Exposure is performed by elevating the sample until soft, or hard contact, is reached against the mask itself, and then selecting dose and exposure times for the UV lamp.

An alternative, and more modern, approach to this exposure, is shown in Figure 3.1-4b, which is a maskless aligner (MLA) system called the MLA-150 that uses a focused UV laser to directly write out features defined in a GDS file. Here, the sample centre is automatically aligned to by the system, and any further alignment can be done by providing the co-ordinates of markers on the sample, which will then be imaged for a final manual

readjustment to a local second layer accuracy of ± 250 nm[88]. In the MLA-150, exposure can be done either with a 375 nm or 405 nm laser, achieving minimum feature sizes of 0.6 μm and 1 μm respectively at the cost of slightly increased exposure times for the shorter wavelength for less dense patterns. For a 4 inch waver, the expected time required to pattern a mask of any feature density and wavelength is at most around 35 minutes. While a standard mask-aligner system can easily achieve rapid sequential patterning of several 4 inch wafers, the mask-less system has great versatility in prototyping, since it does not need a physical mask to be manufactured for its use. In industry, however, extreme ultra violet (EUV) lithography, targeting a wavelength of 13.5 nm, is capable of patterning the resolutions required for the ever shrinking feature sizes found in modern transistor device architectures, from 10 nm down to the smallest currently possible feature width of 0.4 nm if grown epitaxially[89]. In our lab, however, we must make use of another alternative method to define the nanoscale contacts required for our nanowire device architectures.

3.1.3 Electron Beam Lithography

In most non-industrial research, EBL tends to be what bridges the resolution gap between the large scale feature sizes that can be defined by photolithography, to the nanoscale contacts required for the fabrication of modern transistor device architectures. The tool that performs the lithography is, half-paradoxically, referred to as 'an EBL', and makes use of a focused electron beam to write the very same type of digital GDS mask that the mask-less aligner uses into a target resist. For this work, we used a 50 keV Raith Voyager EBL, for all nanoscale pattern transfer. Its electron source is a thermal field emission gun, from which a beam is shaped and focused using a series of apertures and electromagnetic lenses down an electron column held at a high vacuum. For this tool, focusing, beam stigma correction, stage and beam deflection calibration are all done mostly automatically with provided python scripts. Only the step size and dose factor after this must be chosen.

Inserted samples will naturally have layers of spin coated electron sensitive resist, meaning that observations of the sample should be limited to avoid overexposure. With a well-designed template pattern, edge feature identification should allow both angle correction, and a direct stage drive in U-V to a designated origin location without any exposure to other parts of the sample. GDS files can now be loaded to set locations in UV from the origin, after which, if EBL markers exist, a final manual image alignment can be performed.

3.1.4 Designing a Template for Nanoscale Devices

In this thesis, all devices that will be discussed are made from nanoscale components that must be manually placed and contacted on a substrate. One cannot simply transfer nanometer sized components to a smooth substrate sample, spin coat it after imaging, and eyeball stray features of the chip to place contacts with nanometre precision exactly where you intend them to be. It is necessary to have a robust, and purpose-designed device template that simplifies the process of placement, on-chip navigation, and contact design, reducing

both the amount of exposure time needed in the EBL, and limiting the amount of imaging on the resist coated substrate needed. This is why I designed the GDS photo-and-EBL template pattern for all our devices seen in Figure 3.2. My 'Device FRankenstein' (DFR) template, named so for its intended purpose of housing artificial optical neural networks, achieves this. Pay attention to the device naming conventions here, because I will refer to them using this from now on. As stated prior, we use KLayout for our GDS files. I designed the single flower pattern for seamless tiling at any edge, the same idea being applied to the dice marks and corner alignment crosses of the 5×5 device chip. KLayout has an integrated python API, which is a powerful too I used for some level of automation. Here, it was used to optimally tile the 5×5 chip inside the bounds of any provided wafer dimension. During this tiling, each device chip is also given its own label based on the sample design iteration, with alphabetical column and row lettering, which is what gives us the device name DFR1-JK in the figure example. Directional labels along the outside edges of

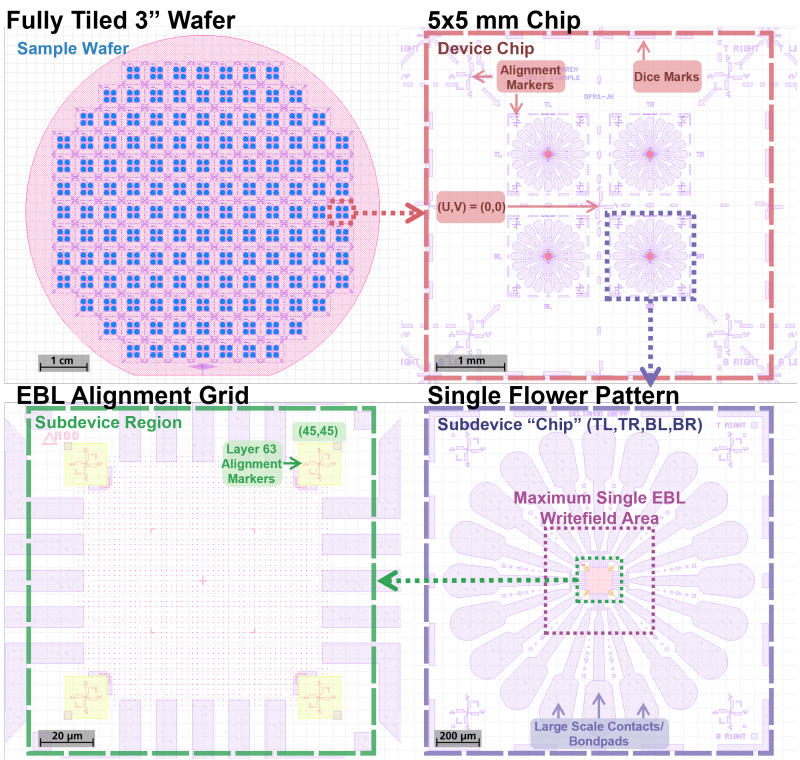

Figure 3.2: Different zoom levels the device template used for nearly all fabricated nanodevices in this work. Large scale contacts and alignment features shown in blue are intended for photolithography, whereas red structures within each quadrants subdevice region requires EBL processing. Edges of each 5×5 chip are lined with dice marks and midpoint markers, directing users towards the labelled U-V origin. Chip corners and quadrants are also labelled with directional text, indicating which top/bottom/left/right section of the chip is being observed. Each chip is also given a unique label, in this case DFR1-JK, representing sample design 1, column J, row K. Layer 63 alignment crosses are EBL elements used for manual alignment when exposing final nanocomponent device contacts in the subdevice region.

quadrants, and at chip corners (e.g. T Left/TL) allows post-correction of nanoscale contact designs if the chip was inserted into the EBL sample holder at an angle. Dice and midpoint markers can be used for the initial angle correction, after which their position in the GDS file can be used to drive the stage directly to the U-V origin. This approach avoids direct exposure to any of the subdevice chip regions, and more rapidly identifies enough features to navigate the chip without any further visual aid. With a symmetrical list of quadrants, positionlist entries from (U,V) = (0,0) in the EBL can be trivially entered. I specifically chose to limit the subdevice region to 100×100 μm, in order to avoid stitchfield writing on both tools we have available in the lab.

3.2 Additional Tools and Techniques

Beyond the essential tools required for simple device contacting, there are a few more techniques whose importance to modern semiconductors, and systematic analysis that cannot be understated.

3.2.1 Atomic Layer Deposition

High-κ materials are essential to the design of nearly all modern semiconductor device architectures. Beyond their use as a gate dielectric for a variety of FET and MOS devices, common oxides deployed in CMOS architectures, like (HfO_2)[90–92] and aluminium oxide (Al_2O_3)[93, 94], are also well suited for use as waveguide materials for integrated opto-electronics. What's more fortunate, is that one of the more common methods employed for the growth of these oxide materials is atomic layer deposition (ALD), which makes use of two separated half-cycle gas-solid reactions to grow sequential layers of a desired material. The working principle on how this growth is achieved can be seen in Figure 3.3. In the first half-cycle, gaseous H_2O is pulsed into the chamber, where OH groups adsorb homogeneously to substrate surface, self terminating after all reaction sites are filled. Since no further adsorption can occur, the chamber is purged with nitrogen, readying it for the second half cycle. The metal-organic precursor is then pulsed into the chamber, replacing the hydrogen with a more stable $-Al(CH_3)_2$ group and CH_4, which is then purged from the chamber. H_2O is pulsed once more, where the $-CH_3$ group is replaced by oxygen, and OH groups, which self-terminates as the first stable layer of oxide. Remainder OH groups on Al atoms now substitute for the surface $-OH$ groups in subsequent cycles. This process, by its very nature, allows for ångström precision control over the grown film thickness.

While ALD may sometimes produce amorphous film, it is possible to fine-tune parameters like chamber pressure, pulse length, wait and purge times, temperature, and the purge gas composition to produce highly homogeneous films, with high crystal purity[93, 95]. In this thesis, we worked mainly with the metal-organic precursor TMA for the growth of Al_2O_3, whose purpose was to act as planar waveguides for opto-electronic components.

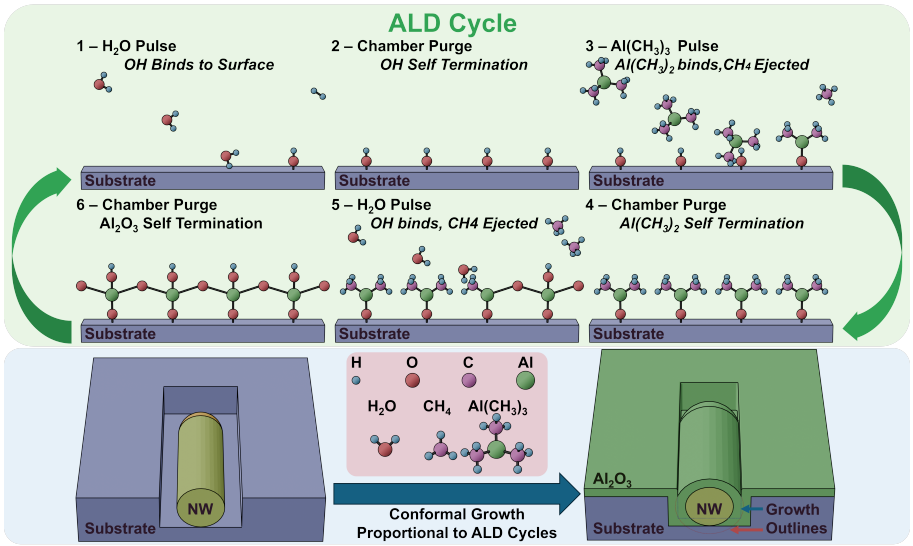

Figure 3.3: An example sequence of a single ALD cycle for the $\mathrm{Al(CH_3)_3}$ (TMA) precursor. It should be noted that the first two steps only happen once, further cycles looping between steps 2-6 after this.

InAs FET devices studied in an ongoing project instead makes use of a $\mathrm{Hf(N(CH_3)_2)_4}$ (TDMA-Hf) precursor for the growth of HfO_2, acting as the dielectric gate material.

3.2.2 Ellipsometry for Growth and Etch Rates

Naturally, a downside of planar waveguides is that surface level device contacts no longer become directly contactable either by probe or wire bonding means. The solution we found for this involved reusing the MLA mask discussed in section 3.1.4 with everything but the ends of each flower petal bondpad removed, allowing us to perform wet chemical etching with aluminium etchant type A, to reveal the contacts once more. Even though the etchant is advertised as aluminium selective, due to the large area we need to etch, we wanted to avoid any large undercutting of the resist to protect our III-V devices. As such, we had to measure the etch rate using a tool known as an ellipsometer.

Ellipsometry is a technique used for determining the thicknesses of one, or multiple, optically transparent films on a sample substrate. This is done by measuring the amplitude components of polarised light Ψ, and phase shift Δ, which can be seen visualised in Figure 3.4 (b). Together, they can be used to determine the ratio of the complex Fresnel reflection coefficients r_s and r_p, also known as the complex reflectance ratio ρ. When measured at various incidence angles and wavelengths, a fit can be built up for a model function, whose simplified expression is given by

$$\rho = \frac{r_p}{r_s} = tan(\Psi)e^{j\Delta} = f(n_i, k_i, t_i), \tag{3.1}$$

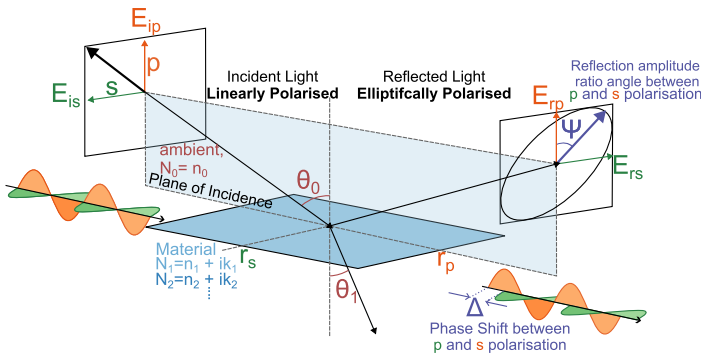

Figure 3.4: Diagram illustrating the relation between incident and reflected light in an ellipsometer measurement, and how these parameters relate to the expression in Equation 3.1.

which can solve for the refractive index n and the extinction coefficient k, also known as the optical constants, and the film thickness t[96]. This function can be one of many models, but the two most common ones are Cauchy's law and Sellmeier's law, both of which are empirical models describing the relationship between the refractive index and wavelength for a transparent medium[97, 98].

As a user, you are fortunately only responsible for knowing what's on your sample, and whether or not its thickness can be determined by the ellipsometer. The variety of use case for this tool is quite extensive, and in our work we have used it for, including but not limited to, measuring: spin curves of resist materials, ALD oxide thickness and per-cycle growth rate, and etch rates of both wet and dry etching techniques, all of which follow the same measurement principle. Before anything else, we measure the sample, saving a model containing the substrate material and fitting for the native, or thermally grown, oxide. After this, either we stepwise deposit material, measuring and fitting for the new material and thickness. If we are measuring the etch rate, we instead begin from a before-etch sample, and then perform multiple different durations of etch soaks, fitting the model anew between each step.

3.2.3 Dry Etching Techniques

For the fabrication of our devices, we made use of three different forms of dry etching techniques. As briefly mentioned in the lithography section, all samples are treated to 15 seconds of oxygen plasma ashing after development. This is done in my favourite tool, namely the plasma preen shown in Figure 3.5[99], which is a microwave oven converted to house a glass vacuum chamber for non-directional oxygen plasma etching. The 2.45 Ghz microwave oscillator is repurposed to produce reactive free radical oxygen species at low pressure, which in turn sputter or react with surface elements, cleaning it. This, however, is a non-directional process, meaning it cannot be used to etch deep grooves into substrate materials. For this, we instead make use of reactive ion etching (RIE) (which we perform

in a tool known as the Trion Sirius T2) illustrated in (b). While it has chamber inlets for up to seven different process gases, we only made use of trifluoromethane (CHF_3) due to its highly controllable etch rate of SiO_2. Similar to the plasma preen, a reactive ion plasma is created using a radio frequency (RF) generator, where the directional etching is induced by the acceleration of the reactive elements towards the sample chuck over an applied RF bias.

Not shown in the figure, is the argon (Ar) plasma milling that we used to remove the native oxide from our NW devices before metallisation. Similar to the plasma preen, a 2,45 GHz magnetron generates the Ar ion species, where extracted ions are accelerated through to the intake using a direct current (DC) acceleration voltage. Due to Ar being an inert gas, the milling reaction is purely kinetic, meaning each atom at the surface is mechanically removed by accelerated Ar ions.

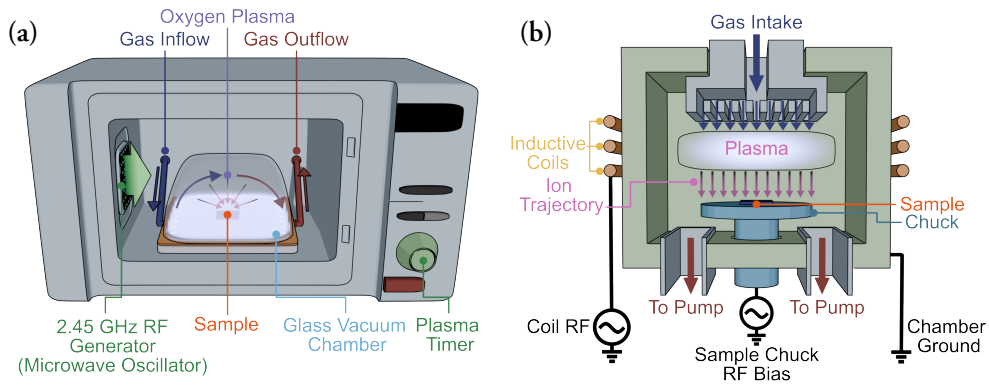

Figure 3.5: (a) Depiction of the plasma preen oxygen plasma ashing system. (b) Cross-section of the Trion T2 RIE.

3.2.4 Nanowire Growth

Since all device architectures that will be discussed in subsequent sections are based on III-V NWs, we will briefly discuss how they are grown. Figure 3.6 illustrates the three main approaches to NW fabrication. The first approach, and perhaps most simple to grasp, is where an inverted growth mask is used, and an anisotropic etching technique, like RIE[100], is used to remove the substrate material around where the mask had been defined. Isotropic techniques, like standard wet chemical etching can only be used for much smaller aspect ratios due to rapid undercutting, meaning that the material pillars that remain are shorter and thicker. Not all wet chemical approaches are isotropic, such as the metal-assisted chemical etching, where a metal catalyst mask is deposited on the substrate instead[101, 102]. Etch rates around the metal catalyst mask is greatly enhanced due to the reduced activation energy for the chemical etch reaction, causing it to act largely anisotropically. All of these techniques fall into the category of top-down processing.

For the devices fabricated in this thesis, all NWs were grown using the third ap-

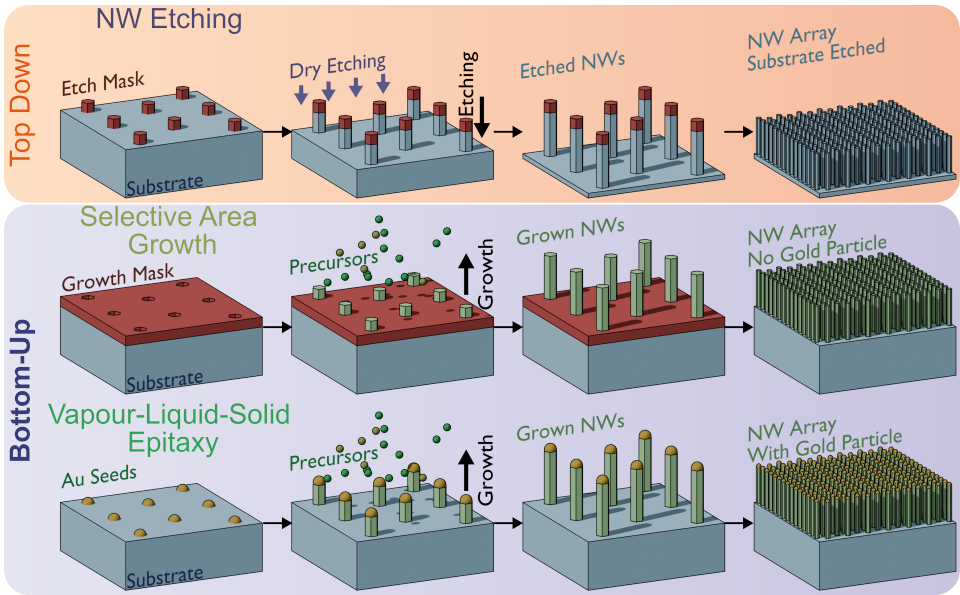

Figure 3.6: Three separate fabrication templates used for the production of vertical standing NWs. All three approaches requires a lithography step to define either a growth mask, or a mask through which Au seeds are evaporated onto the substrate surface.

proach, namely metalorganic vapour phase epitaxy (MOVPE), which is often referred to as vapour-liquid-solid (VLS) epitaxy. Here, precursor gases with the desired elements (e.g. trimethylindium, and phosphene for InP) are injected into the MOVPE chamber together with a carrier gas, where the intended subspecies adsorb on the semiconductor surface to form epitaxial layers. Segment doping is performed similarly by co-injection of dopant species during the growth process, which can be tuned to effectively allow for atomic layer control of doping[103]. Nucleation and material accumulation can either be controlled using a dielectric mask, which is known as selective area growth (SAE), or by using an array of gold seeds. In this thesis, we exclusively used NWs grown using Au seeded MOVPE,[1] where an EBL lift-off process, outlined prior, is used to deposit the hexagonal array of Au particles onto a growth substrate. This technique benefits from reduced waste of both III-V materials otherwise lost to etching, and the etchant chemicals themselves that are necessary for the definition of similar semiconductor structures in top-down alternatives[104, 105]. Heteroepitaxial techniques can be also used to incorporate III-V materials onto less costly Si, ranging from NWs and thin films to monolithic integration[106, 107], although these typically involve more stringent constraints related to lattice mismatch and defect management.

Grown p-i-n junction NWs can be purposed into a solar cell array through a less

[1]NW growth done by Dávid Alcer and Mariia Lamers

complicated process than what is required for multi-NW assembly, often just requiring full-coverage spin coating and surface etch of the transparent insulator Benzocyclobutene (BCB), followed by top-contact evaporation of the transparent indium tin oxide (ITO). For us, however, as special interest lies in making use of the advantageous optoelectronic properties of more than one species of III-V semiconductor NWs, devices cannot be fabricated directly on the growth substrate. Instead, the means of assembly and individual contacting pose the greatest challenge, which we will cover in Chapter 5.

CHAPTER 4

Finite-Difference Time-Domain and Simulating Photonics

'Å, Nangilima! Ja, Jonatan, ja, jag ser ljuset! Jag ser ljuset!'
—Astrid Lindgren, Bröderna Lejonhjärta

Although it may be tempting to jump straight to fabrication when developing complex on-chip optical systems, it is often best to first simulate how aspects of its geometry impacts the intended function of light within it. For instance, one could be looking to optimise the maximum possible absorption or scattering cross-sections of an on-chip component, or attempt to maximise signal transmission between on-chip elements using waveguides or other structures. In this section, I will detail how Finite-Difference Time-Domain (FDTD) simulations can be used to evaluate power absorption, cross-sections, and general behaviour of large-scale optical systems.

4.1 FDTD Solution of Maxwell's Equations

Numerical solutions for electromagnetic field interactions in complex nanostructured geometries featuring both dielectric and metallic, and non-magnetic structures can be evaluated using FDTD. This method, as per the name, is an implementation of time-domain based solutions of the partial derivatives of Maxwell's equations. In particular, FDTD performs this by solving Maxwell's curl equations on a discrete and temporal grid for electric ($\bar{E}$), magnetic ($\bar{H}$), and displacement ($\bar{D}$) field components. The solved curl equations are

$$\frac{\partial \bar{D}}{\partial t} = \nabla \times \bar{H} \tag{4.1}$$

$$\bar{D}(\omega) = \varepsilon_0 \varepsilon_r(\omega) \bar{E}(\omega) \tag{4.2}$$

$$\frac{\partial \bar{H}}{\partial t} = -\frac{1}{\mu_0} \nabla \times \bar{E} \tag{4.3}$$

where $\varepsilon_r(\omega)$ is the relative dielectric constant, ε_0 is the permittivity of free space, and μ_0 is the permeability of free space. For three dimensional space, we have to solve for six

electromagnetic vectors, namely $E_x, E_y, E_z, H_x, H_y, H_z$. FDTD's approach to this is to split these up into two independent 3-parameter equations in two dimensional space, where the z-dimension is considered infinite, namely the transverse electric (TE), composed of E_x, E_y, H_z, and transverse magnetic (TM), composed of H_x, H_y, E_z. These parameters are mapped onto the face and edge structures of a so-called 'Yee-Cell' seen in Figure 4.1, the sum of which builds up the finite domain and can be considered the resolution of the simulation[108]. We will not cover any further specifics on how the solution for each grid

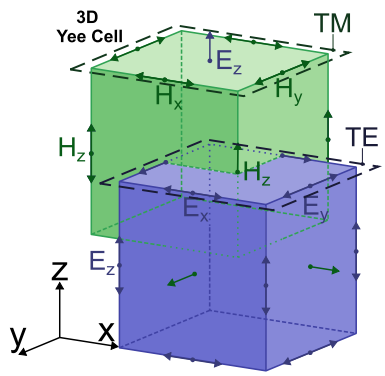

Figure 4.1: Illustration of a Cartesian Yee-Cell, showing the magnetic and electric field vectors considered at each point within the FDTD simulation grid. TM and TE planes are labelled, which is where the independent 3-parameter equations are solved.

point is evaluated in the time-domain. We have a software from the Ansys optical suite known as Lumerical, which solves these interactions for us. Ultimately, we are able to extract information about the total field intensity, power absorption in various mediums, power transmission through waveguides, directionality from antenna structures, plasmon interactions at metallic interfaces etc[108–112].

4.2 Building Reliable and Non-Diverging Simulations

There are many pitfalls when building complex simulation structures in Lumerical's FDTD suite. They range from diverging conditions and small feature sizes, which can be avoided by using the correct mesh resolution for small feature sizes, making use of symmetry conditions whenever possible, and using the correct boundary condition. This section will go over all that.

4.2.1 The Resolution Trade-off

When simulating nanoscale optical structures, one can quickly become RAM limited by the resolution of your simulated mesh, which is why selecting a suitable meshing option is important. As described earlier, the finite enclosed FDTD domain is a dense simulation

grid built up from staggered Yee-cells. The default grid optimisation is an automatic non-uniform meshing option[113] that uses variably sized rectangular cuboid Yee-cells, built up around the more dense areas of the simulation. Uniform parts of geometry, like long stretches of waveguide, do not need the same resolution as the edges of a NW, or an Au particle. As such, we choose to make use of a sparse grid in homogeneous, or planar, stretches of the simulation geometry. Whereas for rounded objects, or diagonally arranged elements, we often specify a mesh area with greater resolution. This is to avoid so-called stair-casing artefacts, which can be seen illustrated in Figure 4.2, which often cause simulations to diverge by solver being unable to find a time stable solution at the interface. With

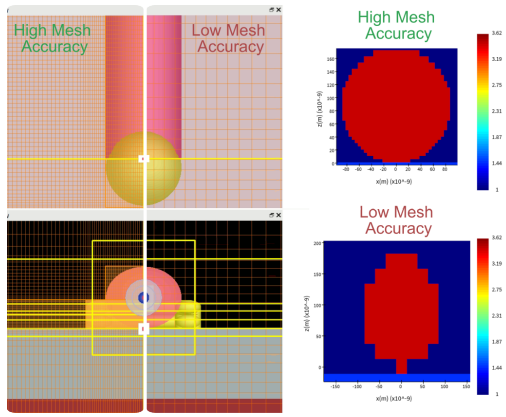

Figure 4.2: Screenshot showcase comparing when a low accuracy of auto non-conformal mesh is used, as compared to when a higher resolution mesh item is placed over the NW. The orange grid lines indicate the Yee cell density. Stair-casing artefacts can be compared in the NW refractive index cross-section shown on the right for both cases.

metal elements, it is especially important that the resolution of the grid around these do not produce significant staircase artefacts, else you risk self-reinforcement divergence occurring. If the resolution cannot be increased further, the DT stability factor can be altered, where a lower number improves numerical stability at the cost of greater simulation times. Beyond this, divergence testing should always be performed. This includes fitting chosen material models, like Palik's for Au[114], against the light source simulation wavelength, and testing mesh resolutions to see where the results begin to diverge significantly from greater resolutions.

4.2.2 Recognising Symmetry and Boundary Conditions

If the simulated system geometry is geometrically symmetric around the injection axis and within the FDTD domain, mesh symmetry can be used to further reduce the time required for simulations, improving simulation times by up to $4\times$. Figure 4.3 shows how the symmetric and anti-symmetry rules apply for the magnetic and electric field polarisations of the injection source for a 2-way symmetric system. The software is designed such that if

the polarisation type is symmetric with a plane of symmetry, the same-coloured symmetric boundary condition should be chosen. Here, this means that the magnetic polarisation is normal to all symmetric boundaries, and tangential to all anti-symmetric ones, with the electric polarisation behaving opposite to this. Finally, we have some additional boundary

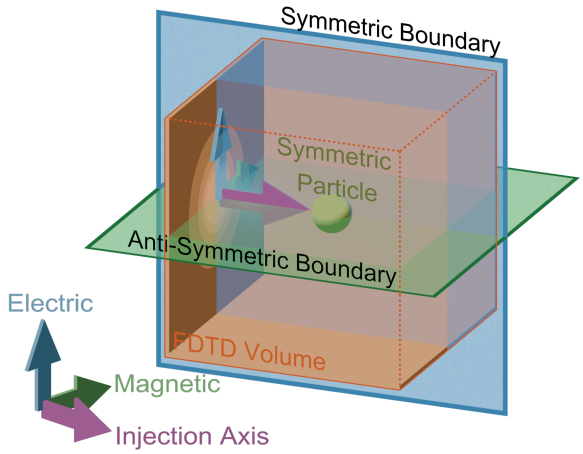

Figure 4.3: Symmetry conditions of magnetic and electric components relative to the injection axis of a light source in FDTD.

types that are important to know. For nearly all simulations, we use a perfectly matched layer (PML) boundary with the option to extend structures through it. Both the PML and other boundary types are illustrated in Figure 4.4, which shows how intersecting geometry from an example substrate with gold particles in trenches is handled under each condition. The PML boundary condition absorbs light without reflection across all incidence angles and frequencies in theory[115]. In software, it achieves this by the graded superposition of absorbing layers from a 'soft' inner, to a hard cut-off outer boundary. A limitation of PML is that reflections can still occur under certain conditions. We found that it was prone to cascading overflow if metallic inhomogeneous media was intersecting with the interface. When the 'extend structure through PML' option is enabled, absorption is computed using a stretched mesh extruded from the face-normal of intersecting geometry at the boundary. In both cases, the PML thickness should be at least half the wavelength of the lowest-frequency mode in the simulation.

Periodic boundary conditions do exactly what it says on the tin, they let you create large systems repeated from the contents of the FDTD volume. Electric fields incident at any periodic boundary will simply be copied to the next. This is useful for simulating large arrays of devices. If the incident light is propagated at an angle, then the Bloch boundary condition should be used.

In this work, I never had any use for perfect electric conductor (PEC) or perfect magnetic conductor boundary (PMC) conditions, since all our devices are simulated on a thick

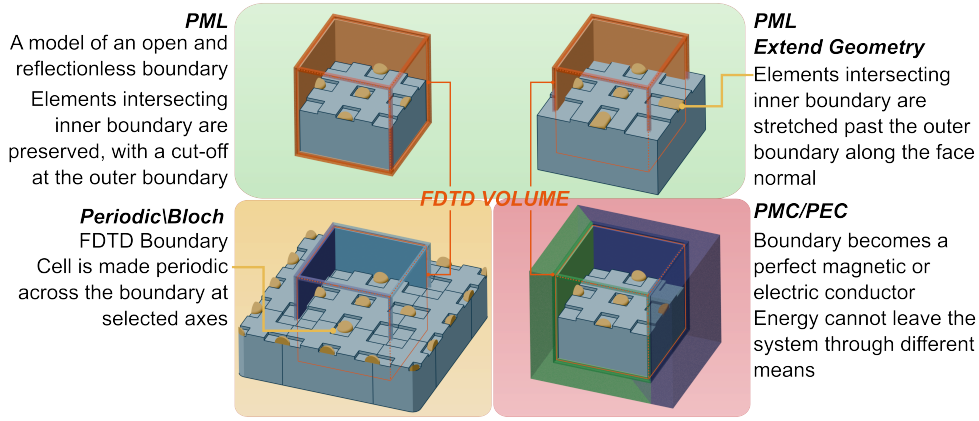

Figure 4.4: Examples of different boundary conditions available for use in FDTD when applied to a substrate with square trenches some of which are filled with hemispherical Au particles. All of these boundaries work together with the symmetric boundary rules shown in Figure 4.3, and each face of the FDTD volume can be independently set to any of these types.

layer of SiO_2, optionally with a planar waveguide. The PEC boundary condition acts like a perfect reflector, where parallel electric, and perpendicular magnetic components are zero at the boundary. Here, no energy ever escapes the simulation at boundaries set as PEC. PMC is similar, instead considering parallel magnetic, and perpendicular electric field components as zero at the boundary. A typical use case for PEC would be when modelling a patch antenna on a metallic substrate, since it more accurately replicates the expected electric field reflection.

4.3 Scattering and Absorption Cross-Sections

The cross-section of any element is highly dependent on its size in relation to the wavelength of incoming light. While a naïve estimate of any absorption cross-sectional area is to take a flattened projection of the object normal to any incident light, but for objects whose size is near the wavelength, this value will be inaccurate due to the effects of scattering. In our structural range (0.01 - 3 μm), there are two main types of scattering, namely Rayleigh and Mie scattering, both pictured in Figure 4.5. The analytical solution for the light scattering by uniform spherical particle in a fully homogeneous medium (including air) was first published by Gustav Mie[116], ergo the name, taking the form of an infinite series of spherical multipole partial waves. This is one of many solutions to the Maxwell's equations for dielectric particles. Nowadays, the scattering in question refers specifically to the near-wavelength range of particle interactions, which at the nanoscale is almost exclusively limited to the electric multipole series[117]. From the figure, the desirable feature of Mie scattering is in its ability, through the optimisation of scattering efficiency components, to control the directivity of light, allowing nanostructures to act as either light directing

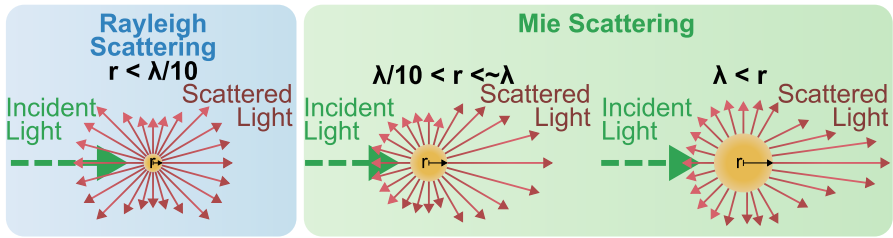

Figure 4.5: Illustrations of the different types of scattering based off spherical particles.

elements, or as antennas. In this thesis, we aimed to investigate the feasibility of utilising gold director elements that could be deposited in the same contact metallisation step as for any on-chip devices. While the analytic solution to Mie scattering applies only to spherical dielectric materials, Lumerical's FDTD suite numerically solves Maxwell's equations, enabling the extraction of scattering parameters for particles of arbitrary morphology. By combining this with a set of scattering and cross-section monitors, we can determine the forward scattering Mie efficiency—even for metallic particles, where the magnetic response is typically excluded[117].

In order to find the most optimal forward scattering nanostructure, we would normally need to calculate the scattering and absorption efficiencies Q_{sca}, and Q_{abs}. These are derived from the scattering and absorption cross-sections σ_{sca} and σ_{abs}, which are expressed as ratios of the normal incidence projected area of the particle, which for a sphere is

$$Q_{sca} = \frac{\sigma_{sca}}{\pi r^2} \qquad\qquad Q_{abs} = \frac{\sigma_{abs}}{\pi r^2}. \tag{4.4}$$

The sum of these give us the extinction efficiency Q_{ext}, which, together with Q_{sca}, can also be determined from the infinite series as defined by Gustav Mie[116]

$$Q_{sca} = \frac{2}{k^2 r^2} \sum_{n=1}^{\infty} (2n+1)(|a_n|^2 + |b_n|^2) \tag{4.5}$$

where r is the radius of the particle, k is the wave vector, and a_n and b_n are Mie coefficients of order n, where $n = 1$ is the dipole term, $n = 2$ the quadrupole, and so forth. Beyond this, the directionality becomes more significant when you want to design directing nanoantennas. The analytical solution beyond this can then distinguish from forward and reverse scattering using what is known as Kerker effects[118], and are given by

$$Q_{sca,bwd} \propto \left| \sum_{n=1}^{\infty} (2n+1)(-1)^n (b_n - a_n)^2 \right. \tag{4.6}$$

$$Q_{sca,fwd} \propto \left| \sum_{n=1}^{\infty} (2n+1)(a_n + b_n) \right|^2 \tag{4.7}$$

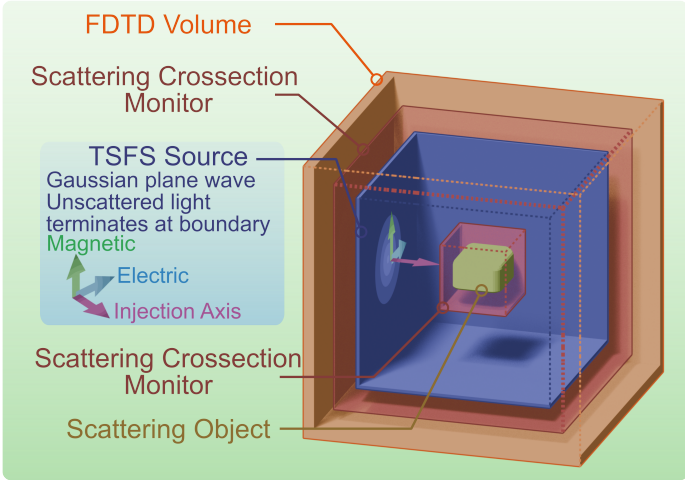

Figure 4.6: FDTD, monitor and source setup to determine the scattering and absorption cross-sections of a nanoscale structure.

We, however, have the use of an FDTD solver, where we can set up a simulation to calculate the Mie efficiency, polar plots of directionality, and the ratio of forward and backwards scattered light. The way this is done can be seen illustrated in Figure 4.6. Here, we make use of an artificial plane wave known as a Total-Field Scattered-Field (TSFS) source. It separates the total field region, representing the sum of both the incident and scattered field, from the scattered field, which only includes the scattered field. Put simply, only scattered light can leave the enclosed volume of the TSFS box, represented by the blue box in the Figure. This means that the TSFS enclosed scattering cross-section monitor, when compared to the external scattering cross-section monitor, can be used together to determine both absorption and scattering cross sections, which is sufficient data required to calculate the Mie scattering efficiency described prior with a built-in mie3d function. With the Mie scattering efficiency, we only need to determine the ratio of forward and reverse scattering, which can be done using the external scattering cross-section monitor, which is built up from several 2D transmission boxes that measure transmitted power.

In a direct application, we can iterate on the enclosed particle's dimensions, measuring the total transmission of the forward-scattered field to identify the scattering element best suited for forward-scattering applications. This, in turn, can be incorporated into fabricated optical structures. An additional benefit of this setup is that it also enables a for the determination of single NW device cross-sections, allowing for more accurate estimates of external quantum efficiency.

4.3.1 Iterative Testing of Optical System Performance

Lumerical's FDTD suite comes with a wide range of options for automation. Any variable defined in the software can be added to a parameter sweeps, saving only the monitor or analysis group data desired at the end of each run. This system effectively enables rapid parameter optimisation, where tests can be run to find e.g. the ideal waveguide thicknesses for power absorption in a distant element, or the optimal forward scattering cross-section of an antenna. However, unless you are the sole user of a PC running this software, larger scale simulation projects that require week-long non-stop simulations are suboptimal. For one, saved monitor data accumulates in the file for each run, which can quickly lead to the PC becoming RAM-limited, rather than storage-limited. Another reason is software volatility, where hard crashes or power-cuts during simulations or the save procedure could corrupt the working file, resulting in the complete loss of simulated data. In the parameter sweep settings, while there is an option to resave the file after every sweep, we had several occasions where extraneous factors would cause an abrupt end to a long parameter sweep, so I instead had to seek alternatives. While this section is not a dedicated soliloquy for limitations the software itself brings, I want to highlight some pressing limitations. This section will only be covered in brief, with remainder information about workarounds and

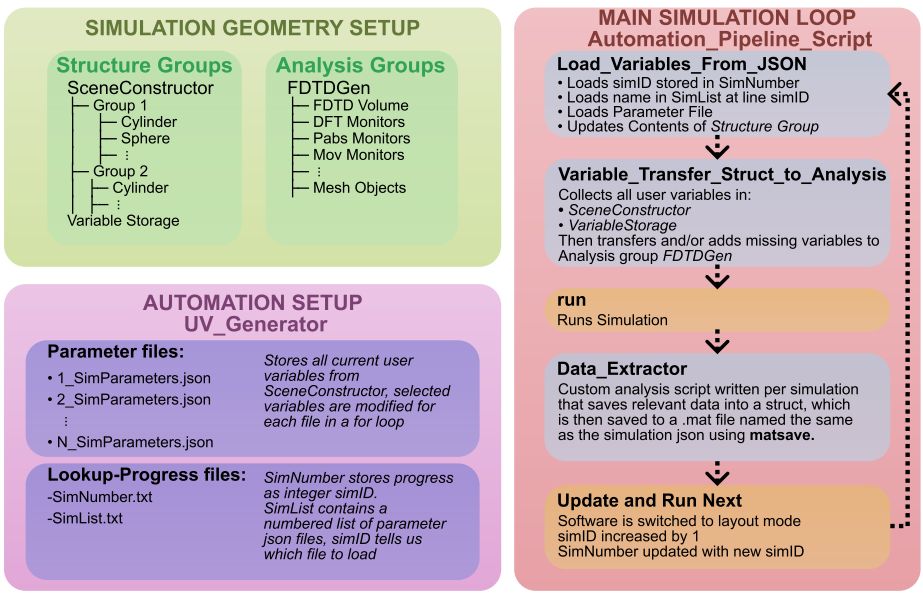

Figure 4.7: Flowchart showing how automated simulations are set up. Code within Analysis and Structure groups are written on a per-simulation basis, defining the geometry of the simulation. UV_Generator script writes out complete parameter sets to numbered .json files, where each file has one parameter iterated on in a defined range. Automation_Pipeline_Script then sequentially loads user variables stored in json files, runs the simulation, saves data, then moves on to the next file.

script implementation provided in the readme file of my self-authored Github repositories [119], with assisting functions for analysis in [120].

In Lumerical, analysis and structure groups double as script containers and as object groups, storing multiple types of monitors or objects in the same location. I opted to write code in these groups to define all simulation objects using the built-in scripting system. A major limitation is that these systems cannot communicate, meaning that if the volume that defined objects occupy is reduced, the FDTD region cannot be re-calculated with this information directly, but rather has to be estimated separately, resulting in longer simulation time. I wrote a script that collects all user variables for any number of structure groups, transferring them to the analysis group. With this, I can e.g. automatically move power absorption monitors based on the structure group NW position.

With this framework, automation is done by a dictionary generator saving variables to a text file, which can then be read sequentially for each new simulation. So with this framework in place, to run sequential multi-parameter sweep simulations that resist problems related to hard crashes, file corruption, and RAM limitations, enabling post-processing in Python for data analysis.

This way, we save only monitor data after the completion of each simulation, preventing loss of data resulting from crashes, and allows other users to use the PC without needing to wait for the entire set to complete. I developed this approach out of necessity from when our simulation PC only had 32 GB of RAM, which would quickly be exceeded during parameter sweeps. The current system has 384 GB of ram, but I still prefer the level of control offered from this, especially now that tools have been developed in python to process this data[120].

CHAPTER 5

Optically Communicating On-Chip Nanowire Devices

'Nothing travels faster than the speed of light with the possible exception of bad news, which obeys its own special laws.'
—Douglas Adams, Mostly Harmless

This thesis is an exploratory work that aims to build a foundation for achieving multi-component nanoscale optical broadcasting for on-chip applications. To demonstrate the feasibility of such a system, the most basic building block, consisting of an emitter and a receiver, must first be fabricated, and its functionality characterised. Inspired by the pilot study in [33], whose inception led to the creation of the InsectNeuroNano Project[43], we determined that emitter and receiver elements should come in the form of single III-V p-n and p-i-n junction NWs, whose growth has been optimised for either light emission or absorption. The development of this emitter-receiver device did not only have to demonstrate that optical communication between nanoscaled components is possible, but it had to be done to such effect that the assembly of a larger system is demonstrably possible. This means solving device assembly, such that the individual manipulation and placement of NWs results in the intended configuration on a substrate within acceptable error. It means finding a high yield metallisation methodology to improve ohmic contact creation to both p- and n-type segments, and confirming the effect that deposition of waveguide materials has on both IV characteristics and optical coupling.

In this work, we have developed a process for the assembly of individual III-V NWs into optically communicating device pairs. While inclined to avoid using descriptors such as novel and groundbreaking, the demonstration of direct optical communication between two nanoscaled emitter-receiver NW components on a chip has not, to our knowledge, been done before our published work in Paper I. As such, in this chapter I will discuss the complete device fabrication process development, the individual and paired NW characterisation, and the supporting FDTD simulations that show in-air and waveguided limitations of distance separation, culminating at our current stage of development. Furthermore, I will detail how each of the other encompassing work has built towards realising the components necessary for the Stone model, described in the introduction and in [40]. From

using the photochromic dyes as a memory medium to regulate signal strength between communicating NWs in paper IV, to how this can be achieved with on-chip elements.

5.1 Development of Reliable Nanowire Device Assembly

As an introduction to this section, I refer to the conceptualisation of the most fundamental device shown in Figure 5.1, which repurposes two p-i-n junction NWs, originally grown as solar cells, as an emitter-receiver pair. With pre-grown InP NW arrays with proven effect in solar cell applications[77], we already had a solid foundation for its photocurrent generating properties, and while p-i-n junctions are not considered ideal for LED applications, a sufficient forward bias should still result in a significant charge recombination over the intrinsic region. From here on out, first comes the question of placement. While the random transfer of a large number of NWs to a substrate can be considered trivial for the purposes of single transverse NW devices, as we will discuss later, producing NW pairs with small rotational variation, and high separation accuracy is not. And, while technically not a problem if one was hoping for a 'hero' device pair, the aim of fabrication methodology development was to reach the point where it can be considered sufficiently scalable for larger assembled structures of up to tens, or even a hundred NWs. Secondly, without an epitaxial contact to what was originally a p-type growth substrate, finding an appropriate native oxide removal technique together with a metallisation stack that produces a reliable metal-semiconductor contact is essential. If individual device pair yields are too low, then realising a larger network more akin to the one in [33] becomes statistically improbable. As

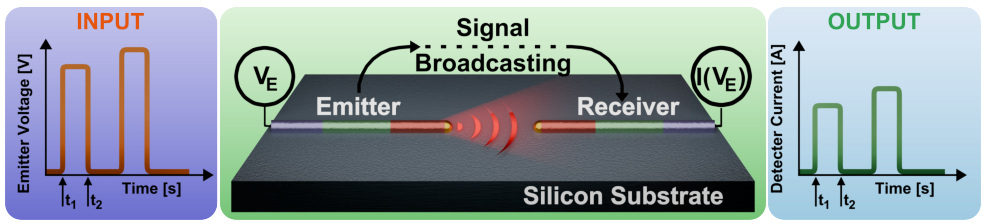

Figure 5.1: The fundamental 2NW device concept, where the emitter input is reflected in the current output of the receiver NW.

such, before we could even begin, we had to figure out how best to consistently produce device pairs with reasonable separation.

5.1.1 Multi-NW Device Assembly And Fabrication Pipeline

Sometimes, it is best to start from the end and work your way backwards. Figure 5.2 shows an illustration of the essential steps of the fabrication pipeline that we settled on for the creation of optically communicating NW device architectures, detailing only steps 8-16 from the stepwise methodological summary in Table 5.1. Working from the 5×5

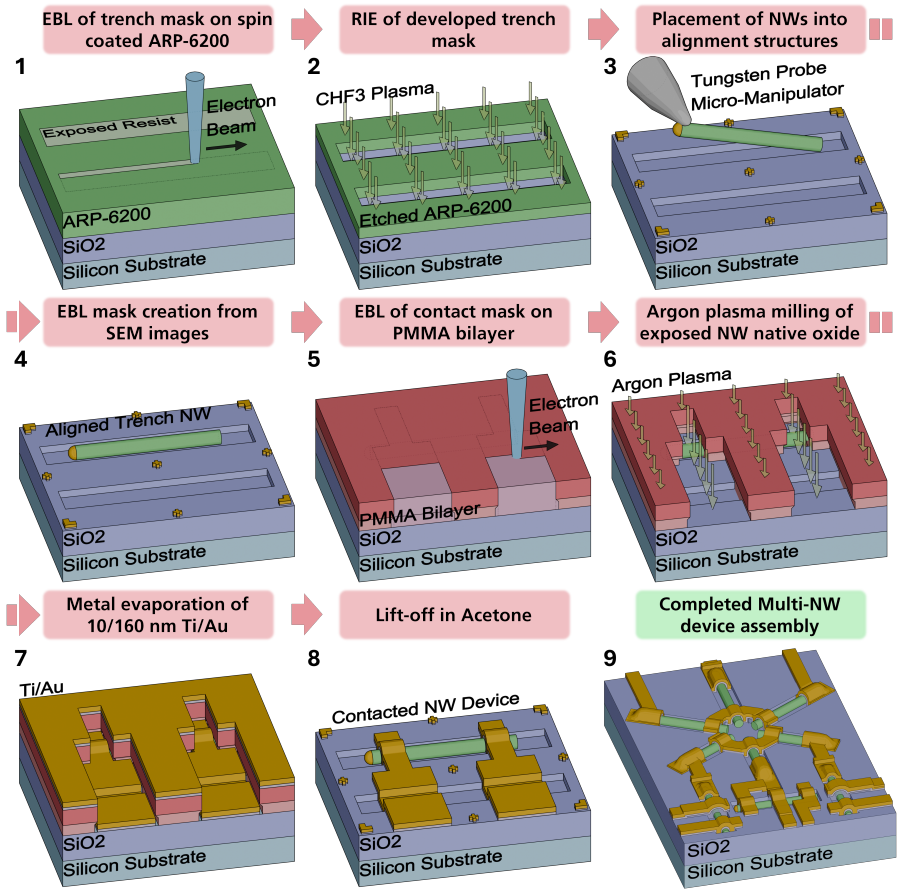

Figure 5.2: The final fabrication pipeline used for the multi-NW assembly of optically communicating optoelectronic devices. Reproduced from same source file used in Paper II

device chip outlined in Chapter 3, we design a NW device template, the mask of which is exposed onto the etch resistant ARP-6200 E-beam resist, and transferred to the SiO_2 using RIE. This results in ∼150 nm deep trenches whose purpose is to simplify NW deposition when using a micro-manipulator setup, controlling for rotational alignment, and with some designs limiting minimum separations. SEM images taken after alignment can then be used for the contact design, allowing for complex multi-NW device assemblies to be put together rapidly. It may sound simple now, but the journey to get here was a long and winding road, the major pitfalls and strides of which I will now go over. For the sake of reproducible documentation, a step-by-step guide detailing each individual step in the table can be found in Appendix A.

Table 5.1: Stepwise summary of the fabrication pipeline used to process the pre-patterned wafer, for the assembly and contacting of multi-NW devices, in addition to the methods used for the deposition and contact-etching for ALD based waveguides.

Step	Task	Description	Tool
Full Wafer Processing			
1	Lithography #1	Pattern large contact pads on the full wafer	Optical Lithography, Mask-Less Aligner (MLA150)
2	Metallisation	Ti/Au Deposition	Evaporation (Temescal E-Beam)
3	Lift-off	Removal of resist & metal from unpatterned regions	Wet Bench
4	Lithography #2	Pattern alignment marks on full wafer	EBL (Raith Voyager)
5	Metallisation	Ti/Au Deposition	Evaporation (Temescal E-Beam)
6	Lift-off	Removal of resist & metal from unpatterned regions	Wet Bench
7	Dicing	Full wafer cut into usable chips	Wafer Dicer (Disco DAD 3320)
Diced Sample Processing			
8	Lithography #3	Pattern trenches required for NW alignment	EBL (Raith Voyager)
9	Etch	SiO2 etch of patterned region using CHF_3	Reactive Ion Etch (Trion T2)
10	Resist Removal	Removal of resist from unpatterned regions	Wet Bench
11	NW Deposition	Transfer NWs onto trenches on substrate	Benchtop Micromanipulator with Optical Microscope
12	Imaging	Capture SEM images to ascertain position of NWs	SEM (Leo 1560/GeminiSem500/FEI Nova Nanolab 600)
13	Lithography #4	Pattern contacts between NWs and large pads	EBL (Raith Voyager)
14	Etch	Native Oxide Removal	Ar Ion Milling (Temescal)
15	Metallisation	Ti/Au Deposition	Evaporation (Temescal E-Beam)
16	Lift-off	Removal of resist & metal from unpatterned regions	Wet Bench
17	Annealing	Thermal processing of metal-NW contacts	Rapid Thermal Processing (RTP 1200-100)
Blanket Waveguiding for Signal Improvement			
18	Oxide Growth	Al2O3 waveguide growth at 200 °C	ALD (Savannah-100)
19	Thickness Measurement	Ellipsometry measurement of Al2O3 layer thickness for determination of etch time	Ellipsometer (RC2)
20	Lithography #5	Re-pattern over large contact pads	Optical Lithography, Mask-less Aligner (MLA150)
21	Wet Chemical Etching	Develop resist, and use aluminium etchant A to expose large scale contact pads	Wet Bench

5.1.2 NW Assembly Techniques Overview

There are many different methodologies for the large and small scale assembly of multi-NW devices. Much research has already been done on the properties of grown NW arrays where the assembly beyond Au seed patterning, and top-contact definition is not required. For single NW contacting in grown arrays, the challenge lies more in achieving good focus and alignment to the electron transparent BCB[121]. Therefore, the prospect of multi-NW assembly for complex optical network remains a relatively unexplored field, meaning that the exploratory work to realise reliable fabrication is much more significant.

We categorised the NW assembly techniques into three main categories. 1) Direct NW synthesis at pre-determined locations, 2) Large scale alignment from an external directional force, and 3) manual transfer and placement, either mechanically or with manipulator and probe tools. For direct synthesis, this includes all variations of selective area growth (SAG) beyond simple Au seed definitions from EBL. For instance, hard masking and etching can ether expose different crystal plane orientations for direct lateral growth from an Au seed[122], or it can be the channel used to constrain growth[123]. The downside of this is that heterostructure formation along laterally grown NWs becomes a further challenge due to the strain induced by the lattice.

Large scale assembly techniques are usually reliant on NW suspensions. Alignment here occurs either from the directional displacement caused by the fluid itself, be it from bubble blown techniques[124, 125], Langmuir-Blodgett assembly[126–128], channel-flow shear force[129, 130], or simply the capillary effect into surface grooves or polymer channels[131]. For further control, these can be combined with electric-field-assisted[132–135] or dielectrophoretic methods[131, 136], or even electrospinning[137]. While all of these techniques could be applied in one way or another for the production of individual NW pairs for optical communication, if considering a minimum working device whose function relies on interconnectivity between several different species of NWs purposed for different functions in the system, then none of them have the flexibility and precision required for their precise assembly. This is why elected to limit ourselves to manual techniques, which instead rely on advanced micro-manipulator systems that can pick up individual NWs and place them down in a desirable position with reasonable accuracy[138]. Combine these with oxide-etched device template guidance structures, as we will get onto in the later sections, and you will come to see how this approach is potentially scalable to larger systems, where any number of different NW species can be integrated into a shared purpose. The following sections will detail how we evolved our approach, before culminating in a description of the flexible fabrication described in Paper II.

5.1.3 Omniprobe Assembly

The most common manual deposition method is through the use of a cut corner from a piece of cleanroom tissue, where transfer is done by dabbing it a few times into the growth substrate, and then a few times on your target substrate. If you are lucky, a reasonable

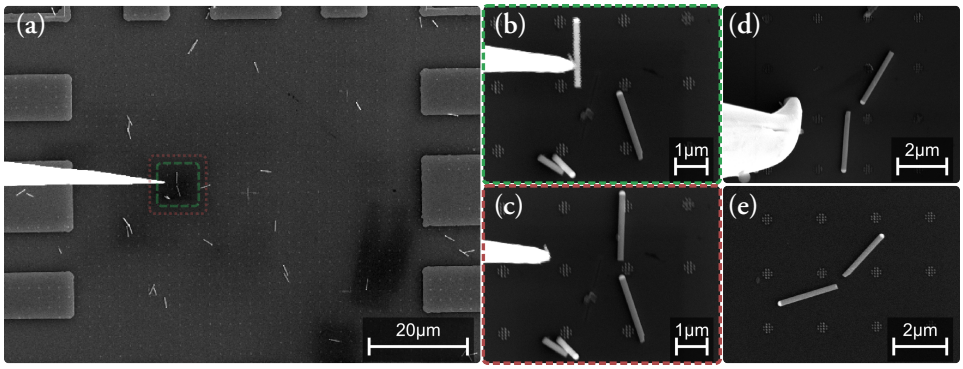

Figure 5.3: Omniprobe free-hand placement of NW pairs. (a) Writefield overview of mechanically deposited NWs on first generation flower pattern with a single highlighted NW pair aligned with the visible probe. (b) NW held by tungsten probe before deposition. (c) NW post-deposition. (d) and (e) show two additional aligned NW pairs from a different writefield. Note that panels (a)-(c) show extensive substrate beam damage, and panel (d) a damaged tungsten probe.

amount of NWs have been transferred, but often your writefield ends up either empty or fully saturated. In my initial venture into micro-manipulation for NW alignment, this is the initial step performed before loading the sample into a SEM equipped with a remote controlled tungsten probe manipulator known as the omniprobe. More commonly used for lamella transfer[139, 140], I was inspired by its use to create single NW devices for use in Optical-Beam-Induced-Current scanning[141]. Here, any of the roughly deposited NWs can be picked up by the probe, and moved to align it with another. In Figure 5.3, we see several examples of NWs aligned using this method. This method is limited by far too many factors to ultimately be useful in the pursuit of reliable multi NW assembly. For one, while

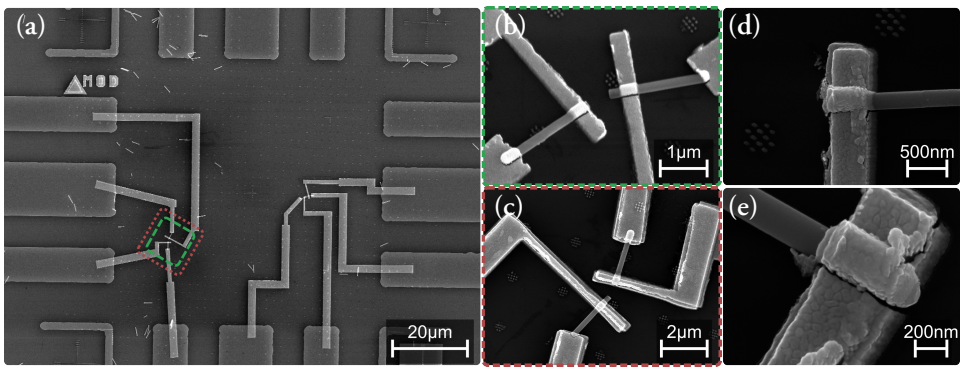

Figure 5.4: Final contact metallisation over omniprobe aligned NW device pairs. (a) Writefield region with two contacted devices. (b) Non-rotation deposition of 10/150 Ti/Au of device labelled in (a) that resulted in discontinuous contacts. (c) Repeated non-rotation evaporation of another 10/150 nm Ti/Au with same EBL mask. (d) Close-up of a different repeat-evaporation, continuous only for a small proportion. (e) Close-up of different, possibly discontinuous, repeat evaporation contact. (d) and (e) are from a different writefield on the same chip as (a).

this tool sees great success in combination with FIB milling to extract substrate lamellas, precisely navigating the probe tip to the midpoint of a NWs whose diameter is 166 nm is not trivial for a variety of reasons. The shallow depth of field makes it difficult to identify when the tip is co-planar with the NW. Furthermore, the fact that the tip make contact with the substrate during z-movement, any bending of the tip is not immediately evident due to the view angle. This difficulty is further compounded by the latency of both the probe controller and the imaging in combination with the unreliable probe motor control whose speed, time to stop, drift, and fine control would vary so significantly, that crashing the probe was not a matter of if, but when in nearly all sessions, as can be clearly seen in Figure 5.3 (d). This led to the alignment of a single pair taking upward of an hour, resulting in significant beam damage and carbon contamination to both NWs that needed to be observed by the SEM for this duration. Ultimately, this leads to worsened metal-semiconductor interfaces, and a lowered electrical conductivity from a reduced dopant contrast[142, 143].

Regardless, I still produced several devices through this method, some of which are shown in Figure 5.4. Metallisation with this technique was initially done using the AVAC evaporation system with a target thickness of 10/160 nm Ti/Au. However, the 88 nm radius of these NWs ended up shadowing the substrate from top-down evaporation to such a degree that both finger and wide-base contacts ended up discontinuous, resulting in no electrical contact between bondpad and NW, as can be seen in panel (b). Panels (d) and (e) even showcase an example where I repeated the EBL masking, development and evaporation steps, and even with double the thickness, substrate and NW evaporated metal only barely connect. All these factors together required a complete rethink of the assembly technique, both for the accuracy and speed of deposition.

5.1.4 Molten Indium Probe Micromanipulator Assembly

With the aforementioned issues with Omniprobe based assembly, I instead looked towards tools operated with standard optics. For this, we envisioned using a micro-manipulator setup where a coarse tungsten probe is inserted at normal incidence into molten indium (In), after which the speed of its extraction controls the formation and termination of a fine In tip. With this In tip, we can somewhat control the area of deposition by direct transfer of NWs from growth substrate to a device region, where the bundle of NWs collected on the tip can be brushed off by direct contact to the substrate. With single NW devices, this approach is more than suitable, but since we need to control for separation and rotation of NW pairs, without the potential precision of the Omniprobe, we would instead need physical structures patterned on the substrate surface to guide NW deposition into target areas. For this, I tested combining EBL and reactive ion etching, as detailed in steps 8-10 in Table 5.1, to define trench structures in each device region. We found that if the probe was brushed along the trench length, not only would NWs tend to orient themselves along the axis of movement, but the additional surface area of the trench walls would exhibit greater van der Waals forces than the substrate surface[144], tending to leave NWs more commonly

deposited within these structures. The mechanics of this process is further discussed in Paper II.

Figure 5.5 shows examples of the various initial approaches to deposition using this

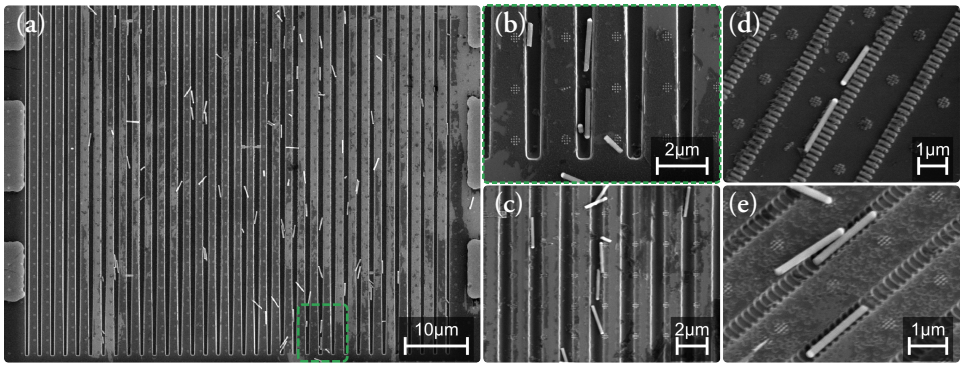

Figure 5.5: Initial deposition using molten indium probe micro manipulator. (a) Writefield overview showing general spread of NW orientations and frequency of alignment within trench. (b) Close-up of highlighted NW pair shown in (a). (c) Additional example of in-NW alignment from the same sample. (d) Example of alignment to intentionally cross-linked resist walls, showing that additional alignment features can be used. (e) Alignment of NW into shallow trench.

method. For the random creation of NW pairs placed within a few µm of each other, this technique is more than applicable, and is how we got our first optically communicating device. However, the lack of control means that reproducible separations for comparisons between devices is impossible. Furthermore, the variable size of the probe means that the accuracy of NW deposition varies between attempts, in addition to mechanical transfer yielding NWs with damaged stems, and other fragments all of which can be in nearly all panels of the figure.

5.1.5 Robot-Assisted Tungsten Probe Micromanipulator

In the end, we settled on a solution together with collaborators[1], wherein we provided pre-patterned samples and grown NWs, and they utilised a robot-assisted fine tungsten probe micro-manipulator system to perform the final deposition step. The control offered by this setup allowed single NWs to be precisely placed into the trench structures, after which their location within can be altered by soft force applied along the trench at either end of the NW. Figure 5.6 showcases several different NW alignment geometries, all achievable in this schema. It is this that has consequently allowed us to explore the idea of creating a minimum working device, whose assembly requires upward of 42 NWs. The general flexibility and precision being clearly visible throughout the many examples presented in the figure.

[1]Joachim Elbeshausen Sestoft and Jesper Nygård, Niels Bohr Institute

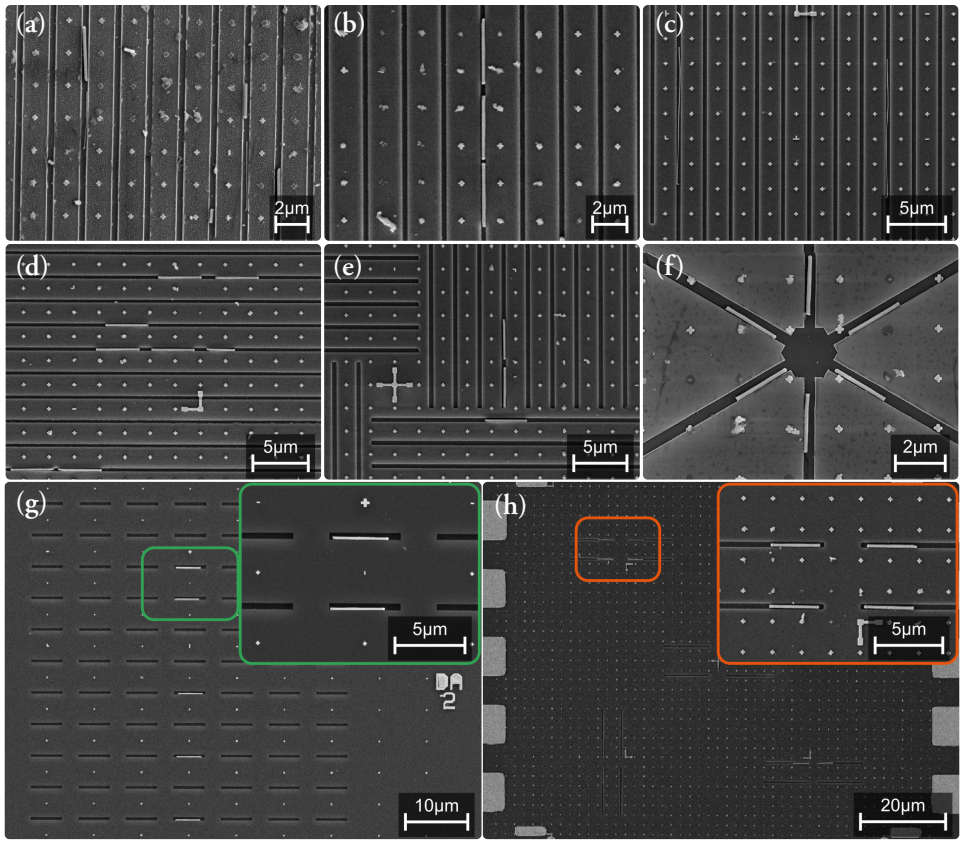

Figure 5.6: SEM images of alignment variation achieved with the robot-assisted microprobe system. (a) Example combination of molten indium probe, used for rough initial placement of InP, with InGaP NWs precisely matched using robot micromanipulator. (b) Linear close-proximity alignment of InP NWs in the same trench length. (c) Long InAs NWs aligned in trenches. (d) Linear close-proximity alignment of several NWs in different trenches. (e) Parallel aligned NW pair in the same vertical trench, with a centred horizontally aligned NW underneath. (f) InP NWs aligned near-equidistant in a hexagonal trench pattern[1]. (g) Slotted horizontal NWs placed in the same column with miniscule variation[2]. (h) Slotted horizontal pairs of NWs, demonstrating ability to adjust position along length of trench[3].

5.1.6 Final Contact Metallisation

Finally, with EBL, metallisation, lift-off and annealing outlined in steps 12-17 from Table 5.1, we arrive to our final non-waveguided devices, of which several are shown in Figure 5.7. Most of these panels showcase the same examples as illustrated in Figure 5.6. With the exception of panel (a), all devices are assembled only using the robot-assisted micro manipulator setup. While we will not go deep into specifics here, in the development

[1]Image Credit: Joachim Elbeshausen Sestoft

[2]Image Credit: Leon Seggering, Hamburg University & DESY. Device fabrication in project collaboration for *Integration of Light Sensitive Nanowires Within Nanoimprinted Fluidic Devices*(working title).

[3]Image credit: Abhijit Das

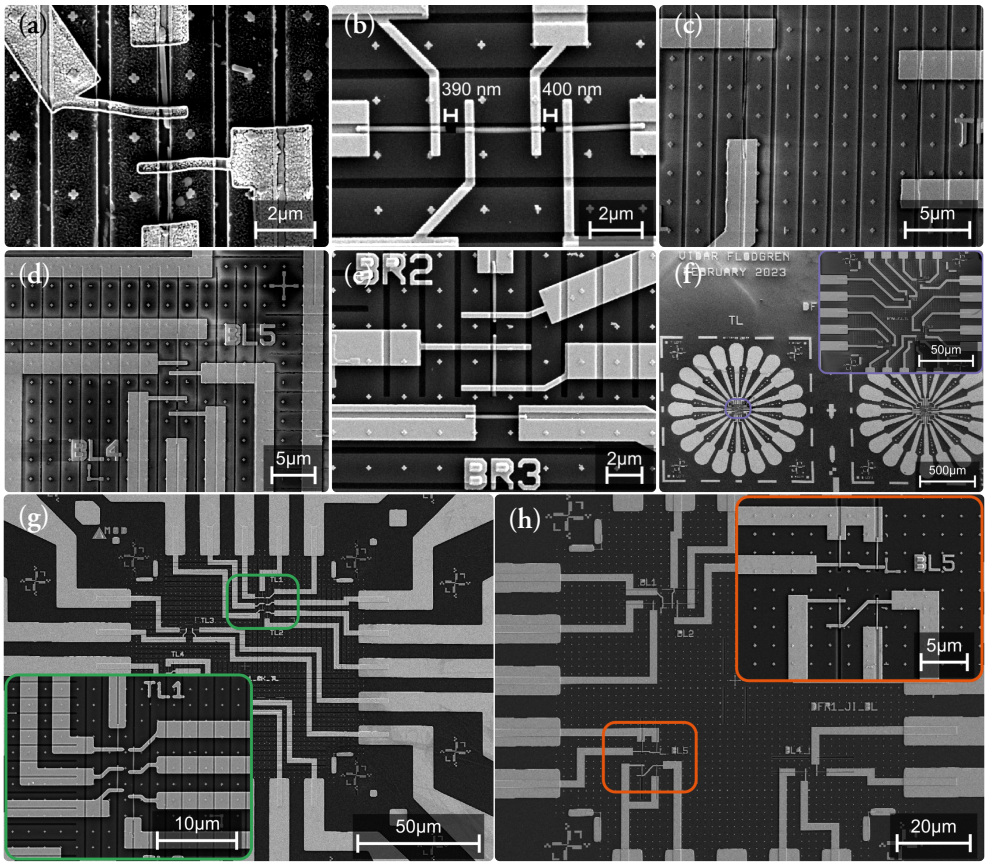

Figure 5.7: SEM images of varying types devices after contact metallisation, of which panels (a), (b), (c), (e), (g) have their deposition step also shown in Figure 5.6. (d) Shows a contacted multie NW device aligned within 200 nm wide trenches, demonstrating the placement flexibility for different width trenches. (f) A single flower pattern with an insert showing the device leads defined within.

of this fabrication pipeline we iterated through a vast number of variables before ending up at this flexible fabrication assembly of NWs. As should be evident from Figure 5.4, initial device yield was assumed poor as a consequence of the evaporation angle used in the AVAC resulting in poor surface coverage and shadowing. A solution for this was simply using a holder that was capable of tilt and rotation, which would reduce shadowing enough for continuous coverage with as little as 10/100 nm Au. From steps 14-15 in the listed fabrication pipeline from Table 5.1, and as detailed in Section 3, it should be noted that tilt and rotation is not possible with holder D, but it was with the native oxide removal technique that was used for the first optically communicating devices. Instead, at this point, we were also using with a mixture of 1:10 H_2SO_4:H_2O as a native oxide removal and passivation agent[145–148], before evaporation. Furthermore, the metallisation stack for this first sample also had an additional evaporation step of 5/10 nm Ti/Zn[149–153]

in the AVAC before the main 10/160 nm Ti/Au was evaporated with rotation and tilt in the Temescal followed by annealing. We suspected that, in spite of the claimed passivating effect, with the sample requiring an N2 drying step followed by a transfer into the Temescal vacuum chamber, the time it spends exposed air before this was sufficient for some native oxide re-growth. As such, it is important to highlight that while we were able to optimise the native oxide removal with argon plasma milling done directly in the same vacuum chamber as evaporation, the wet chemical etch process also has the potential to be optimised similarly. And while the loss of rotation on the holder requires thicker evaporation stacks, the addition of trench structures also reduces the step coverage needed. More discussion around this can be found in Paper II.

In terms of NW assembly, from the hour per pair using the omniprobe, to an hour in the molten indium probe setup to sufficiently over-populate the trench structures for a handful of NW pairs, to accurately aligning 20+ NWs in an hour of manipulation using the robot-assisted setup, a $\times 20$ time improvement of assembly, in addition to improvements to the general yield, has brought the idea of multi-NW assembly into a complex artificial optical broadcasting neural network from dream to a feasible reality.

5.2 Device Characterisation

Complete device characterisation is always a lengthy procedure, especially if future device data is to be comparable with the first generation of measurements. As a consequence, we set up a standardised measurement system, one that we still maintain for future papers, and accompanying this several systems of automation to simplify device comparison. Most of our measurements are done on a Cascade 11000B probe station with a Keithley 4200A-SCS parameter analyser. In our measurements, we often made use of all four probes, contacted to the sample as pictured in Figure 5.8 (a), forming the circuit found in (b). It is with this

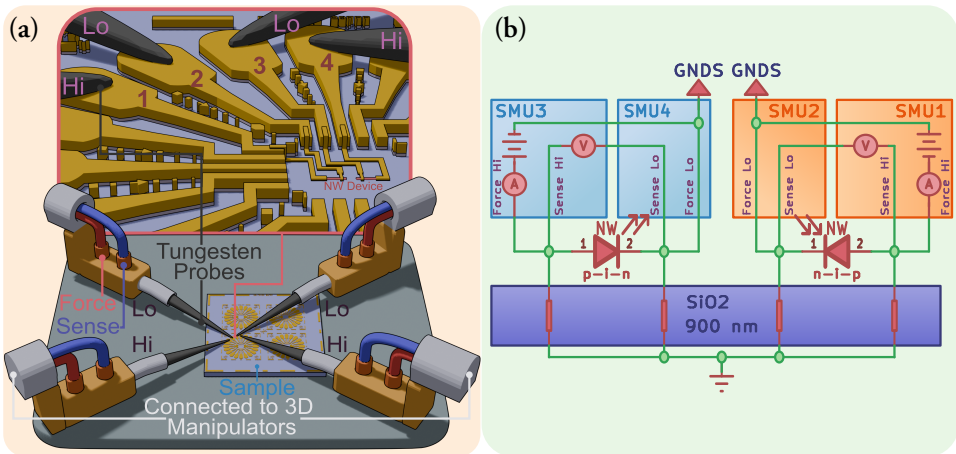

Figure 5.8: (a) Labelled illustration of how a NW device pair is contacted in the probe station. (b) Circuit diagram formed by the Cascade 1000B through the source measure units (SMUs) when probes are connected according to the corresponding labels in (a). Each probe can independently be set to ground for IV measurements on individual NWs before collective characterisation. A final connection between the substrate back and the 3D stage is also made, which can optionally be biased as a back gate, which is set to the chassis ground as indicated by circuit termination underneath the oxide. This renders devices floating.

that we follow a strict set of measurement procedures, as outlined in Table 5.2, designed to ascertain that results for any future devices will be comparable. During measurements, a spreadsheet sharing part of the same name as the measurement data is maintained, containing information about which segment of each NW is connected to what SMU, which runID's were saved, the type of measurement and on which NW and side it was done. The way we have stored this data allows us to crawl the folder structure, and automatically collect results from devices sharing the same name, and from subdevices, and their measurement variations. It is this that has allowed us to manage the thousands of different measurements required for a complete and comparable device characterisation and comparison.

Table 5.2: Stepwise summary for the each measurement step involved in NW characterisation using the Cascade 11000B probe station shown in Figure 5.8. All NW device pair bondpads are contacted with the probes even during single NW measurements, where relevant SMUs are set to ground. Convention is for biasing to be done on the NW contact furthest away from the device centre, resulting in finger gates being set to a common ground for all measurements.

Measurement	Description
Single NW Characterisation	
1: NW "Curing"	Initial power cycling of each NW, involving high voltage sweeps in range [-7,7] V until IV curve becomes more characteristic. Script called Generate_CuringSweep can be used to create a cycling voltage list $[V_{min,i}, V_{max,i}]$ which decays by ΔV until reaching $[V_{min,f}, V_{max,f}]$. If either NW in a device pair appears shorted or broken, we do step 2 only for any working NW, and then move on to the next device pair. Tool settings: range 10 μA, compliance 1.1 μA, voltage step 0.1 V, speed "quiet", sweep delay: 0 s, hold time: 0 s
2: Standard IV	IV characterisation with standardised voltage ranges for the purpose of determining diode ideality. With forward bias assumed to be positive voltage: a) Measure IV with voltage range [-0.6,2] V, and voltage step 0.025 V. b) Measure IV with voltage range [0,1.25] V, and voltage step 0.01 V. Tool settings: range auto, compliance 1.1 μA, speed "quiet", sweep delay 0 s, hold time 0 s.
3: Illuminated and Dark Photocurrent	Reverse bias sweep under illuminated and dark conditions to verify photocurrent. Lowest range that keeps maximum current under compliance is used. NW in device pair with greatest photocurrent delta is chosen as receiver, and the other as emitter. Tool settings: range and compliance [10 pA and 1.05e-11 A] or [100 pA and 1.05e-10 A] or [1 nA and 1.05e-09 A], voltage step 0.05 V, voltage limits [0,4] in reverse bias, speed "normal", sweep delay 0 s, hold time 0 s.
Optical Communication Measurements	
4: Forward Reverse Emitter Pulse at Constant Receiver Reverse Bias	First optical communication test, where emitter and receiver IV is recorded when a created voltage list is cycled through [0,V_F,0,$-V_F$], where $V_F = I(V_F) = 0.7$ μA, on the emitter while the receiver NW is biased at a constant $V_R = 2$ V. For one cycle, each point is measured five times, and each complete measurement covers five cycles. Reverse bias component evaluates if significant leakage exists. Measurement is aborted if communication is not evident, and we move on to next device pair. Emitter settings: range 10 μA, compliance 1.1 μA. Receiver settings: same range and compliance as in step 3 Tool settings: speed "quiet", sweep delay 2.5 s, hold time 2.5 s
5: Emitter Sweep, Receiver Reverse Bias Step	Emitter and receiver IV is recorded when emitter NW is swept in the range [0,V_f] V (determined in step 2) with a voltage step of 0.025 V, repeated for applied receiver reverse biases in [0,1,2,3] V. Emitter and Receiver Settings: Same as in step 4. Tool settings: speed "quiet", sweep delay 2.5 s, hold time 2.5 s
6: Forward Emitter Voltage Ladder Pulse at Constant Receiver Reverse Bias	Final optical communication measurement, where the aim is to get 8 distinct receiver current levels whose amplitude could feasibly be discretised as weights. Emitter bias range $[V_{E,min}, V_{E,max}]$ should be selected so that $I_{E,max} = 0.7$ μA, and $I_{E,min}$ results in the minimum possible I_D that can be measured by the system. Example emitter voltage steps looks like [0.0, 3.2, 3.4, 3.6, 3.8, 3.9, 4.0, 4.1] V, where the voltage list created is mirrored around the maxima, with 0 V points placed between each step. Emitter and receiver IV is recorded five times for each point on the voltage ladder, with a reverse bias of 2 V applied on the receiver NW. Emitter and Receiver Settings: Same as step 4. Tool settings: speed "quiet", sweep delay 2.5 s, hold time 2.5 s

5.2.1 Single NW Ideality Determination

As outlined in Section 2, the ideality factor gives some quantitative measure on the overall quality of both the metal-semiconductor interface and the recombination in the p-i-n junction itself[15, 61]. As such, determining this factor is an important part of device characterisation, as it gives a metric of emitter and receiver performance[15]. Lower standard deviations also show the consistency and reproducibility of fabrication. Together, they give an outlook on the performance and yield of the measured batch of devices.

Through the extensive development of the data importing, plotting, and analysis tools in my own python package DMU[120], I was able to automate much of the data plotting and analysis. I first wrote a multi-purpose script file that wrapped the package functions to automatically scrub and categorise all measurement and logbook information per subdevice when executed from the same folder as this data. Its function was to rapidly produce the correct style plots with annotations of device-subdevice names, runID, and what each NW was operating as. However, when it came down to identifying good measurements to fit ideality on, and comparing outcomes from multiple measurements on the same NW, we ran into an issue. As we came to understand rather quickly, attempting to write a catch-all function to automatically fit and compare ideality is not feasible due to the sensitivity of

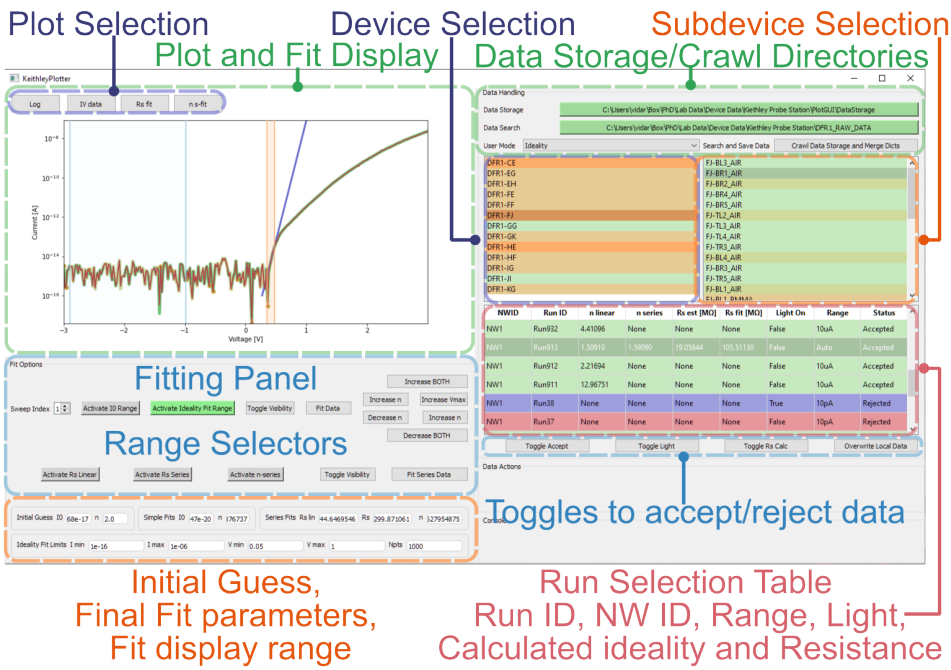

Figure 5.9: Annoted image of the DMIdeal_GUI[120] user interface. The plot display shows: a green IV curve of a single NW, a blue fit of the standard Shockley ideal diode equation[59], a red analytical fit for the current which includes the series resistance. Buttons activate fit range selection and fitting, where data can be chosen from the device, subdevice and run lists on the right.

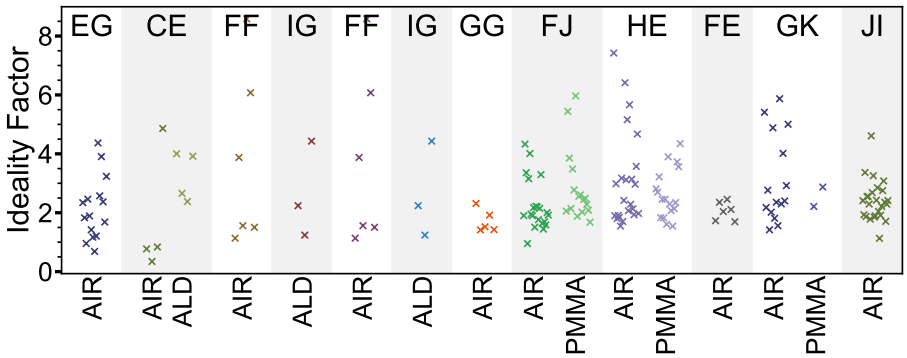

Figure 5.10: Best fitted ideality in each NW pair characterised by this GUI. Device chip label is shown above, and waveguide material below. The device chronology is presented from left to right, encompassing a total of 137 device pairs.

exponential functions. Initial guess parameters and fit-ranges are paramount to properly fitting data in the correct target region. Due to the large volume of data produced, also summarised in Table 5.3, manually altering fit ranges and initial guesses in a python script file to characterise all data quickly became an unfeasible task. Instead, I wrote an ideality fitting GUI shown in Figure 5.9, where the Shockley ideal diode equation is used to first estimate the ideality, after which the series resistance can be included in the formula to also estimate the series resistance with a root method fit. With this GUI, fitting ideality takes at most 20 seconds per subdevice. A range is drawn for reverse saturation current, then one for the ideality region, after which appropriate parameters are fed to scipy.optimize for the fit. This data is then stored in separate dictionaries for easy access. The best measured ideality from each of the 137 NW device pairs, categorised per device chip, can be seen in Figure 5.10. More details on the GUI can be found in the DMU GitHub repository[120].

5.2.2 Confirming NW Emission and Absorption

Since our initial devices were made from InP NW solar cells, whose growth has been optimised over several years to achieve low ideality and high absorption EQE in their natively grown arrays[21–23, 76, 77], we could make the assumption already that they would exhibit a photovoltaic response under a known irradiance. The initial measurements on the InP arrays demonstrated both a photovoltaic response, in addition to a linear relation between current density and light emission intensity, visible without magnification through the scope of an IR viewer.[4] When dealing with single NWs in close proximity, however, we needed to be sure that what we were measuring was, in actuality, optical communication. This means verifying both that the designated emitter NW is capable of light emission, and

[4]Measurements done by: David Alcer

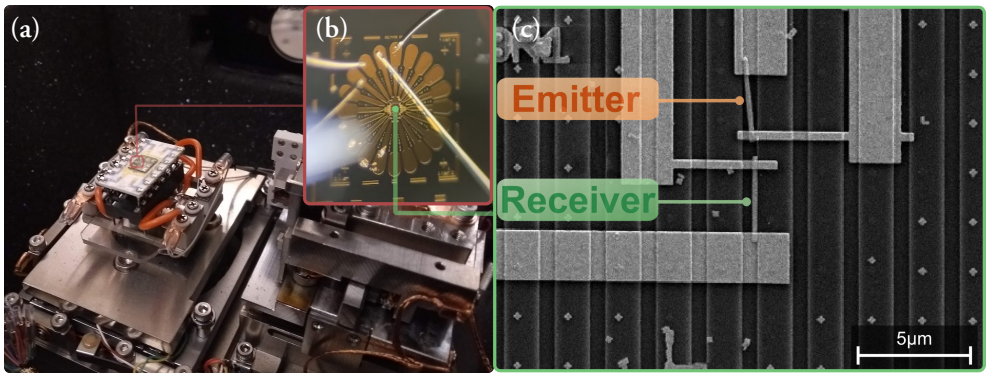

Figure 5.11: (a) Image depicting how the sample was mounted to the STM stage in the unisoku, with inset (b) showing a closeup of the wirebonded flower pattern. (c) shows the designated emitter and receiver NWs for this device pair.

that the photovoltaic response to irradiance is linear before saturation.

To test the light emission, we measured the total number of counts in dark conditions during an IV sweep over the emitter NW. The setup for this can be seen in Figure 5.11, where an STM stage, sample wire bonding, and an SEM image of the emitter-receiver pair measured on can be seen. The STM stage in question is that of a Nanonis integrated Unisoku system, which was also used as the SMU.

Images are captured with a CMOS camera mounted to a 100× objective lens over the setup. Since CMOS and IV measurement tools are operated independently, IV measurements were started after approximately 10 seconds of CMOS video recording, from which I programmatically generated matching timestamps for both measurements. By finding the time coincidence of the current and intensity maxima, and determining the time-offset between the start and end of the IV measurement, I was able to isolate and remove the video frames outside this time range, directly mapping the frame range to the measurement time.

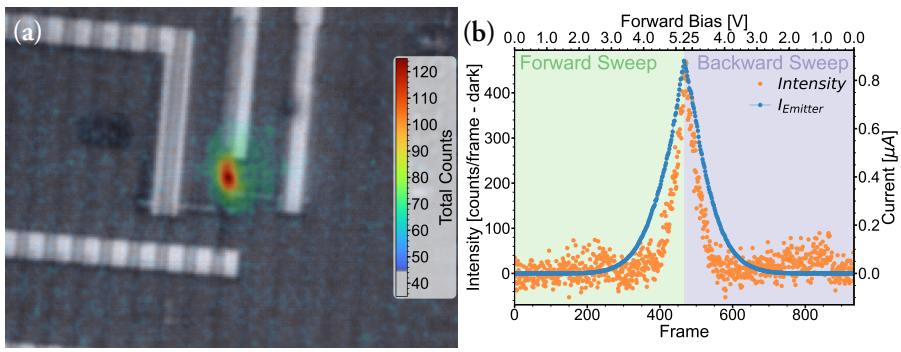

Figure 5.12: Light intensity and IV measurements of the NW device pair shown in Figure 5.11 (a) Light emission from the emitter NW captured with a CMOS camera, expressed as the dark noise subtracted total counts. (b) Dark noise subtracted total counts per frame of captured CMOS video.

Trimmed frames can be used to determine the dark noise profile, which is subtracted from the total counts of the intensity per frame. The result of this data can be seen in Figure 5.12.

For absorption, simply measuring the change in current under light and dark condition at reverse bias is sufficient, as Figure 5.13 clearly shows. As a final precaution, attempting to measure the current between any top contact through to the substrate can directly verify if we have any significant leakage. Naturally, plotting the noise profile at the noise floor doesn't look like much proof for this, so we won't show it. And with that out of the way, we are naturally ready to begin attempting to measure optical communication.

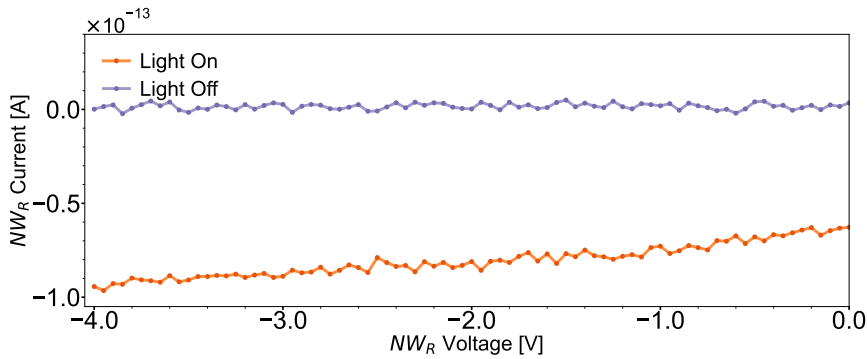

Figure 5.13: Photocurrent generated in receiver NW during a reverse bias sweep in illuminated and dark conditions.

5.2.3 Optical Communication Measurements

Finally, if the stars align, and both NWs in the device pair show good diode and photocurrent performance, we can perform steps 4-6 from Table 5.2. Step 4 is a measurement that aims to provide a reproducible standard to evaluate device performance. The applied pulses of positive and negative emitter bias measuring the emitter and receiver current, as shown in Figure 5.14 (a), demonstrate both if the device pair is capable of optical communication in the operational range, in addition to highlighting significant leakage currents, if any. The forward bias being selected to ensure that 0.7 μA is reached allows us to compare the optical coupling strength of similarly separated NW device pairs. With more measurements of varying NW separations, we can evaluate the maximum separation distances in air, and in waveguided systems, the work of which is currently ongoing. Step 6 is what we call a ladder measurement, an example of which is shown in panel (b), where we demonstrate that each optical coupling has the capability to express a range of uniquely distinguishable levels. In order to replicate the function of a biological neural network, we need our devices to be capable of a minimum analogue expression range of up to 24-32 different states, based on the estimated 4-5 bit synaptic information storage capacity of the human brain[154]. For the device shown in the figure, we estimate that upward of 40 uniquely distinguishable levels can be attained in this configuration. For a wider broadcasting scheme, similar

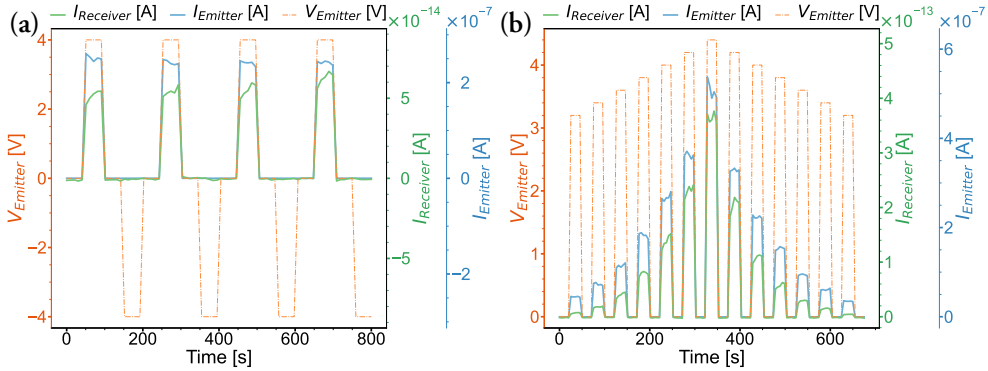

Figure 5.14: Time resolved emitter and receiver measurements in optically communicating NW device pair, where a constant reverse voltage bias of 2 V is applied to the receiver, and the emitter bias is altered. In all plots, the orange curve is the applied emitter bias, the blue curve the resultant emitter current, and the green curve the resultant photoinduced current in the receiver as a result of the light emission from the emitter. (a) Measurement of induced photocurrent I_{Rec} in the receiver NW resulting from the applied emitter bias V_{Em} pulsed in the range [–4, 0, 4] V. The lack of a current response at -4 V suggest that there is no leakage through the oxide. Unlike step 4 in Table 5.2, current compliance was not intentionally met here. (b) Ladder measurement following step 6 in Table 5.2, where I_{Rec} and I_{Em} are measured when V_{Em} is stepped in 0.2 V intervals from 3.2 to 4.4 V, starting at the detection threshold in the receiver. This measurement demonstrates the range of analogue weights achievable.

to[33], this becomes the key that enables for dynamic weights to accumulate from current summation in an artificial neuron from multiple overlapping signals[10, 13, 14] . From the numerous characterised NW device pairs, we are able to build up a large catalogue of measurements comparing the performance and yield of different device chips at various NW separations, the total sum of the best runs from each device being shown in Figure 5.15. These results, whenever relevant, also shows the difference in signal strength when a spin coated PMMA waveguide has been applied to the sample surface. Table 5.3 contains

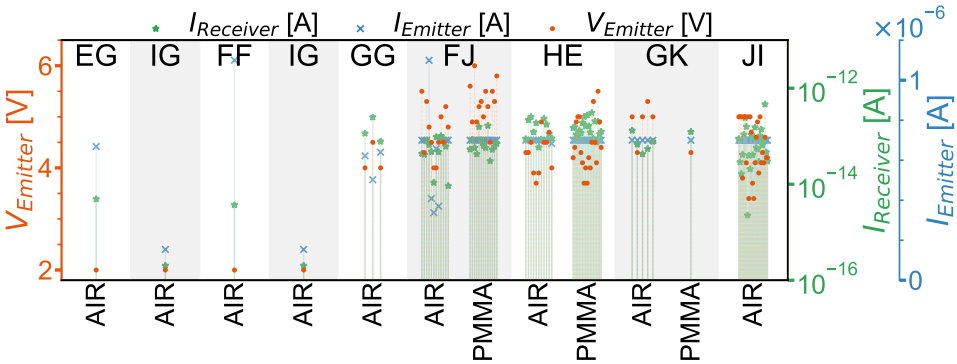

Figure 5.15: Highest recorded noise-subtracted receiver current for every characterised optically communicating NW device pair when measured using the voltage pulse scheme in Figure 5.14 (a), intended to be measured when the emitter current was set to 0.7 μA. Outlier measurements were either done before standardisation, or because of a poor quality emitter wire requiring unreasonably high voltages. The device chronology is presented from left to right, and presents data from 59 device pairs.

a tally of the total number of measurements and devices characterised for this project so far, demonstrating the consistency of our final methodology.

Table 5.3: Summary table totalling the number of measurements saved and analysed in relation to the sum of device components characterised.

Measurement Statistics		Device Statistics	
Type of Measurement	Number of	Type of Component Characterised	Number of
Single NW IV	1307	Single NWs	317
Device Pair Optical Communication	226	NW Device Pairs	83

5.2.4 Estimating EQE of Emission and Absorption

To evaluate the potential performance of these NWs when in our device configurations, we would need to characterise their EQE of absorption and emission. Normally, a tool like the Bentham - PVE300 with a tunable uniform solar simulator could be used in conjunction with a reference standard to evaluate the spectral response, and subsequently the EQE at each wavelength, which is what was done for the standing InP NW arrays we sampled for our devices[21, 77, 155]. However, for the reference sample to work, this necessitates that the spot size exposes an equivalent area of electronically contacted photovoltaic devices, which in our case means the reference sample would need to be 3000×166 nm in size, and such a sample does not exist. Fortunately for us, because we are only concerned with how efficiently the emitter-receiver pair emits and absorbs, the EQE can instead be assumed equivalent to the response of same spectra of emission. As such, we can instead form an estimate of the EQE using an alternative tool whose spectral range can be tuned to match the measured emission spectra of the very same arrays of InP NWs, namely the G2V Pico variable Solar Simulator. Through this, we are able to simplify the receiver EQE to be given by

$$EQE_{Rec}(\lambda) = \frac{I_{ph}(\lambda)}{e\Psi_{ph,\lambda}} \approx \frac{I_{Rec}}{e\frac{E_{sol}\lambda}{hc}\sigma_{NW}}, \tag{5.1}$$

where I_{ph} is the photocurrent, $\Psi_{ph,\lambda}$ is the spectral irradiance, I_{Rec} is the measured current in the receiver, E_{sol} is the solar simulator irradiance, and σ_{NW} is the absorption cross section of the NW. It is of course important to note that the solar simulator irradiance, though uniform across the substrate surface, is not monochromatic. But we can still use it to acquire a reasonable order of magnitude estimate for the EQE.

I determined a value for the absorption cross-section by creating a digital replica of the trench and NW structures in Lumerical, and used the cross-section calculation setup detailed earlier to extract the absorption cross-section, both of which can be seen in Figure 5.16, where the TSFS source was set to a centre wavelength of 910 nm, with a Gaussian emission range of [750,1050] nm. Since the solar simulator lamp does not have a means to output the spectrum, and rather only provides the centre wavelength, bandwidth and

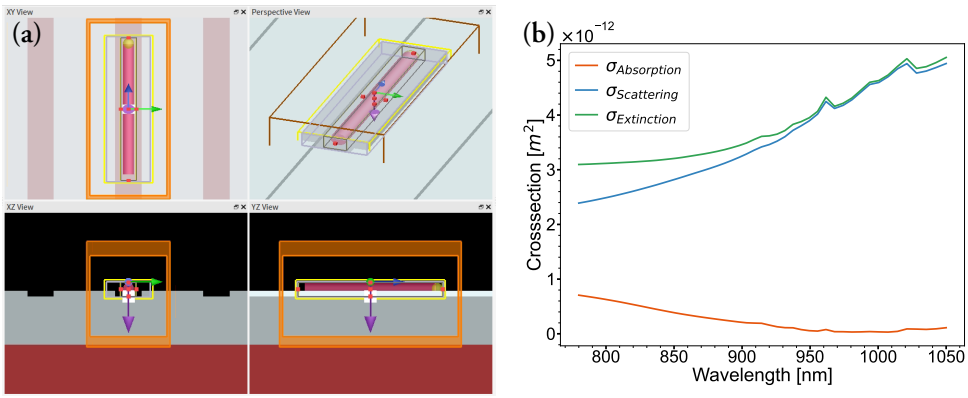

Figure 5.16: (a) FDTD viewport showing the simulation geometry used to calculate the absorption cross-section of the NW. The monitor setup is equivalent to the one described in Section 4, Figure 4.5,(b) Simulated absorption cross-sections as a function of wavelength in range of the InP NW array emission spectra. Note that the cross-section is affected by the trench structure of the oxide.

irradiance, we ultimately only calculated the EQE at this wavelength. When evaluating the current generating absorption cross-section, we make the assumption that only the 1 µm intrinsic segment contributes. As such, the projected square area cross-section of a 1000×250 nm segment would have been $\sigma_{abs,projected} = 2.5 \times 10^{-13}$ m^2 in comparison to the $\sigma_{abs,simulated}(\lambda = 910\text{ nm}) = 1.1368 \times 10^{-13}$ m^2, which would have otherwise significantly affected the order of magnitude EQE estimate, a problem whose expression is known to more greatly affect estimates for standing NWs[121]. With this data, we have

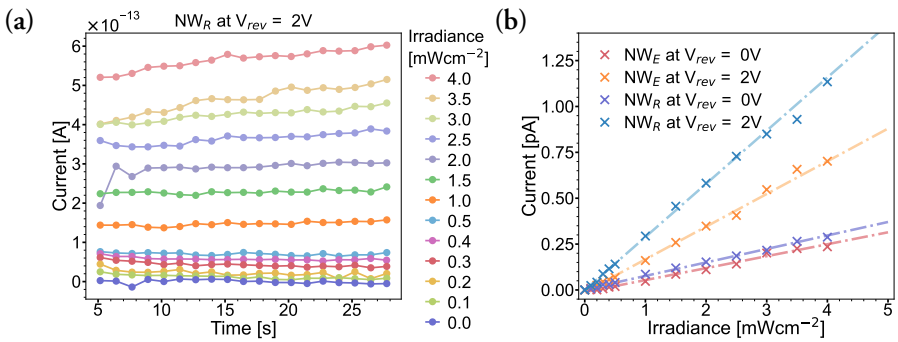

Figure 5.17: (a) Photocurrent measured as a function of irradiance in the G2V Pico from a receiver NW (NW_R) biased at a reverse bias $V_{rev} = 2$ V from a NW device pair. (b) Photocurrent average as a function of irradiance for all NWs in the device pair

effectively put together a lookup-sheet, where any generated photocurrent in the receiver NW can give us an estimate of the experienced irradiance from another source, namely the emitter NW. Now we only have one missing piece of the puzzle left, which is figuring out the fraction of emitted light that is absorbed in the receiver. For this, we can create

a cad model-replica in Lumerical of a standard device pair, on which we can iterate the NW separation to measure $P_{abs}(NW_{sep})$, namely the power absorbed in the receiver as a fraction of the total emission as function of NW separation.

In any emitter and absorbed system, the generated photocurrent I_{Rec} in the receiver can be constructed from the emitter current I_{Em}, allowing the EQE of electron-photon conversion EQE_{Em} to be inferred from the photon-electron conversion EQE_{Rec}. Naturally, just as before, this should be done per wavelength, but we will simply assume that the centre emission wavelength is representative. Now, since the simulation would be measuring the power absorption fraction directly, the absorption cross-section is not necessary. As such, we can now estimate that

$$I_{Rec} = \underbrace{I_{Em} \cdot \mathrm{EQE}_{Em} \cdot \mathrm{Pabs}_{frac}(NW_{sep})}_{\phi_{Rec}} \cdot \mathrm{EQE}_{Rec} \tag{5.2}$$

where ϕ_{Rec} becomes the photons per second incident on the receiver. From this, it naturally makes sense that

$$T = EQE_{Rec} EQE_{Em} P_{abs}. \tag{5.3}$$

This is what I used to calculate the final range estimates for the EQE of single emitter and receiver NWs, the results of which can be seen in Figure 5.18. The simulation setup, and

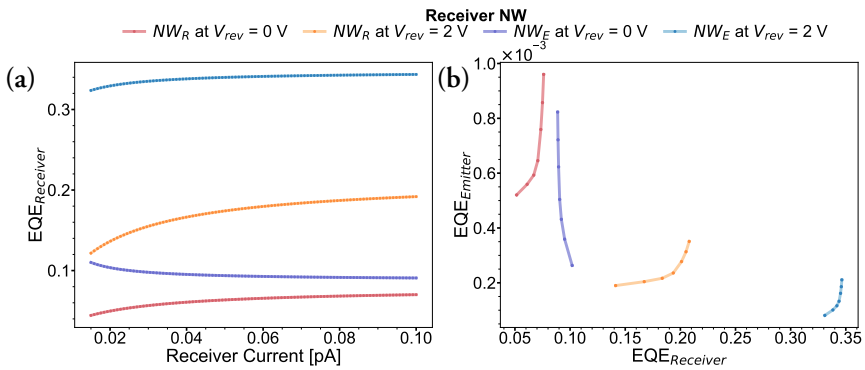

Figure 5.18: (a) Calculated EQE per measurement point in Figure 5.17 (b) using Equation (5.1) together with the FDTD simulated cross-section, the applied irradiance E_{sol}, and the measured photocurrent I_{Rec} at the indicated receiver applied reverse bias V_{rev}. (b) Emitter EQE as a function of receiver EQE, determined with Equation (5.2), where the simulated total power absorption fraction replaces the need for an absorption cross-section.

results for all possible NW orientations and presence of gold contacts that we used to get $\mathrm{Pabs}_{frac}(NW_{sep})$ can be seen in Figure 5.19. The results from this simulation also informs us that Au particle locations only minimally affects the transmission when metal contacts are present, which also enhance the transmission at larger separations. Single receiver NWs having estimated EQE values in the range of 5-35% EQE places its order of magnitude comparable to more robust measurements on standing single junction InP NW arrays[21, 70, 71, 155, 156], and within theoretical bounds[69].

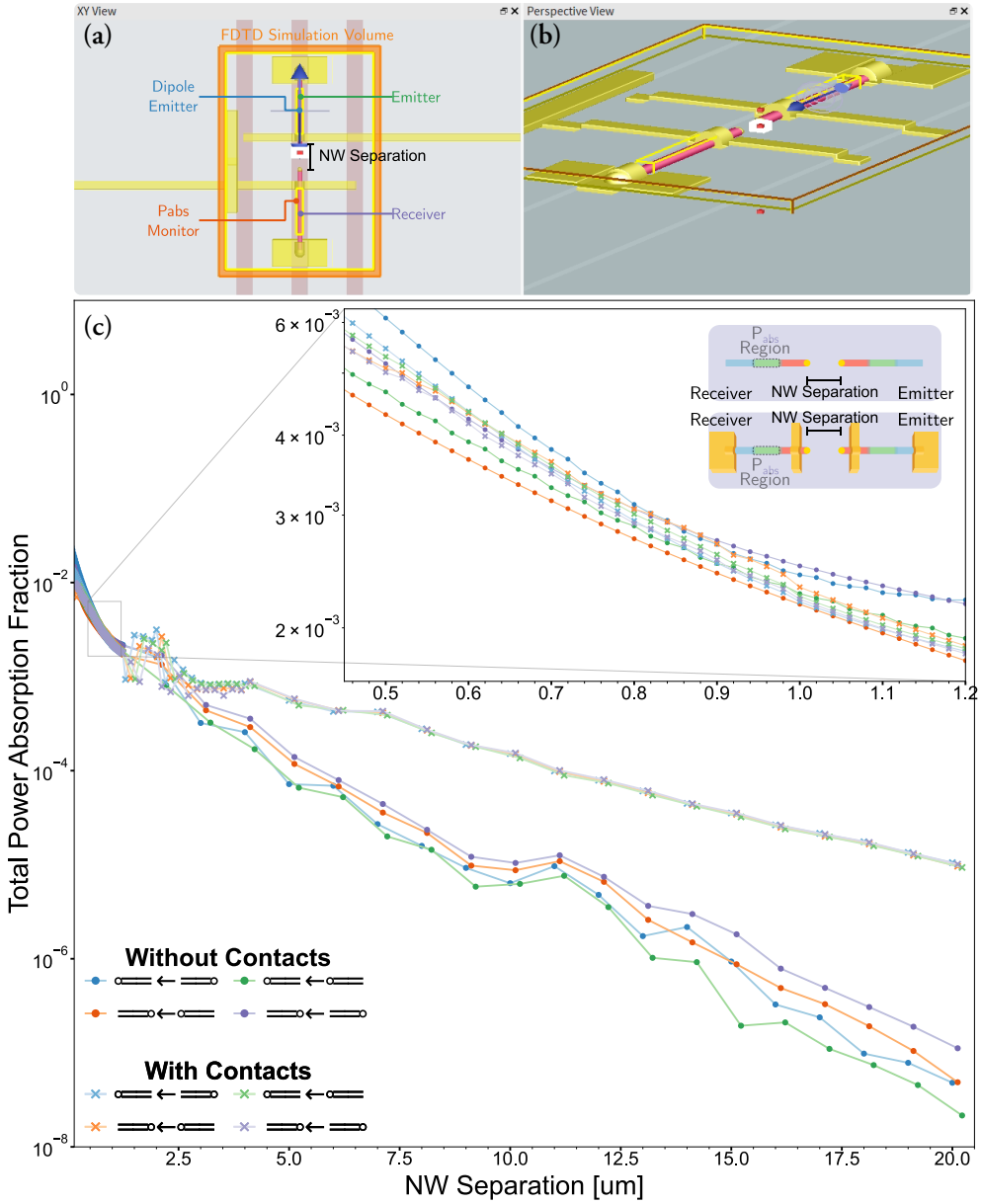

Figure 5.19: (a) Annotated top-down screenshot from Lumerical illustrating the simulation setup replicating the geometry of a contacted NW device pair in a trench structure. Note that Au structures outside the PML FDTD simulation region are underneath the substrate oxide with overwrites it during meshing. No Au intersects with the PML. (b) 3C view of the contents of (a). (c) Results from FDTD simulations plotting the total power absorption fraction as a function of NW separation. Simulation sets are done both for different NW orientations, as indicated by the legend, and when Au contacts are present or not.

5.3 Photochromic Dyes as Memory

In the optically communicating NW device pairs of the previous section, the receiver current is modulated only by the applied emitter bias. If we combine this with a medium whose level of photoabsorption can be altered by the strong incidence of a specific polarisation of light, then we can equate the receiver current to the medium's total exposure to specific polarised light. Relating this back to the Stone model, this would be equivalent to the compass neuron memory, where traversal through a specific polarisation of light increases the magnitude of a cardinal direction vector represented in the increase of receiver current[40].

In Paper IV, we explored the potential use of photochromic donor-acceptor Stenhouse adduct (DASA) dyes as the on-chip memory component that could be incorporated into a physically realised neural network of the Stone model, something we have been building towards. When exposed to a sufficiently high intensity of wavelength-specific light, these dyes can reversibly, and gradually, switch from a light absorbing state, to a non-absorbing

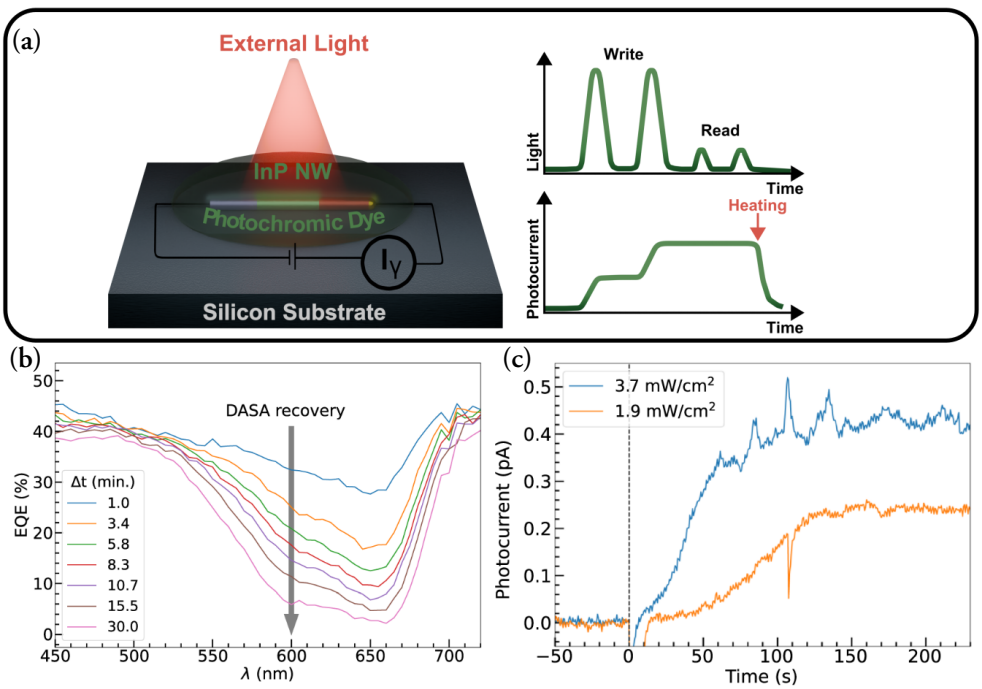

Figure 5.20: (a) Simplified illustration showing the setup used in Paper IV to evaluate the state of dye bleaching by measuring the generated photocurrent of a short-circuit connected single NW device encapsulated in the dye when under constant irradiance from the G2V Pico solar simulator. (b) EQE measurements of a dye encapsulated InP NW solar cell array, done using the Bentham PVE300 during the dye's recovery after bleaching. This shows the range of wavelengths that are most absorbed by the dye, and how quickly it recovers from photobleaching. (c) Measurement showing the generated photocurrent of the single InP NW, shown in (a), over time while under a constant irradiance. The LED whose spectral range most closely matched the absorbing range demonstrated in (b), namely 633–711 nm, was used in the G2V pico system.

state in a process we call photobleaching. And as such, similar to the analogue current steps of the optically communicating device pairs, the level of bleaching can consequently either be used to regulate photo-coupled weights between optoelectronic components on chip, or act as a long or short term memory for exposure to light[157], not unlike the compass neurons in the bee brain.

For this paper, I provided a device chip with a contacted and pre-characterised single InP NW, which is one essential component necessary to evaluate the effect of the dye on a single optoelectronic NW component, similar to what we have been proposing from the pilot study[14, 33]. Figure 5.20 (a) shows an illustration of the experimental setup, where an external light source can be used to probe the state of bleaching, by measuring the photocurrent generation in the NW with a low intensity light pulse, or to alter it, by transmitting a high intensity pulse to further bleach the dye. For memory computing, these two light-dye interactions can be considered as read and write operations respectively, with the photocurrent output representing the continuous state of photobleaching, the magnitude of which could be used as an analogue for the compass neuron memory from the Stone Model[40].

In Paper IV, InP NW-based device chips had a polystyrene suspended DASA dye spin coated onto its surface, after which the photobleaching properties of the dye could be evaluated by measuring the generated photocurrent. EQE measurements of a dye encapsulated standard size solar cell array were done in the Bentham PVE300 during the dye's recovery after bleaching, allowing us to identify the photoabsorption wavelength range, the transmission ratio, and the recovery time of the dye. Here, we see that the 600-670 nm range is most photoabsorbing. For the single NW device case, shown in (b), photocurrent measurements use the 633-711 nm LED in the G2V solar simulator. Results show that the rate of photobleaching is significantly greater at higher irradiance, and that there is no observable photobleaching change in the lower irradiance measurement within the first few seconds. These findings consequently demonstrate the potential to use two different light intensities

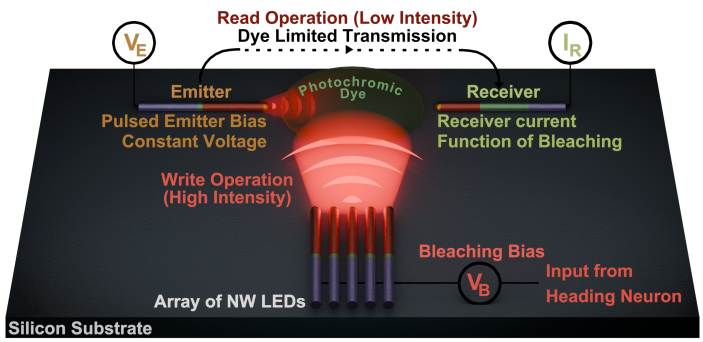

Figure 5.21: Illustration of how an on-chip memory component using DASA dye to modulate the signal between communicating NW device pairs. An external polarisation sensor would regulate the input biasing of the NW emitter array, optimised to have emission at 650 nm in order to act as a bleaching agent.

to read and write to the dye.

For integration into an on-chip component, the basic memory could instead rely on something akin to the device concept illustrated in Figure 5.21, where we combine the optically communicating NW device design from Paper I, replacing emitter component materials with one whose centre emission wavelength is 650 nm, such as InGaP. These emitters can be coupled to a photogated component (not pictured) that transmits a bias to the array of NW LEDs, who in turn perform a write operation, progressively bleaching the dye. Now, instead of having a variable emitter bias control the receiver photocurrent, low intensity pulses can be sent from the emitter in a read operation, resulting in a receiver photocurrent output that is dependent on the bleaching. Work on this device concept is currently ongoing.

CHAPTER 6

Simulating Broadcasting Networks

'We have learned more about the brain in the last fifteen years than in all prior human history, and the mind, once considered out of reach, is finally assuming center stage.'
—Michio Kaku, The Future of the Mind

So far, we have discussed the work done at the individual component level, on the fabricated optoelectronic systems whose development, and eventual combined functional purpose, builds towards a multi component neuromorphic broadcasting system. However, in the current state, these networks are reliant on the symmetric distribution of weights around each emitter, something that was instrumental in replicating the mapped activity in the compass neurons of the bee[33, 40]. This logic differs significantly from the more recent implementations of large convolutional neural networks (CNNs), wherein there exist several hidden layers between the input and output that we just don not fully understand. Instead we focus on networks such as the insect inspired Stone model [40] in which a large part of the network is hardwired to give functionality. Memory components like optical dyes acting as synapses (discussed at the end of Chapter 5) can then be added in part of the network (as the memory nodes in the Stone model) or input-output can be trained as in a reservoir network described below. This section will discuss two different FDTD simulated works, one that focuses on training a neural network from a random distribution of weights, and another that demonstrates how we can use nano-antenna components to modify the weights in a fixed network with two layers.

6.1 Echo State Networks

Let us imagine a uniform standing NW array, where each point on the array has a NW emitter and receiver neuron. In a fully homogeneous system, should we evaluate the optoelectronically coupled weights each node has to its neighbours, then the only factor determining its amplitude is distance and occlusion. If we can knock every single NW down in a random orientation, then the interconnected weights are now randomised for the immediate vicinity of every single node. This configuration would allow us to replicate the idea behind an echo state network (ESN), which is a form of reservoir computer making use of a recurrent neural network (RNN). This type of network, first, proposed in 1992[158], use

a sparsely populated randomly connected pool of neurons whose weights are fixed and randomly assigned, just like our toppled over array of NW neurons[159]. This configuration, as a side effect of the inverse square law, also fulfils the suggestion that most weight elements in the matrix are assigned a zero value[158, 160, 161]. We simulated a variant of this network in FDTD, using a conceptual replica of the NW neuron detailed in[14], where the emitter NW is stacked on top of the two-part receiver. Unlike this approach, other research has proposed reservoir networks that instead make use the electrical pathways formed between defined metal contacts through the random interconnections from toppled NWs, demonstrated in either simulated[162] or experimentally realised forms[36, 163, 164]. Both of these networks are trained in the same way, with a layer of digital output neurons whose weights are tuned over the original fixed sparse network weight and input data using the supervised learning principle. To obtain a good metric to evaluate the predictive capabilities of these networks, the output can then be trained for a set time interval on some type of data, usually a chaotic time series like the set of Mackey-Glass equations[165], before being set free to predict the future values of the formula. Specifically, the learner network is trained on $t \in [0, T_{train}]$ number of points from generated Mackey-Glass data in the form $y_{target}(t)$, where for each point t the network makes a prediction $y_{predict}(t+1)$, to which it receives a correction from the supervising agent against the real value $y_{target}(t+1)$[166]. For each prediction, the output neuron weights are tweaked programmatically, until the network is finally let free for an interval $t \in [T_{train}, T_{train} + T_{future}]$, where the normalised mean root square error σ_{nmrse} against the real data gives us a metric for the network performance.

6.1.1 Network Creation and Weight Generation

The simulated network, in theory, is built up from nodes on a square aspect ratio hexagonal grid with a 5 μm pitch, on which an emitter and receiver pair are instanced as a stack, each with random rotation. As can seen in Figure 6.1 (b), the emitter has three in-plane dipoles to simulate non-homogeneous emission, and the receiver has 'activator' and 'inhibitor' Pabs monitors encapsulating part of each end-segment. Every node is given an index, reading left to right, and row-wise bottom to top, as seen in Figure 6.1(a), which also accurately shows the grid cut-off. Weights are calculated from receiver node i, as a function of the dipole averaged power absorption difference between activator and inhibitor induced by each emitter at node j, otherwise given by

$$W_{i,j} = \frac{\sum_{k=1}^{3}(\mathrm{Pabs}_{\mathrm{activator,i,j_k}} - \mathrm{Pabs}_{\mathrm{inhibitor,i,j_k}})}{3}. \tag{6.1}$$

Here, $W_{i,j}$ is the weight, expressed as the effect in receiver node i from emitter node j and its dipole given by index k. We will refer to each network by its total number of nodes, meaning that e.g. an N36 network has 6 rows, with 6 nodes per row. We simulated[1]

[1]Simulations and weight generation done by Kristians Draguns

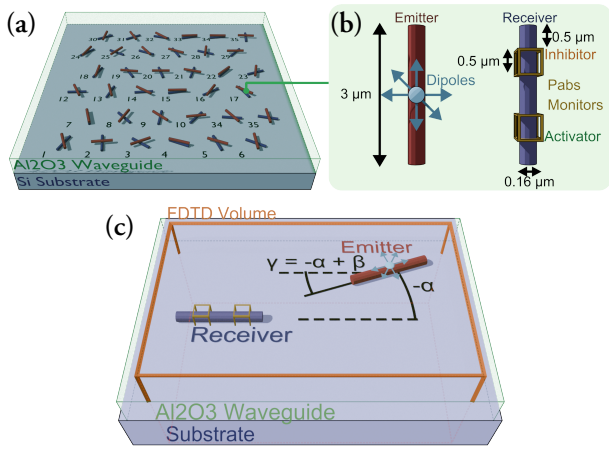

Figure 6.1: Diagram showing (a) visualisation of what a full NW reservoir network looks like. (b) emitter and receiver dimensions and setup. (c) the simulation setup used to build up a catalogue possible weights to distribute around each N×M sized network.

100 networks for each N16, N36, N100, N400 and N1024s size, with separate weights generated for wavelengths 750 nm, 800 nm and 830 nm, achieved by altering the centre wavelength of emission on the dipole. However, as described in Section 4, large simulation volumes with rounded small-scale features need an extreme amount of RAM to run accurately due to the dense simulation grid required, making full-scale network simulations unfeasible. Instead, all possible combinations of emitter-receiver rotation and separation within 2 pitch distances are evaluated separately, with one example shown in Figure 6.1(c). This allows us to build up a weight index map $W(\alpha, \beta)$, shown in Figure 6.2, which can then be used to populate any number of different networks without needing to simulate the entire geometry.

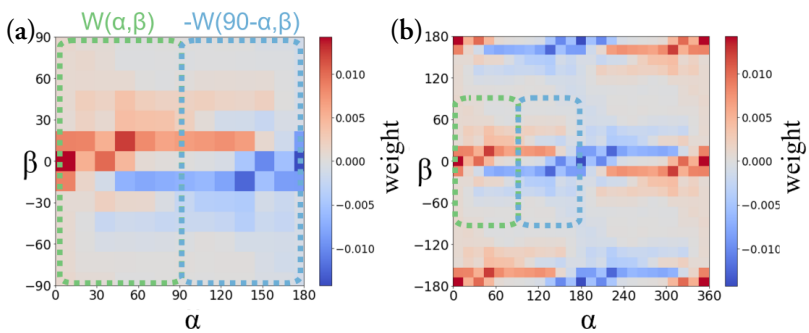

Figure 6.2: Weight index $W(\alpha, \beta)$ maps generated from the nearest pitch distance away. Due to rotational and positional symmetry, (a) shows the value mirrored expansion of the simulated range $\alpha \in [0, 90]^\circ$ and $\beta \in [-90, 90]^\circ$ to fill $\alpha \in [0, 180]$. (b) shows how further symmetry allows for expansion over 360° in both α and β.

6.1.2 ESN Training and Data Evaluation

For network training, I used a publicly available repository known as PyESN[167]. For each of the 1500 different network weight matrix files provided (5 sizes, 3 wavelengths, 100 array configurations), I trained separate models for $T_{train} = [100, 500, 1000, 2000]$ and evaluated the σ_{nmrse} given by

$$\sigma_{nmrse} = \frac{1}{\sigma_{target}} \sqrt{\frac{\sum_{i=1}^{N} (y_{target,i} - y_{predict,i})^2}{N}} \tag{6.2}$$

against $T_{future} = [100, 500, 1000, 2000]$. To illustrate what the connected weight matrix files look like once configured into the hexagonal array, we can look at the network pairs in Figure 6.3 (a)-(b) and (c)-(d). These figures show two differently performing N36 networks, (a) and (c) illustrating emitter and receiver NW placement and orientation, along with visually indicating the strength and coupling of weights otherwise shown per-index in complementary panels (b) and (d) respectively. To look at the performance of each net-

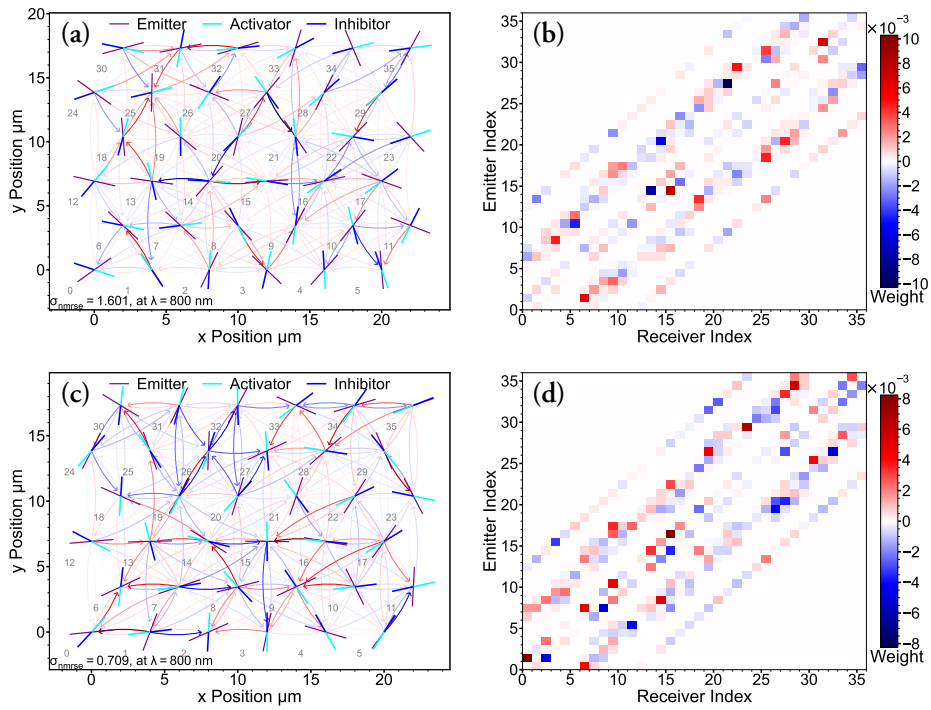

Figure 6.3: (a)/(c) To-scale illustration of the location and rotation of the inhibitor-activator receiver and emitter NWs in each index-labelled neuron node. The weights, also shown in the index map in (b)/(d), are drawn per receiver as colourbar matched arrows pointing from the relevant emitter to the receiver node. Weights whose value is $0.01W_{max}$ are omitted from (a)/(c). (a) shows the worst performing non-diverging network, and (c) the best from $T_{train} = 2000$,$T_{future} = 500$

work, while calculations of the σ_{nmrse} will tell us if the system is diverging or not rather

readily, differentiating between how well the network can predict both feature location and amplitude is another factor that is hard to quantify. For instance, if take the networks from Figure 6.3, and look at their performance after $T_{train} = 2000$ compared to an $N = 1024$ network, shown in Figure 6.4, we see some key differences. The well performing $N36$

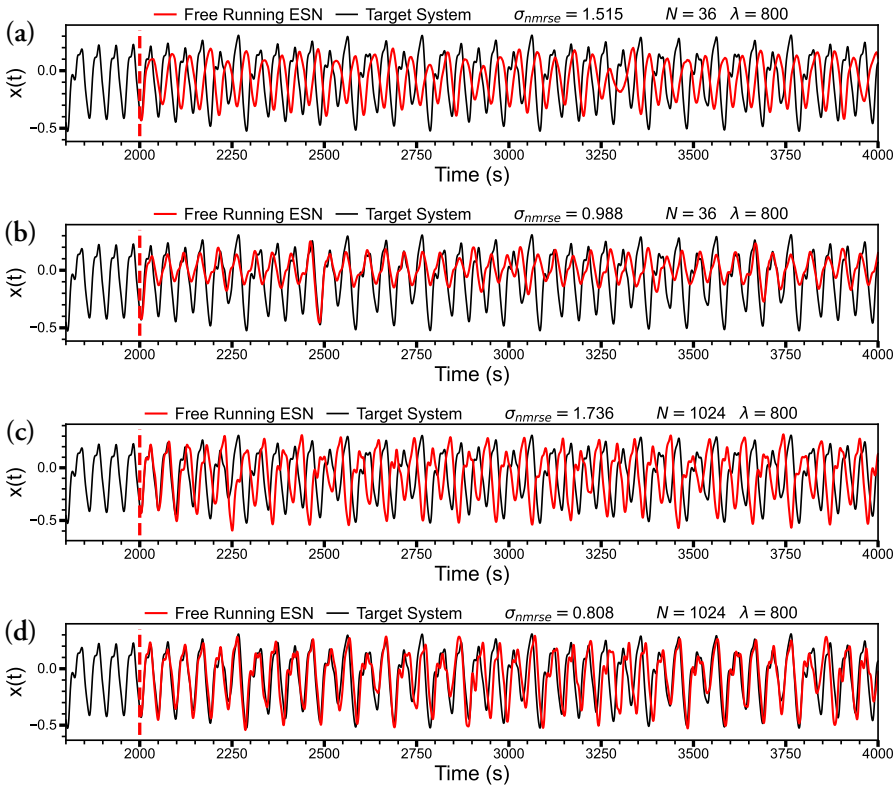

Figure 6.4: Diagram illustrating the different ranges of predictive behaviour between low and high σ_{nmrse} systems for different N sized networks. Each trace shows the Mackey-Glass training data as the target system, and the freely running ESN predictive trace from T_{train} to T_{future}. (a) Highest non-diverging $N36$ network, same as Figure 6.3 (a)-(b). (b) Lowest σ_{nmrse} $N36$ network, same as Figure 6.3 (c)-(d). (c) Highest non-diverging σ_{nmrse} $N1024$ network. (d) Lowest σ_{nmrse} $N1024$ network.

network in (b) shows good temporal prediction, but cannot match the amplitude, unlike the $N1024$ network in (d). Both poorly performing networks in (a) and (c) show similar repeating patterns as the target data, but with a large temporal mismatch. A shortcoming of σ_{nmrse} as an evaluation tool is that a $y_{predict}$ composed of all zeroes will score better than one with a minor temporal mismatch.

Figure 6.5 summarises the difference in σ_{nmrse} between the same differently sized networks set free for T_{future} = 500 when trained for $T_{train} = 500$ for all three wavelengths evaluated at. The results from this paper show that a high percentage of larger networks are capable of some level of Mackey Glass prediction, or at the very least are capable of pro-

ducing an output with the correct magnitude and variation, just like we see in Figure 6.4 (c). Smaller networks, however, do not reach a, perhaps less classifiable, saturation point governing the number of weight pathways necessary for function[160, 161]. More analysis on this can be read in Paper v.

Regardless, we find a high yield of networks capable of producing low σ_{nmrse} values in chaotic time series prediction. This shows the potential for an optical ESN made from a substrate randomly populated with III–V NWs.

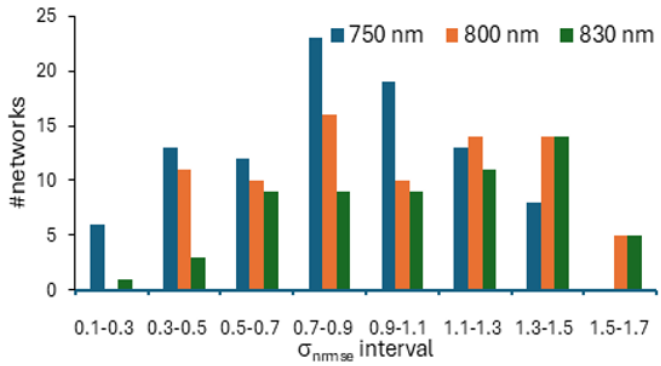

Figure 6.5: Histogram of the final σ_{nmrse} ranges for 100 N1024 networks after $T_{train} = 500$ and $T_{future} = 500$ evaluated at different wavelengths. In general, $\lambda = 750$ nm performed better overall compared to the other wavelengths. Networks whose $\sigma_{nmrse} > 2$ are not included, but total 6, 20 and 38 for wavelengths 750 nm, 800 nm and 830 nm respectively.

6.2 Yagi-Uda Guided Networks

While the geometrically symmetric weights presented in [33] accurately mimic the neural weights from the Stone model[40], expanding the possibilities offered by optical broadcasting in artificial neural networks requires the ability to purposefully guide the light down specific pathways. Further, the relatively low transmission between the optically communicating device pairs from Paper I-II raised many questions of how the coupling efficiency could be increased beyond blanket waveguiding. One of the ideas presented was to use a nanoscale plasmonic antenna based on the Yagi-Uda[168] design, the classic TV antenna found on many houses in the last century. It functions on both receiving and emitting components, relying on a reflector element behind the target and several directors in front that guide both inbound and outbound signals. Only more recently has it been explored in nanoplasmonic systems for optical signals with promising results for external in-coupling[169], and has shown promise for our specific on-chip use-case[109, 170, 171]. A diagram of the nanoscale antenna coupled to our light emitting NW can be seen in Figure 6.6 (a), where our InP NW acting as the feed, is positioned perpendicular to the regular orientation due to the increased absorption cross-section offered by this placement. If a

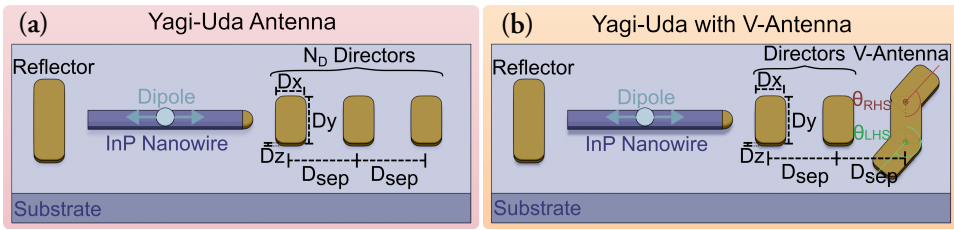

Figure 6.6: a) Yagi-Uda InP NW-based nanoantenna[109, 170, 172], featuring several leading director structures modelled after Au evaporated features on a substrate. (b) The structures in (a) modified with a two sided V-Antenna [173, 174] replacing the last director in the sequence.

director element is replaced with a so-called V-antenna, seen in (b), then the rotation of either Θ_{RHS} and Θ_{LHS} uniquely directs the outbound light[173, 174]. The dimensions of these metallic director elements are usually smaller than the wavelength, meaning that for the wavelengths that our different NW emitters operate at (650 and 910 nm), we could feasibly evaporate such contacts in tandem with the contact metallisation step for the NW devices, which would not add to the complexities of fabrication. In this section, we will discuss the results of a linear system of emitter-receiver nodes modified with Yagi-Uda and V-antenna components to alter the weight coupling of the system.

6.2.1 Model for a Linear Broadcasting Network

The design chosen for our simulated broadcasting network, the building block of which can be seen in Figure 6.7, mimics that of the standard appearance used to visualise the input-output nodes of a conventional CNN. The model morphology, as a whole, builds on the cumulative work we have done so far. The substrate on which NW and antenna are placed consists of 1000 nm of SiO_2, with a 250 nm thick Al_2O_3 waveguide, chosen based on previous optimal values simulated in Paper I. Here, each node has a emitter-receiver pair,

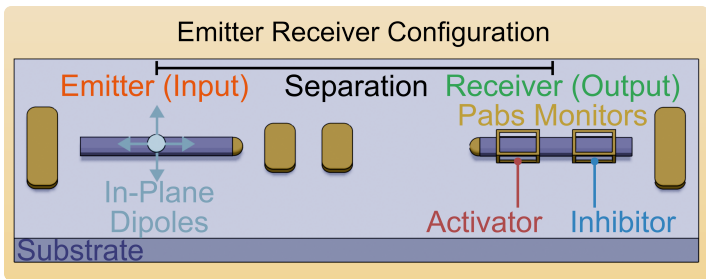

Figure 6.7: Simulation setup for a single emitter-receiver node, showing dipole placement in the emitter, with activator and inhibitor Pabs monitor placements in the receiver. These can be assembled into networks with any number of nodes, such as the 7 node system shown in Figure 6.10 (b), where the nodes are given corresponding E_n and R_n labels, with the end director optionally being modified with a V-antenna, denoted by a nonzero Θ_{LHS} and Θ_{RHS} value.

whose NWs are modelled after the 3 μm long, 176 nm wide InP ones used for simulations in Paper I. NW centres are separated by 7 μm, in adherence to similar separations used in [33], with each emitter having a complete antenna, with only a reflector on the receiver side. To improve simulation accuracy, director and reflector components, when present, are encapsulated by 2 nm resolution mesh objects, with all NWs encapsulated by a 10 nm mesh object. Every emitter node is separated from the next by 2 μm, since cross-talk between emitter nodes can be disregarded. Finally, each receiver has two 750 nm long Pabs monitors, separated by 500 nm, tightly encapsulating the NW, one designated an 'activator', and the other an 'inhibitor', the difference of which is what defines the output weight. Simulations are performed twice, once for each of the shown dipole directions. Similar to Paper V, the resultant weight is given by

$$W_{i,j} = \frac{1}{2}\sum_{k=1}^{2}(\mathrm{Pabs}_{\mathrm{activator,i,j_k}} - \mathrm{Pabs}_{\mathrm{inhibitor,i,j_k}}). \tag{6.3}$$

While in a physical system, the dipole-like emission of a NW p-i-n junction should be modelled as the weighted contributions from a random number of dipole orientations, we chose instead to limit our simulations to only the dipole whose emission losses through the NW geometry was the lowest. Similar to the pilot study[33], we found that dipoles whose electric field component is parallel to the NW orientation had the lowest losses. However, before this network can be simulated, the ideal parameters for both director morphology and separation must be determined.

6.2.2 Determining Ideal Director Structures

Each individual element is considered a non-uniform rounded cuboid, with a near-flat base, rounded vertical edges, with more rounding on the top edges, similar in appearance to those in Figure 6.6. To determine their ideal dimensions, the simulation setup described in Section 4, Figure 4.6, is used. Here, only the forward and reverse scattering transmission is measured, the value of which will be proportional to the forward and reverse scattering cross-sections. Initial measurements, detailed in the SI of Paper III, first performed this measurement over a smaller range to determine the ideal $D_z = 60$ nm, after which we produced the results in Figure 6.8, where $D_x, D_y \in [10, 1225]$ was evaluated. From the results in Paper I, and work done afterwards, we already know that the maximum NW separation in our InP emitter-receiver pairs is approximately 3 μm in air, and as such we wanted to constrain our network to separations less than 8 μm in a planar waveguide, especially now that the resultant current is made up only 1/4 of the available absorption volume. This led to us disregard the second, greater, maxima beyond the limits of the simulated D_x region, opting instead to operate from director dimensions $[D_x, D_y, D_z] = [485, 350, 60]$ nm. A director D_z of 60 nm could feasibly be an evaporated thickness of material in NW devices with a smaller radius, but not for our InP devices from Paper I that require 165 nm of material. From the results in the SI, however, it should be noted that a D_z of 160 still

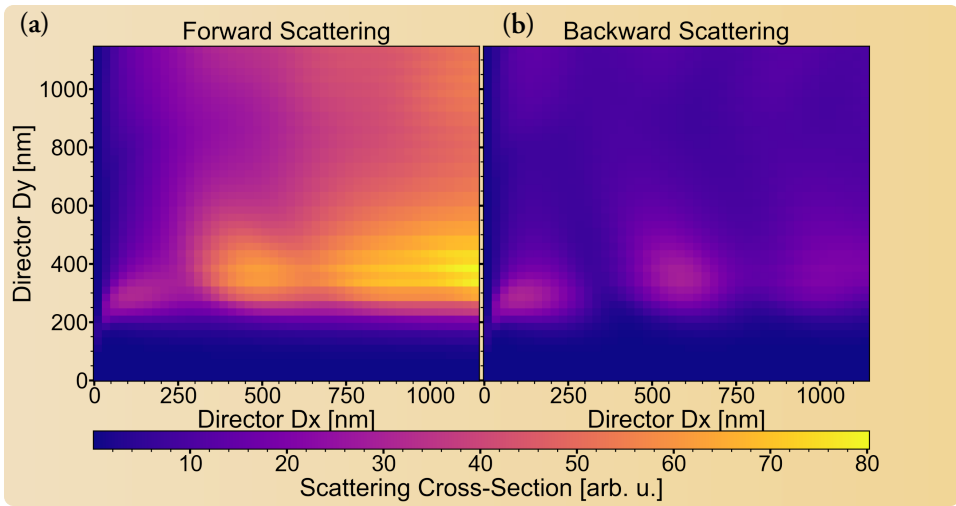

Figure 6.8: (a) and (b) respectively show the forward and backward scattering resulting from the injection of a TSFS source with centre wavelength $\lambda = 910$ nm against the -x axis one of the symmetric director element shown in Figure 6.6 evaluated for $D_x, D_y \in [10, 1225]$ at a constant $D_z = 60$ nm. The colourbar shows the power transmission as arbitrary units of the scattering cross-section.

produced significant forward scattering, and could already be incorporated as a transmission boosting component.

Following this, we must find the ideal director number, and separation. This is done by measuring the summed Pabs from activator and inhibitor segments, while iterating on the total number and separation of the detector structures, and determining which com-

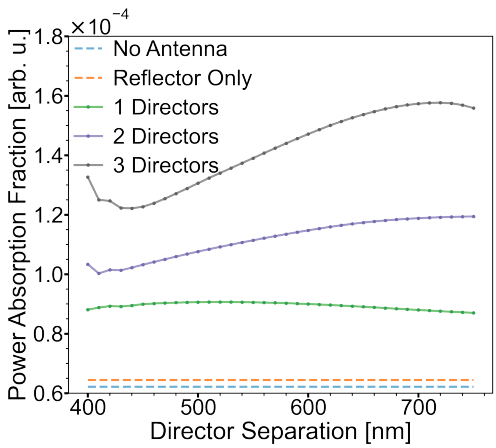

Figure 6.9: Director number and separation as function of the power absorption in the receiver NW, as compared to no director and only a reflector. Pabs improves by a factor of 1.5, 1.9 and 2.6 for 1,2 and 3 directors respectively compared to the no-antenna case.

bination results in the greatest total signal. This result is shown in Figure 6.9, which was done using the single-node setup shown in Figure 6.7 (a). From this, we determined that, while the benefit offered by 3 directors is significant, the space they occupy beyond the NW becomes a limiting factor on the potential effect of light guiding that the V-antennas could have. As such, we settled on using only 2 directors for all measurements. The very same director structures and ideal separations were subsequently used for the V-Antenna wings. Extensive work was also done on determining the change in directivity through the V-antenna, probing the potential configurations that could produce the greatest change in the full network. These results can be seen in Paper III, with additional plots shown at the end of the supporting information.

6.2.3 Simulated Light Guiding Networks

With individual component performance evaluated, I can now show results from the full network described earlier. I chose to use 7 emitter nodes and 7 receiver nodes, an example of which can be seen in Figure 6.10 (b). This compact configuration of 7×14 μm ensures that all nodes are at least weakly, but quantifiably, optically coupled to one another, allowing us to define 49 individual weighted connections with no wiring. I performed FDTD simulations for three V-antenna networks, in addition to a fourth control network composed of only the symmetric Yagi-Uda antennas. The configurations of each network, defined by their $\Theta_{LHS}, \Theta_{RHS}$ values, are listed in Table 6.1 and are referred to throughout by their respective Network IDs.

To assess the spatial distribution of optical signals, a frequency-domain monitor was placed in the x–y plane intersecting the NW centres. This monitor records electric field components E_x, E_y, E_z that pass through it, which are typically represented as the total field intensity, expressed by the absolute vector magnitude $|\bar{E}|$. Figure 6.10 (a) shows a comparison between the emitter node E_2's performance in both networks II and III. Highlighted is a clear indication of a greater signal reaching the activator segment of node R_6 in network II, as a consequence of the V-antenna design. To further illustrate the variance in performance between V-antenna configurations, Figure 6.11 shows the difference in total field intensity when the result for each respective node is subtracted from that of the same

Table 6.1: V-antenna configurations for three simulated networks, where Θ_{LHS} and Θ_{RHS} according to Figure 6.6 (b) are listed for each node emitter E_n, where a value of 0 indicates that the wing in that position is not present.

		Rotation at Node [°]						
Network ID	Θ	E1	E2	E3	E4	E5	E6	E7
I	LHS	80	80	80	220	0	0	0
	RHS	0	0	0	0	80	80	80
II	LHS	0	0	0	0	80	80	80
	RHS	80	80	80	0	0	0	0
III	LHS	0	0	0	0	80	30	80
	RHS	30	70	80	320	60	30	0

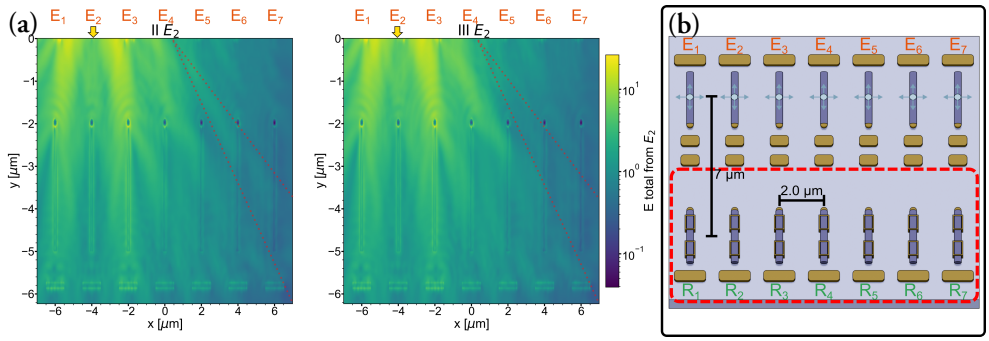

Figure 6.10: a) E-field intensity captured by a frequency domain monitor (measuring the x-y plane at z equal to the NWs radius) in the lower half of networks II and III for the emission of node E_2. A dotted line highlights a specific difference between the field intensities affecting R_6, indicating the function of the V-antenna. (b) Sketch of the Yagi-Uda simulated emitter/receiver antenna system. The red box indicates the area shown in all other plots.

node in network IV. This differential analysis reveals clear changes in signal distribution due to the V-antenna geometry. In particular, there is a significant reduction in electric field intensity over the activating segment of Network **II**, indicating effective suppression of propagation to that region.

When evaluating the weights using Equation (6.3) for all networks, we get the results shown in Figure 6.12. In panel (a), we show both activator and inhibitor Pabs values used to calculate the final weight matrix, shown at the bottom, illustrating clear asymmetry of weight distribution in comparison to the Yagi-Uda network reference. To further highlight this effect, in (b), we compare the asymmetric configuration to the symmetric Yagi-Uda arrangement, showing the resulting difference in weight matrices. Even with limited testing, the introduction of asymmetry clearly produces substantial variation in the weights. Notably, due to the compact nature of this configuration, modifying a single emitter's antenna influences the weights of other, unmodified emitters as well. In this case, it is primarily

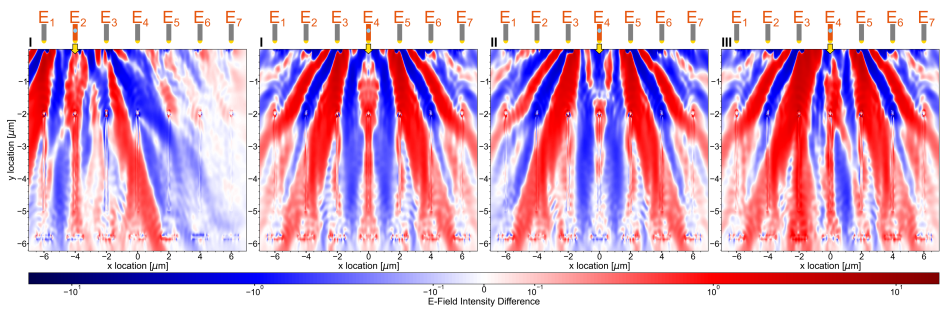

Figure 6.11: Intensity difference maps between network IV, and each of the labelled networks from Table 6.1 and their respective emitter. The injection axis is labelled by a yellow arrow, and by an accompanying red illustration of the labelled emitter node. The difference in total electric field intensity illustrates the individual performance of each V-antenna component highlighted.

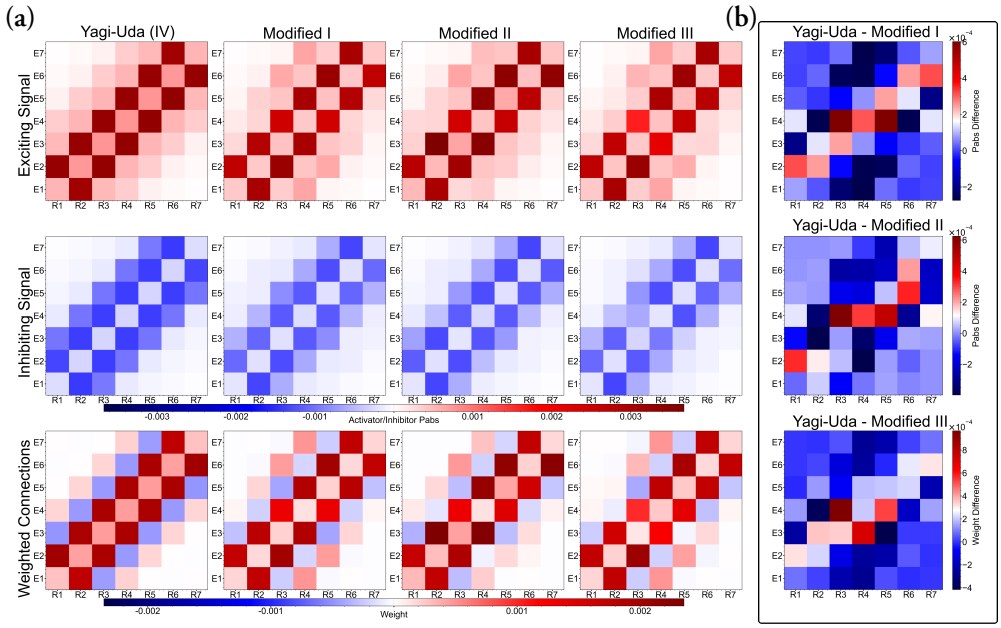

Figure 6.12: (a) Pabs induced in activator and inhibitor segments in receiver R_n by emitter E_n, and the resultant weight produced by their difference in four different networks, labelled above. The first two rows share a colourbar, representing activator and inhibitor segments respectively, where inhibitor Pabs is assumed to be negative. The bottom row shows their sum, which is the network's resultant weights. (b) Matrices showing the difference in weights calculated as the symmetric Yagi-Uda network, subtracted by each of the three asymmetric network weights. Configurations for each network can be seen in Table 6.1.

the magnitude, rather than the sign, of the weights that is altered. Achieving a complete change in sign would likely require modifying the geometric arrangement of the inhibitory and excitatory segments within the active nanowire elements, or the introduction of a more complicated waveguide arrangement to more strongly couple network nodes. As expected, a general focusing effect is observed from the antenna design, yet considerable asymmetry between elements is still achievable.

These results show that symmetric and asymmetric Yagi-Uda antennas, composed of active III–V nanowires and passive gold elements, can focus and direct light within nanophotonic emitter–receiver networks. Asymmetric layouts offer a degree of control over coupling and light splitting, with complex connectivity emerging from relatively modest structural changes. This approach supports compact, tunable optical networks, though achieving precise connection patterns will likely require iterative adjustment of antenna geometry and emitter–receiver placement.

Finally, before we wrap everything up in the outlook, I would like to highlight the overall scale of the FDTD simulation work carried out during the projects discussed in this thesis. Naturally, the summary in Table 6.2 only includes simulations for which results were saved and analysed, and does not account for runs whose data were discarded or unused. Altogether, this work represents an estimated three months of continuous simu-

lation time on our in-house simulation PC, representing yet another compelling reason to develop more energy efficient device architecture.

Table 6.2: Summary table totalling the number of simulations I have saved and analysed. The left table covers all done for Paper III, and the right for Papers I – II. In total, I analysed the results of 20862 FDTD simulations.

Type of Measurement	Count
Director cross-sections	17153
Director Separation	749
Antenna Directivity	954
Full Network Weights	133

Type of Simulation	Count
NW Separation as function of Pabs	317
NW Device cross-sections	48
Waveguide Thickness Optimisation	720
Trench Geometry Impact on Pabs	30

CHAPTER 7

Outlook

The work presented in this thesis showcases advancements in what can be achieved with on-chip optoelectronic III-V NW devices, focusing on the aspects of optical communication via broadcasting, and its potentials for applications in biologically inspired neural networks.

The development and characterisation of III-V optoelectronic device pairs presented in Papers I-II expands on the possibilities of single NW device design, assembly, and purpose. With the first working on-chip component capable of optical communication, we have demonstrated that the fundamental building block needed to realise larger broadcasting networks is possible. The development of a flexible fabrication pipeline with yields upwards of 80% for these devices also further illustrates the level of complexity attainable, serving as proof that the precise assembly of upwards of tens to hundreds of integrated NWs of various species is fully achievable for on-chip purposes. Some improvement in yield might be necessary to make functional networks, but if we build redundancy into the networks, then they may still function even if not all components operate perfectly. With the investigation into the properties of photochromic dye for on-chip applications in Paper IV, we demonstrate a candidate memory medium capable of replicating the synaptic behaviour in the bee brain, as in the Stone model[40] used for memory neurons. As with any ongoing work, the future outlook for these projects is multifaceted and exciting.

With the flexible assembly discussed in Papers II, we have the potential to realise any number of complex device architectures. Furthermore, due to the fabrication being done on a wafer with 1000 nm of oxide, the type of which should not matter exactly, the entire process can be considered CMOS compatible. While Au is normally a forbidden material in CMOS processing, our process can be done on already completed CMOS template chips, which can act as the logic for the optical NW components above. Integration between these two layers can be done with copper pillar contacts, exposed through the oxide using chemical-mechanical planarisation[175]. While optical communication of distances up to 3micron was experimentally achieved by components in air, optical communication across a complete circuit of 10-100 μm distances will be needed. For this we need to implement a waveguiding material around the NW devices as a natural next step. While blanket coverage planar waveguides can improve the transmission by upwards of 20$\times$, in the case of Al_2O_3, coupled tunnel waveguides may be necessary to retain more of the signal, which

is something our collaborators at INL in the InsectNeuroNano project have been working on[176]. Another future use is to use the optically communicating device pair from Paper I, as local sensors detecting changes in the optical signal.

For implementing memory, however, using Al_2O_3 might make dye integration more difficult, but the polystyrene itself, that the dye is suspended in, can also act as a waveguiding material. With the memory needing to be localised to a specific region, a UV lithography tool could be used to accurately permanently bleach the dye in all non-memory areas, leaving behind a polystyrene based planar waveguide everywhere else. Alternative dye deposition or removal techniques otherwise need to be expanded upon to allow for their direct integration.

For the implementation of NW neurons in [33] and Paper III and Paper V divided up a simulated NW into segments that act as exciting and inhibiting regions. But in order to experimentally realise the function of such a neuron, presented in more detail in [14], we could grow a specialised tandem junction NW whose segments target different wavelengths, like in[24], or spatially separate two connected single NWs. The latter approach makes up a project nearing completion, where the InP NWs used in Paper I are precisely positioned parallel but with opposing orientations, separated by a few μm, and connected to the gate passing underneath a single InAs NW, acting as a FET. The purpose of this is for each NW to act as either an inhibitor or excitor, where a strong enough light signal impinging on the exciting NW should sufficiently bias the gate of the InAs to let through a bias. This device has already been tested with an externally coupled light source, demonstrating a significant and measurable change in the InAs conductance for activating and inhibiting signals. Alternatively, the concept could be coupled together with a polarisation sensor, allowing it to mimic the polarisation-sensing abilities of the insect's eyes when monitoring the sky , for instance, to provide an input bias to the on-chip memory concept shown in Figure5.21.

In the latter half of this thesis, through simulated works, we also demonstrated how the same optoelectronic components can be used in large and random assemblies to create several trainable ESN networks. While not perfect, their function after only a limited training time demonstrates close adherence to the chaotic time series they were trained on, in some cases nearly completely replicating the future data for a significant time after being set free. While we note that the smaller networks (N16, N32) were not capable of replicating both the temporal and amplitude components, they still produced an output whose frequency was similar to the time series, meaning their function may well still be adaptable to perform another task. Beyond which, in Paper III, we demonstrate an on-chip means to alter the broadcasting distribution in a linear NW network, by using combination of Yagi-Uda and asymmetric Yagi-Uda designs. This approach enables the creation of compact, light-communicating networks with tuneable connection strengths. Due to the directional nature of the antennas, nodes aligned in the forward direction will naturally still retain the relative magnitude of their weights. This results in locally clustered networks, whose configurations still remain highly functional, with the natural distribution appearing similar to those used successfully in [33] for the python based Stone model. To further enhance

near-field tuning, particularly in compact systems, iterative optimisation of antenna geometry and receiver alignment will be essential.

With the design of antenna structures being a largely iterative design, alternative approaches to achieving more control over the weight distribution should be looked into. For instance, instead of using a planar waveguide, an etchant could be used to retain only the area in which the network operates in, leaving an oxide-air interface at the edges of the network to keep signal strengths up. Furthermore, since light emission out of the NWs is cone-shaped, some of the emission will not interact with the antenna structure of its own NW, but rather its neighbours in densely packed neural node structures. Here, either Au reflectors around each NW, or holes etched in the waveguide between NWs can further improve interaction with the intended components. In simulations, it is possible to achieve exact dimensions and isotropy of etched material, so a refraction-based antenna using precisely shaped air gaps in the waveguide could also be tested. For network performance testing different weight distributions in models such as the python-based Stone model is an important way to study the usefulness of the networks. Furthermore, with the antenna director elements design being likened to that of evaporated structures, we have also demonstrated their potential as forward scattering elements that can be evaporated either during, or after, fabrication of our current devices to improve the signal transmission, the experimental performance of which should also be evaluated.

Taken together, these developments present the beginnings of a flexible and scalable platform for assembling complex NW-based optoelectronic systems. The ability to fabricate optically communicating components with high yield, embed responsive materials such as photochromic dyes, and design antenna structures to shape interconnectivity lays the groundwork for future work, both for biologically inspired, and physically trainable broadcasting networks. Aspects such as reliable memory integration, selective weighting, and adaptive response are now within reach, though further experimental exploration is needed. With the focus of ongoing efforts already set on completing the remainder components necessary for the realisation of a network inspired by the Stone model, all we need is time.

7.1 References

[1] G. E. Moore, 'Cramming more components onto integrated circuits', *Electronics*, vol. 38, 8 Apr. 1965.

[2] R. H. Dennard, F. H. Gaensslen, H. N. Yu, V. L. Rideout, E. Bassous and A. R. Leblanc, 'Design of ion-implanted mosfet's with very small physical dimensions', *IEEE Journal of Solid-State Circuits*, vol. 9, pp. 256–268, 5 1974, ISSN: 1558173X. DOI: 10.1109/JSSC.1974.1050511.

[3] B. Davari, R. H. Dennard and G. G. Shahidi, 'Cmos scaling for high performance and low power—the next ten years', *Proceedings of the IEEE*, vol. 83, pp. 595–606, 4 1995, ISSN: 15582256. DOI: 10.1109/5.371968.

[4] TSMC, *3nm technology*, 2025. https://www.tsmc.com/english/dedicatedFoundry/technology/logic.

[5] Samsung, *Optimized 3nm process achieves 45% reduced power usage, 23% improved performance and 16% smaller surface area compared to 5nm process*, Jun. 2022. https://news.samsung.com/global/samsung-begins-chip-production-using-3nm-process-technology-with-gaa-architecture.

[6] ASML, *Euv lithography systems*, 2023. https://www.asml.com/en/products/euv-lithography-systems.

[7] I. E. AGENCY, 'World energy outlook 2024', 2025.

[8] NVIDIA, *Programming tensor cores in cuda 9 | nvidia technical blog*, Oct. 2017. https://developer.nvidia.com/blog/programming-tensor-cores-cuda-9/.

[9] D. Marković, A. Mizrahi, D. Querlioz and J. Grollier, 'Physics for neuromorphic computing', *Nature Reviews Physics*, vol. 2, pp. 499–510, 9 Sep. 2020, ISSN: 25225820. DOI: 10.1038/s42254-020-0208-2.

[10] B. J. Shastri et al., 'Photonics for artificial intelligence and neuromorphic computing', *Nature Photonics*, vol. 15, pp. 102–114, 2 Feb. 2021, ISSN: 17494893. DOI: 10.1038/s41566-020-00754-y.

[11] P. R. Prucnal and B. J. Shastri, *Neuromorphic photonics*. CRC Press, 2017, p. 445, ISBN: 9781498725224.

[12] B. Shi, N. Calabretta and R. Stabile, 'Deep neural network through an inp soa-based photonic integrated cross-connect', *IEEE Journal of Selected Topics in Quantum Electronics*, vol. 26, 1 Jan. 2020, ISSN: 15584542. DOI: 10.1109/JSTQE.2019.2945548.

[13] Q. Zhang, H. Yu, M. Barbiero, B. Wang and M. Gu, 'Artificial neural networks enabled by nanophotonics', *Light: Science and Applications*, vol. 8, 1 Dec. 2019, ISSN: 20477538. DOI: 10.1038/s41377-019-0151-0.

[14] D. Winge, M. Borgström, E. Lind and A. Mikkelsen, 'Artificial nanophotonic neuron with internal memory for biologically inspired and reservoir network computing', *Neuromorphic Computing and Engineering*, vol. 3, 3 Sep. 2023, ISSN: 26344386. DOI: 10.1088/2634-4386/acf684.

[15] W. Shockley and W. T. Read, 'Statistics of the recombinations of holes and electrons', *Physical Review*, vol. 87, pp. 835–842, 5 1952, ISSN: 0031899X. DOI: 10.1103/PhysRev.87.835.

[16] G. E. Stillman, V. M. Robbins and N. Tabatabaie, 'Ill-v compound semiconductor devices: Optical detectors', *IEEE TRANSACTIONS ON ELECTRON DEVICES*, 11 1984.

[17] L. C. Andreani, A. Bozzola, P. Kowalczewski, M. Liscidini and L. Redorici, 'Silicon solar cells: Toward the efficiency limits', *Advances in Physics: X*, vol. 4, p. 1 548 305, 1 Jan. 2019, ISSN: 23746149. DOI: 10.1080/23746149.2018.1548305.

[18] N. R. E. Laboratory, *Best research-cell efficiency chart from photovoltaic research*, 2025. https://www.nrel.gov/pv/cell-efficiency.html.

[19] M. A. Green et al., 'Solar cell efficiency tables (version 63)', *Progress in Photovoltaics: Research and Applications*, vol. 32, pp. 3–13, 1 Jan. 2024, ISSN: 1099-159X. DOI: 10.1002/PIP.3750.

[20] S. Magdi, F. El-Diwany and M. A. Swillam, 'Broadband mir harvester using silicon nanostructures', *Scientific Reports*, vol. 9, 1 Dec. 2019, ISSN: 20452322. DOI: 10.1038/S41598-019-42022-2.

[21] L. Hrachowina, N. Anttu and M. T. Borgström, 'Wafer-scale synthesis and optical characterization of inp nanowire arrays for solar cells', *Nano Letters*, vol. 21, pp. 7347–7353, 17 Sep. 2021, ISSN: 15306992. DOI: 10.1021/acs.nanolett.1c02542.

[22] M. T. Borgström et al., 'In situ etching for total control over axial and radial nanowire growth', *Nano Research*, vol. 3, pp. 264–270, 4 Apr. 2010, ISSN: 19980000. DOI: 10.1007/s12274-010-1029-x.

[23] G. Otnes et al., 'Understanding inp nanowire array solar cell performance by nanoprobe-enabled single nanowire measurements', *Nano Letters*, vol. 18, pp. 3038–3046, 5 May 2018, ISSN: 15306992. DOI: 10.1021/acs.nanolett.8b00494.

[24] D. Alcer, M. Tirrito, L. Hrachowina and M. T. Borgström, 'Vertically processed gainp/inp tandem-junction nanowire solar cells', *ACS Applied Nano Materials*, vol. 7, pp. 2352–2358, 2 Jan. 2024, ISSN: 25740970. DOI: 10.1021/acsanm.3c05909.

[25] I. Mediavilla et al., 'Composition, optical resonances, and doping of inp/ingap nanowires for tandem solar cells: A micro-raman analysis', *ACS Nano*, vol. 18, pp. 10 113–10 123, 14 Apr. 2024, ISSN: 1936086X. DOI: 10.1021/acsnano.3c12973.

[26] M. Yao et al., 'Tandem solar cells using GaAs nanowires on si: Design, fabrication, and observation of voltage addition', *Nano Letters*, vol. 15, pp. 7217–7224, 11 Nov. 2015, ISSN: 15306992. DOI: 10.1021/acs.nanolett.5b03890.

[27] L. Hrachowina, Y. Chen, E. Barrigón, R. Wallenberg and M. T. Borgström, 'Realization of axially defined gainp/inp/inasp triple-junction photovoltaic nanowires for high-performance solar cells', *Materials Today Energy*, vol. 27, Jul. 2022, ISSN: 24686069. DOI: 10.1016/j.mtener.2022.101050.

[28] N. Yantara et al., 'Ion-mediated recombination dynamics in perovskite□based memory light-emitting diodes for neuromorphic control systems', *Advanced Materials*, Aug. 2023, ISSN: 0935-9648. DOI: 10.1002/adma.202305857.

[29] P. S. Tiwari et al., 'III–V infrared emitters on si: Fabrication concepts, device architectures and down-scaling with a focus on template-assisted selective epitaxy', *Semiconductor Science and Technology*, vol. 38, p. 053 001, 5 Apr. 2023, ISSN: 0268-1242. DOI: 10.1088/1361-6641/AC9F60.

[30] G. Badawy and E. P. Bakkers, *Electronic transport and quantum phenomena in nanowires*, Mar. 2024. DOI: 10.1021/acs.chemrev.3c00656.

[31] E. Prada et al., *From andreev to majorana bound states in hybrid superconductor–semiconductor nanowires*, Oct. 2020. DOI: 10.1038/s42254-020-0228-y.

[32] J. E. Sestoft et al., 'Shadowed versus etched superconductor-semiconductor junctions in al/inas nanowires', *Nano Letters*, vol. 24, pp. 8394–8401, 27 Jul. 2024, ISSN: 15306992. DOI: 10.1021/acs.nanolett.4c02055.

[33] D. O. Winge et al., 'Implementing an insect brain computational circuit using iii-v nanowire components in a single shared waveguide optical network', *ACS Photonics*, 2020, ISSN: 2330-4022. DOI: 10.1021/acsphotonics.0c01003.

[34] F. Ashtiani, A. J. Geers and F. Aflatouni, 'An on-chip photonic deep neural network for image classification', *Nature*, vol. 606, pp. 501–506, 7914 Jun. 2022, ISSN: 14764687. DOI: 10.1038/s41586-022-04714-0.

[35] X. Chen, B. Chen, P. Zhao, V. A. Roy, S. T. Han and Y. Zhou, 'Nanowire-based synaptic devices for neuromorphic computing', *Materials Futures*, vol. 2, 2 Jun. 2023, ISSN: 27525724. DOI: 10.1088/2752-5724/acc678.

[36] A. Loeffler et al., 'Neuromorphic learning, working memory, and metaplasticity in nanowire networks', *Science Advances*, vol. 9, 16 Apr. 2023.

[37] W. B. Levy and V. G. Calvert, 'Communication consumes 35 times more energy than computation in the human cortex, but both costs are needed to predict synapse number', *BIOPHYSICS AND COMPUTATIONAL BIOLOGY*, vol. 27, p. 2 008 173 118, 2021. DOI: 10.1073/pnas.2008173118.

[38] Q. Duan et al., 'Spiking neurons with spatiotemporal dynamics and gain modulation for monolithically integrated memristive neural networks', *Nature Communications*, vol. 11, 1 Dec. 2020, ISSN: 20411723. DOI: 10.1038/s41467-020-17215-3.

[39] B. Webb, 'Robots with insect brains', *Science*, vol. 368, pp. 244–245, 6488 Apr. 2020, ISSN: 10959203. DOI: 10.1126/SCIENCE.AAZ6869.

[40] T. Stone et al., 'An anatomically constrained model for path integration in the bee brain', *Current biology : CB*, vol. 27, 3069–3085.e11, 20 Oct. 2017, ISSN: 1879-0445. DOI: 10.1016/J.CUB.2017.08.052.

[41] B. Poucet and E. Save, 'Attractors in memory', *Science*, vol. 308, pp. 799–800, 5723 May 2005, ISSN: 00368075. DOI: 10.1126/science.111255.

[42] D. K. Gramotnev and S. I. Bozhevolnyi, 'Plasmonics beyond the diffraction limit', *Nature Photonics 2010 4:2*, vol. 4, pp. 83–91, 2 Jan. 2010, ISSN: 1749-4893. DOI: 10.1038/nphoton.2009.282.

[43] InsectNeuroNano, 'Insect-brain inspired neuromorphic nanophotonics', Apr. 2022. DOI: 10.3030/101046790.

[44] S. Sze and K. K. Ng, 'Physics of semiconductor devices', *Physics of Semiconductor Devices*, Oct. 2006. DOI: 10.1002/0470068329.

[45] D. Jena, *Quantum Physics of Semiconductor Materials and Devices*. Oxford University Press, May 2022, ISBN: 0198856849. DOI: 10.1093/oso/9780198856849.001.0001.

[46] V. S. Babu, *Solid State Devices and Technology*. 3rd Edition. Pearson, 2010, pp. 25–26.

[47] A. Chroneos, M. J. Rushton and R. W. Grimes, 'Fundamental point defect properties in ceramics', *Comprehensive Nuclear Materials: Volume 1-5*, vol. 1-5, pp. 47–64, Jan. 2012. DOI: 10.1016/B978-0-08-056033-5.00002-1.

[48] S. Morab, M. M. Sundaram and A. Pivrikas, 'Review on charge carrier transport in inorganic and organic semiconductors', *Coatings*, vol. 13, 9 Sep. 2023, ISSN: 20796412. DOI: 10.3390/COATINGS13091657.

[49] M. Wraback et al., 'Time-resolved electroabsorption measurement of the electron velocity-field characteristic in gan', *Applied Physics Letters*, vol. 76, pp. 1155–1157, 9 Feb. 2000, ISSN: 0003-6951. DOI: 10.1063/1.125968.

[50] C. J. Wort and R. S. Balmer, 'Diamond as an electronic material', *Materials Today*, vol. 11, pp. 22–28, 1-2 Jan. 2008, ISSN: 1369-7021. DOI: 10.1016/S1369-7021(07)70349-8.

[51] A. Yoshikawa, H. Matsunami and Y. Nanishi, 'Development and applications of wide bandgap semiconductors', *Wide Bandgap Semiconductors: Fundamental Properties and Modern Photonic and Electronic Devices*, pp. 1–24, 2007. DOI: 10.1007/978-3-540-47235-3_1.

[52] S. M. Sze and M. K. Lee, '3rd edition semiconductor devices physics and technology', 2012.

[53] P. S. Dutta, H. L. Bhat and V. Kumar, 'The physics and technology of gallium antimonide: An emerging optoelectronic material', *Journal of Applied Physics*, vol. 81, pp. 5821–5870, 9 May 1997, ISSN: 0021-8979. DOI: 10.1063/1.365356.

[54] R. J. Walters et al., 'Design of an achievable, all lattice-matched multijunction solar cell using ingaalassb', *Conference Record of the IEEE Photovoltaic Specialists Conference*, pp. 000 122–000 126, 2011, ISSN: 01608371. DOI: 10.1109/PVSC.2011.6185859.

[55] K. Masuko et al., 'Achievement of more than 25% conversion efficiency with crystalline silicon heterojunction solar cell', *IEEE Journal of Photovoltaics*, vol. 4, pp. 1433–1435, 6 Sep. 2014, ISSN: 21563381. DOI: 10.1109/JPHOTOV.2014.2352151.

[56] K. Yoshikawa et al., 'Silicon heterojunction solar cell with interdigitated back contacts for a photoconversion efficiency over 26%', *Nature Energy 2017 2:5*, vol. 2, pp. 1–8, 5 Mar. 2017, ISSN: 2058-7546. DOI: 10.1038/nenergy.2017.32.

[57] G. Chen et al., 'Optical antenna effect in semiconducting nanowires', *Nano Letters*, vol. 8, pp. 1341–1346, 5 May 2008, ISSN: 15306984. DOI: 10.1021/nl080007v.

[58] J. Wang, M. S. Gudiksen, X. Duan, Y. Cui and C. M. Lieber, 'Highly polarized photoluminescence and photodetection from single indium phosphide nanowires', *Science*, vol. 293, pp. 1455–1457, 5534 Aug. 2001, ISSN: 00368075. DOI: 10.1126/science.1062340.

[59] W. Shockley, 'The theory of p-n junctions in semiconductors and p-n junction transistors', Tech. Rep., Jul. 1949.

[60] K. G. Mckwv, 'Avalanche breakdown in silicon', 1954.

[61] C. T. Sah, R. N. Noyce and W. Shockley, 'Carrier generation and recombination in p-n junctions and p-n junction characteristics', *Proceedings of the IRE*, vol. 45, pp. 1228–1243, 9 1957, ISSN: 00968390. DOI: 10.1109/JRPROC.1957.278528.

[62] A. Karabchevsky, A. Katiyi, A. S. Ang and A. Hazan, 'On-chip nanophotonics and future challenges', *Nanophotonics*, vol. 9, pp. 3733–3753, 12 Sep. 2020, ISSN: 21928614. DOI: 10.1515/nanoph-2020-0204.

[63] A. Higuera-Rodriguez et al., 'Ultralow surface recombination velocity in passivated ingaas/inp nanopillars', *Nano Letters*, vol. 17, pp. 2627–2633, 4 Apr. 2017, ISSN: 15306992. DOI: 10.1021/acs.nanolett.7b00430.

[64] F. Patolsky and C. M. Lieber, 'Nanowire nanosensors', *Materials Today*, vol. 8, pp. 20–28, 4 Apr. 2005, ISSN: 1369-7021. DOI: 10.1016/S1369-7021(05)00791-1.

[65] M. Berg, K. M. Persson, J. Wu, E. Lind, H. Sjöland and L. E. Wernersson, 'Inas nanowire mosfets in three-transistor configurations: Single balanced rf down-conversion mixers', *Nanotechnology*, vol. 25, p. 485 203, 48 Nov. 2014, ISSN: 0957-4484. DOI: 10.1088/0957-4484/25/48/485203.

[66] C. Zhang and X. Li, 'Iii-v nanowire transistors for low-power logic applications: A review and outlook', *IEEE Transactions on Electron Devices*, vol. 63, pp. 223–234, 1 Jan. 2016, ISSN: 00189383. DOI: 10.1109/TED.2015.2498923.

[67] B. Monemar, B. J. Ohlsson, N. F. Gardner and L. Samuelson, 'Nanowire-based visible light emitters, present status and outlook', *Semiconductors and Semimetals*, vol. 94, pp. 227–271, Jan. 2016, ISSN: 0080-8784. DOI: 10.1016/BS.SEMSEM.2015.10.002.

[68] M. Liu, M. Jiang, Y. Liu, K. Tang, D. N. Shi and C. Kan, 'Wavelength-tunable green light sources based on zno:ga nanowire/p-ingan heterojunctions', *ACS Applied Nano Materials*, vol. 4, pp. 11 168–11 179, 10 Oct. 2021, ISSN: 25740970. DOI: 10.1021/acsanm.1c02650.

[69] N. Anttu, 'Shockley-queisser detailed balance efficiency limit for nanowire solar cells', *ACS Photonics*, vol. 2, pp. 446–453, 3 Mar. 2015, ISSN: 23304022. DOI: 10.1021/ph5004835.

[70] J. Wallentin et al., 'Inp nanowire array solar cells achieving 13.8% efficiency by exceeding the ray optics limit', *Science*, vol. 339, pp. 1057–1060, 6123 Mar. 2013, ISSN: 10959203. DOI: 10.1126/science.1230969.

[71] Z. Zhong et al., 'Efficiency enhancement of axial junction inp single nanowire solar cells by dielectric coating', *Nano Energy*, vol. 28, pp. 106–114, Oct. 2016, ISSN: 2211-2855. DOI: 10.1016/J.NANOEN.2016.08.032.

[72] L. Hrachowina, Y. Zhang, A. Saxena, G. Siefer, E. Barrigon and M. T. Borgstrom, 'Development and characterization of a bottom-up inp nanowire solar cell with 16.7% efficiency', in *Conference Record of the IEEE Photovoltaic Specialists Conference*, vol. 2020-June, Institute of Electrical and Electronics Engineers Inc., Jun. 2020, pp. 1754–1756, ISBN: 9781728161150. DOI: 10.1109/PVSC45281.2020.9300394.

[73] M. T. Borgström et al., 'Towards nanowire tandem junction solar cells on silicon', *IEEE Journal of Photovoltaics*, vol. 8, pp. 733–740, 3 May 2018, ISSN: 21563381. DOI: 10.1109/JPHOTOV.2018.2816264.

[74] H. Yang et al., 'Nanowire network–based multifunctional all-optical logic gates', *Science Advances*, vol. 4, pp. 7954–7981, 7 Jul. 2018, ISSN: 23752548. DOI: 10.1126/sciadv.aar7954.

[75] P. Espinet-Gonzalez et al., 'Nanowire solar cells: A new radiation hard pv technology for space applications', *IEEE Journal of Photovoltaics*, vol. 10, pp. 502–507, 2 Mar. 2020, ISSN: 21563403. DOI: 10.1109/JPHOTOV.2020.2966979.

[76] M. T. Borgström et al., 'Precursor evaluation for in situ inp nanowire doping', *Nanotechnology*, vol. 19, 44 Nov. 2008, ISSN: 09574484. DOI: 10.1088/0957-4484/19/44/445602.

[77] D. Alcer, L. Hrachowina, D. Hessman and M. T. Borgström, 'Processing and characterization of large area inp nanowire photovoltaic devices', *Nanotechnology*, vol. 34, p. 295 402, 29 May 2023, ISSN: 0957-4484. DOI: 10.1088/1361-6528/ACCC37.

[78] H. J. Joyce et al., 'Electronic properties of gaas, inas and inp nanowires studied by terahertz spectroscopy', *Nanotechnology*, vol. 24, 21 May 2013, ISSN: 13616528. DOI: 10.1088/0957-4484/24/21/214006.

[79] S. A. Dayeh, C. Soci, P. K. L. Yu, E. T. Yu and D. Wang, 'Transport properties of inas nanowire field effect transistors: The effects of surface states', *Journal of Vacuum Science and Technology B: Microelectronics and Nanometer Structures Processing, Measurement, and Phenomena*, vol. 25, pp. 1432–1436, 4 Jul. 2007, ISSN: 1071-1023. DOI: 10.1116/1.2748410.

[80] R. Shen et al., 'Artificial synapse based on an inas nanowire field-effect transistor with ferroelectric polymer p(vdf-trfe) passivation', *ACS Applied Electronic Materials*, vol. 4, pp. 5008–5016, 10 Oct. 2022, ISSN: 26376113. DOI: 10.1021/acsaelm.2c01005.

[81] K. Redmond, *Nov. 16, 1904: John ambrose fleming patents the vacuum tube*, 2024. https://www.aps.org/apsnews/2024/10/ambrose-fleming-patents-vacuum-tube.

[82] J. S. Kilby, 'Invention of the integrated circuit', *IEEE Transactions on Electron Devices*, vol. 23, pp. 648–654, 7 1976, ISSN: 15579646. DOI: 10.1109/T-ED.1976.18467.

[83] H. W. Ballou, 'Microphotography, photography and photofabrication at extreme resolution. 1968. g. w. w. stevens. wiley, inc., n.y. 2nd ed. 510 pp.', *American Documentation*, vol. 20, pp. 283–284, 3 Jul. 1969, ISSN: 0096-946X. DOI: 10.1002/ASI.4630200321.

[84] P. B. Meggs and A. W. Purvis, *Meggs' History of Graphic Design Fourth Edition*. 2006, ISBN: 9780471699026.

[85] M. Köfferlein, *KLayout*, Jan. 2018. https://github.com/KLayout/klayout.

[86] L. D. Nanolab, *Specific process knowledge/thin film deposition/deposition of zinc*, 2023. https://labadviser.nanolab.dtu.dk/index.php?title=Specific_Process_Knowledge/Thin_film_deposition/Deposition_of_Zinc.

[87] K. Shubham and A. Gupta, *Integrated Circuit Fabrication*. CRC Press, Feb. 2021, ISBN: 9781003178583. DOI: 10.1201/9781003178583.

[88] H. Instruments, *Mla 150 advanced maskless aligner*, 2015. https://heidelberg-instruments.com/product/mla150/.

[89] H. Ahn et al., 'Integrated 1d epitaxial mirror twin boundaries for ultrascaled 2d mos2 field-effect transistors', *Nature Nanotechnology*, vol. 19, pp. 955–961, 7 Jul. 2024, ISSN: 17483395. DOI: 10.1038/s41565-024-01706-1.

[90] J. Robertson, 'High dielectric constant oxides', *The European Physical Journal Applied Physics*, vol. 28, pp. 265–291, 3 Dec. 2004, ISSN: 1286-0042. DOI: 10.1051/EPJAP:2004206.

[91] W. Tsai et al., 'Performance comparison of sub 1 nm sputtered tin/hfo2 nmos and pmosfets', *Technical Digest - International Electron Devices Meeting*, pp. 311–314, 2003, ISSN: 01631918. DOI: 10.1109/IEDM.2003.1269287.

[92] J. Robertson and R. M. Wallace, 'High-k materials and metal gates for cmos applications', *Materials Science and Engineering: R: Reports*, vol. 88, pp. 1–41, Feb. 2015, ISSN: 0927-796X. DOI: 10.1016/J.MSER.2014.11.001.

[93] M. Broas, O. Kanninen, V. Vuorinen, M. Tilli and M. Paulasto-Kröckel, 'Chemically stable atomic-layer-deposited al2o3 films for processability', *ACS Omega*, vol. 2, pp. 3390–3398, 7 Jul. 2017, ISSN: 24701343. DOI: 10.1021/acsomega.7b00443.

[94] E. G. Lizarraga-Medina et al., 'Optical waveguides fabricated in atomic layer deposited al2o3 by ultrafast laser ablation', *Results in Optics*, vol. 2, p. 100 060, Jan. 2021, ISSN: 2666-9501. DOI: 10.1016/J.RIO.2021.100060.

[95] N. Dsouza et al., 'Silicon surface passivation of industrial n-type cz si (111) by al2o3 layers deposited by thermal ald process for application in carrier selective contact solar cells', *Journal of Materials Science: Materials in Electronics*, vol. 34, pp. 1–9, 14 May 2023, ISSN: 1573482X. DOI: 10.1007/S10854-023-10587-4/TABLES/2.

[96] G. G. Politano and C. Versace, 'Spectroscopic ellipsometry: Advancements, applications and future prospects in optical characterization', *Spectroscopy Journal*, vol. 1, pp. 163–181, 3 Dec. 2023. DOI: 10.3390/SPECTROSCJ1030014.

[97] G. G. Politano and C. Versace, 'Spectroscopic ellipsometry: Advancements, applications and future prospects in optical characterization', *Spectroscopy Journal 2023, Vol. 1, Pages 163-181*, vol. 1, pp. 163–181, 3 Dec. 2023, ISSN: 2813-446X. DOI: 10.3390/SPECTROSCJ1030014.

[98] A. Ballato and J. Ballato, 'Sellmeier circuits: A unifying view on optical and plasma dispersion fitting formulas', *Journal of Applied Physics*, vol. 128, p. 34 901, 3 Jul. 2020, ISSN: 10897550. DOI: 10.1063/5.0015282/157742.

[99] A. Ribner, *Obtaining molecularly clean surfaces by plasma processing*, 1992. https://www.plasmapreen.com/Literature.

[100] Y. J. Hung, S. L. Lee, B. J. Thibeault and L. A. Coldren, 'Fabrication of highly ordered silicon nanowire arrays with controllable sidewall profiles for achieving low-surface reflection', *IEEE Journal on Selected Topics in Quantum Electronics*, vol. 17, pp. 869–877, 4 Jul. 2011, ISSN: 1077260X. DOI: 10.1109/JSTQE.2010.2068540.

[101] F. J. Wendisch, M. Rey, N. Vogel and G. R. Bourret, 'Large-scale synthesis of highly uniform silicon nanowire arrays using metal-assisted chemical etching', *Chemistry of Materials*, vol. 32, pp. 9425–9434, 21 Nov. 2020, ISSN: 15205002. DOI: 10.1021/acs.chemmater.0c03593.

[102] C. Chartier, S. Bastide and C. Lévy-Clément, 'Metal-assisted chemical etching of silicon in hf–h2o2', *Electrochimica Acta*, vol. 53, pp. 5509–5516, 17 Jul. 2008, ISSN: 0013-4686. DOI: 10.1016/J.ELECTACTA.2008.03.009.

[103] D. Alcer, A. P. Saxena, L. Hrachowina, X. Zou, A. Yartsev and M. T. Borgström, 'Comparison of triethylgallium and trimethylgallium precursors for gainp nanowire growth', *physica status solidi (b)*, vol. 258, p. 2 000 400, 2 Feb. 2021, ISSN: 1521-3951. DOI: 10.1002/PSSB.202000400.

[104] M. D. Lafontaine et al., 'Anisotropic and low damage iii-v/ge heterostructure etching for multijunction solar cell fabrication with passivated sidewalls', 2021. DOI: 10.1016/j.mne.2021.100083.

[105] N. Karam, C. Fetzer, X.-Q. Liu, M. Steiner and K. Schulte, 'Metamorphic growth and multijunction iii-v solar cells', *Metalorganic Vapor Phase Epitaxy (MOVPE)*, pp. 149–173, Oct. 2019. DOI: 10.1002/9781119313021.CH5.

[106] B. Pal, K. J. Sarkar and P. Banerji, 'Fabrication and studies on si/inp core-shell nanowire based solar cell using etched si nanowire arrays', 2019. DOI: 10.1016/j.solmat.2019.110217.

[107] W. Q. Wei et al., 'Monolithic integration of embedded iii-v lasers on soi', *Light: Science and Applications*, vol. 12, pp. 1–11, 1 Dec. 2023, ISSN: 20477538. DOI: 10.1038/s41377-023-01128-z.

[108] D. M. Sullivan, *Electromagnetic Simulation Using the FDTD Method*. Wiley-IEEE Press, 2000, ISBN: 9780470544518.

[109] J. Dorfmüller et al., 'Near-field dynamics of optical yagi-uda nanoantennas', *Nano Letters*, vol. 11, pp. 2819–2824, 7 Jul. 2011, ISSN: 15306984. DOI: 10.1021/nl201184n.

[110] F. Xu, Y. Zhang, W. Hong, K. Wu and T. J. Cui, 'Finite-difference frequency-domain algorithm for modeling guided-wave properties of substrate integrated waveguide', *IEEE Transactions on Microwave Theory and Techniques*, vol. 51, pp. 2221–2227, 11 Nov. 2003, ISSN: 00189480. DOI: 10.1109/TMTT.2003.818935.

[111] F. L. Teixeira et al., 'Finite-difference time-domain methods', *Nature Reviews Methods Primers*, vol. 3, 1 Oct. 2023. DOI: 10.1038/s43586-023-00257-4.

[112] ANSYS, *Finite difference time domain (fdtd) solver introduction*, 2024. https://optics.ansys.com/hc/en-us/articles/360034914633-Finite-Difference-Time-Domain-FDTD-solver-introduction.

[113] W. Yu and R. Mittra, 'A conformal finite difference time domain technique for modeling curved dielectric surfaces', *IEEE Microwave and Wireless Components Letters*, vol. 11, pp. 25–27, 1 Jan. 2001, ISSN: 15311309. DOI: 10.1109/7260.905957.

[114] E. D. Palik, 'Handbook of optical constants of solids', *Handbook of Optical Constants of Solids*, vol. 1, pp. 1–804, Dec. 2012. DOI: 10.1016/C2009-0-20920-2.

[115] J. P. Bérenger, 'Perfectly matched layer (pml) for computational electromagnetics', *Synthesis Lectures on Computational Electromagnetics*, vol. 8, pp. 1–120, Jan. 2007, ISSN: 19321252. DOI: 10.2200/S00030ED1V01Y200605CEM008.

[116] G. Mie, 'Beiträge zur optik trüber medien, speziell kolloidaler metallösungen', *Annalen der Physik*, vol. 330, pp. 377–445, 3 Jan. 1908, ISSN: 1521-3889. DOI: 10.1002/ANDP.19083300302.

[117] R. Paniagua-Dominguez, B. Luk'yanchuk and A. I. Kuznetsov, *Control of scattering by isolated dielectric nanoantennas*. Elsevier, Jan. 2019, pp. 73–108, ISBN: 9780081024034. DOI: 10.1016/B978-0-08-102403-4.00008-6.

[118] W. Liu and Y. S. Kivshar, 'Generalized kerker effects in nanophotonics and meta-optics [invited]', *Optics Express*, vol. 26, p. 13 085, 10 May 2018, ISSN: 10944087. DOI: 10.1364/oe.26.013085.

[119] F. Vidar, *Lumerical FDTD Scripting Tools*, Feb. 2025. https://github.com/DeltaMod/Lumerical_FDTD_Scripting_Tools.

[120] F. Vidar, *DeltaMod Utilities (DMU)*, Jan. 2022. https://github.com/DeltaMod/DMU.

[121] N. Lamers, K. Adham, L. Hrachowina, M. T. Borgström and J. Wallentin, 'Single vertical inp nanowire diodes with low ideality factors contacted in-array for high-resolution optoelectronics', *Nanotechnology*, vol. 36, 07LT01, 7 Dec. 2024. DOI: 10.1088/1361-6528/ad96c3.

[122] T. Y. Chang, H. Kim, B. T. Zutter, W. J. Lee, B. C. Regan and D. L. Huffaker, 'Orientation-controlled selective-area epitaxy of iii–v nanowires on (001) silicon for silicon photonics', *Advanced Functional Materials*, vol. 30, p. 2 002 220, 30 Mar. 2020, ISSN: 1616-3028. DOI: 10.1002/ADFM.202002220.

[123] H. Kato, S. Sakita and S. Hara, 'Selective-area growth and magnetic characterization of lateral mnas nanowires', *Journal of Crystal Growth*, vol. 414, pp. 151–155, Mar. 2015, ISSN: 0022-0248. DOI: 10.1016/J.JCRYSGRO.2014.09.020.

[124] G. Yu, A. Cao and C. M. Lieber, 'Large-area blown bubble films of aligned nanowires and carbon nanotubes', 2007. DOI: 10.1038/nnano.2007.150.

[125] S. Wu et al., 'Soluble polymer-based, blown bubble assembly of single- and double-layer nanowires with shape control', *ACS Nano*, vol. 8, pp. 3522–3530, 4 Mar. 2014, ISSN: 1936086X. DOI: 10.1021/nn406610d.

[126] J. Park, G. Shin and J. S. Ha, 'Controlling orientation of v2o5 nanowires within micropatterns via microcontact printing combined with the gluing langmuir–blodgett technique', *IOP PUBLISHING NANOTECHNOLOGY Nanotechnology*, vol. 19, p. 6, 2008. DOI: 10.1088/0957-4484/19/39/395303.

[127] A. Tao et al., 'Langmuir-blodgett silver nanowire monolayers for molecular sensing using surface-enhanced raman spectroscopy', *Nano Letters*, vol. 3, pp. 1229–1233, 9 Sep. 2003, ISSN: 15306984. DOI: 10.1021/nl0344209.

[128] D. Whang, S. Jin, Y. Wu and C. M. Lieber, 'Large-scale hierarchical organization of nanowire arrays for integrated nanosystems', *Nano Letters*, vol. 3, pp. 1255–1259, 9 Sep. 2003, ISSN: 15306984. DOI: 10.1021/NL0345062.

[129] Y. Huang, X. Duan, Q. Wei and C. M. Lieber, 'Directed assembly of one-dimensional nanostructures into functional networks', *Science*, vol. 291, pp. 630–633, 5504 Jan. 2001, ISSN: 00368075. DOI: 10.1126/SCIENCE.291.5504.630.

[130] X. Duan et al., 'High-performance thin-film transistors using semiconductor nanowires and nanoribbons', *Nature 2003 425:6955*, vol. 425, pp. 274–278, 6955 Sep. 2003, ISSN: 1476-4687. DOI: 10.1038/nature01996.

[131] C. Borschel et al., 'A new route toward semiconductor nanospintronics: Highly mn-doped gaas nanowires realized by ion-implantation under dynamic annealing conditions', *Nano Letters*, vol. 11, pp. 3935–3940, 9 Mar. 2011, ISSN: 15306984. DOI: doi.org/10.1021/nl2021653.

[132] C. M. Hangarter, Y. Rheem, B. Yoo, E. H. Yang and N. V. Myung, 'Hierarchical magnetic assembly of nanowires', *Nanotechnology*, vol. 18, 20 Apr. 2007, ISSN: 09574484. DOI: 10.1088/0957-4484/18/20/205305.

[133] K. Heo et al., 'Large-scale assembly of silicon nanowire network-based devices using conventional microfabrication facilities', *Nano Letters*, vol. 8, pp. 4523–4527, 12 Dec. 2008, ISSN: 15306984. DOI: 10.1021/NL802570M.

[134] M. Liu et al., 'Self-assembled magnetic nanowire arrays', 2007. DOI: 10.1063/1.2711522.

[135] M. Sam, N. Moghimian and R. B. Bhiladvala, 'Field-directed assembly of nanowires: Identifying directors, disruptors and indices to maximize the device yield', *Nanoscale*, vol. 8, pp. 889–900, 2 Jan. 2016, ISSN: 20403372. DOI: 10.1039/c5nr06763d.

[136] K. Oh, J. H. Chung, J. J. Riley, Y. Liu and W. K. Liu, 'Fluid flow-assisted dielectrophoretic assembly of nanowires', *Langmuir*, vol. 23, pp. 11 932–11 940, 23 Mar. 2007, ISSN: 07437463. DOI: doi.org/10.1021/la701755s.

[137] T. Krishnamoorthy et al., 'A facile route to vertically aligned electrospun sno 2 nanowires on a transparent conducting oxide substrate for dye-sensitized solar cells', *Journal of Materials Chemistry*, vol. 22, pp. 2166–2172, 5 Feb. 2012, ISSN: 09599428. DOI: 10.1039/c1jm15047b.

[138] K. Mølhave, T. Wich, A. Kortschack and P. Bøggild, 'Pick-and-place nanomanipulation using microfabricated grippers', *Nanotechnology*, vol. 17, pp. 2434–2441, 10 May 2006, ISSN: 09574484. DOI: 10.1088/0957-4484/17/10/002.

[139] M. Khalilian et al., 'Dislocation-free and atomically flat gan hexagonal microprisms for device applications', *Small*, vol. 16, p. 1 907 364, 30 Jul. 2020, ISSN: 16136829. DOI: 10.1002/smll.201907364.

[140] J. Colvin et al., 'Surface and dislocation investigation of planar gan formed by crystal reformation of nanowire arrays', *Physical Review Materials*, vol. 3, p. 093 604, 9 Sep. 2019, ISSN: 24759953. DOI: 10.1103/PhysRevMaterials.3.093604.

[141] Y.-P. Liu, 'Surfaces and interfaces of low dimensional iii-v semiconductor devices', Ph.D. dissertation, Sep. 2022, ISBN: 978-91-8039-399-7.

[142] M. Hugenschmidt, K. Adrion, A. Marx, E. Müller and D. Gerthsen, 'Electron-beam-induced carbon contamination in stem-in-sem: Quantification and mitigation', *Microscopy and Microanalysis*, vol. 29, pp. 219–234, 1 Mar. 2023, ISSN: 1431-9276. DOI: 10.1093/MICMIC/OZAC003.

[143] M. A. Jepson, K. Khan, T. J. Hayward, B. J. Inkson and C. Rodenburg, 'The effect of oxidation and carbon contamination on sem dopant contrast', *Journal of Physics: Conference Series*, vol. 241, p. 012 078, 1 Jul. 2010, ISSN: 1742-6596. DOI: 10.1088/1742-6596/241/1/012078.

[144] J. Hwang et al., 'Wafer-scale alignment and integration of micro-light-emitting diodes using engineered van der waals forces', *Nature Electronics*, vol. 6, pp. 216–224, 3 Mar. 2023, ISSN: 25201131. DOI: 10.1038/s41928-022-00912-w.

[145] M. Löw, M. Guidat, J. Kim and M. M. May, 'The interfacial structure of inp(100) in contact with hcl and h2so4 studied by reflection anisotropy spectroscopy', *RSC Advances*, vol. 12, pp. 32 756–32 764, 50 Nov. 2022, ISSN: 20462069. DOI: 10.1039/d2ra05159a.

[146] M. Schvartzman, V. Sidorov, D. Ritter and Y. Paz, 'Passivation of inp surfaces of electronic devices by organothiolated self-assembled monolayers', *Journal of Vacuum Science and Technology B: Microelectronics and Nanometer Structures*, vol. 21, p. 148, 1 2003, ISSN: 0734211X. DOI: 10.1116/1.1532026.

[147] D. H. van Dorp, D. Cuypers, S. Arnauts, A. Moussa, L. Rodriguez and S. D. Gendt, 'Wet chemical etching of inp for cleaning applications', *ECS Journal of Solid State Science and Technology*, vol. 2, P190–P194, 4 2013, ISSN: 2162-8769. DOI: 10.1149/2.025304JSS.

[148] S. Adachi and H. Kawaguchi, 'Chemical etching characteristics of (001) inp', *Journal of The Electrochemical Society*, vol. 128, pp. 1342–1349, 6 Jun. 1981, ISSN: 0013-4651. DOI: 10.1149/1.2127633/XML.

[149] S. Hwang, J. Shim and Y. Eo, 'Ohmic contacts of pd/zn/m(= pd or pt)/au to p-type inp', Tech. Rep., 2005, pp. 751–755.

[150] T. Haggren et al., 'Inp nanowire p-type doping via zinc indiffusion', *Journal of Crystal Growth*, vol. 451, pp. 18–26, Oct. 2016, ISSN: 00220248. DOI: 10.1016/j.jcrysgro.2016.06.020.

[151] K. Zhang, H. Tang, X. Wu, J. Xu, X. Li and H. Gong, 'Improved au/zn/au ohmic contacts for p -type inp', in *International Symposium on Photoelectronic Detection and Imaging 2007: Photoelectronic Imaging and Detection*, vol. 6621, SPIE, Sep. 2007, p. 662 118, ISBN: 9780819467638. DOI: 10.1117/12.790778.

[152] M.-H. Park, L. C. Wang, J. Y. Cheng and C. J. Palmstro, 'Low resistance ohmic contact scheme to p-inp', *Applied Physics Letters*, vol. 70, 1 Jan. 1997.

[153] A. G. Baca, F. Ren, J. C. Zolper, R. D. Briggs and S. J. Pearton, 'A survey of ohmic contacts to iii-v compound semiconductors', Tech. Rep.

[154] M. Samavat, T. M. Bartol, K. M. Harris and T. J. Sejnowski, 'Synaptic information storage capacity measured with information theory', *Neural Computation*, vol. 36, pp. 781–802, 5 May 2024, ISSN: 1530888X. DOI: 10.1162/neco_a_01659.

[155] E. Barrigón, L. Hrachowina and M. T. Borgström, 'Light current-voltage measurements of single, as-grown, nanowire solar cells standing vertically on a substrate', *Nano Energy*, vol. 78, Dec. 2020, ISSN: 22112855. DOI: 10.1016/j.nanoen.2020.105191.

[156] G. Otnes et al., 'Understanding inp nanowire array solar cell performance by nanoprobe-enabled single nanowire measurements', *Nano Letters*, vol. 18, pp. 3038–3046, 5 May 2018, ISSN: 15306992. DOI: 10.1021/acs.nanolett.8b00494.

[157] D. Sharma, D. Rao and B. Saha, 'A photonic artificial synapse with a reversible multifaceted photochromic compound † new concepts nanoscale horizons', *Nanoscale Horiz*, vol. 8, pp. 543–549, 2023. DOI: 10.1039/d2nh00532h.

[158] L. R. Schomaker, 'A neural oscillator-network model of temporal pattern generation', *Human Movement Science*, vol. 11, pp. 181–192, 1-2 Feb. 1992, ISSN: 0167-9457. DOI: 10.1016/0167-9457(92)90059-K.

[159] H. Jaeger and H. Haas, 'Harnessing nonlinearity: Predicting chaotic systems and saving energy in wireless communication', *Science*, vol. 304, pp. 78–80, 5667 Apr. 2004, ISSN: 00368075. DOI: 10.1126/science.1091277.

[160] M. Lukoševičius, 'A practical guide to applying echo state networks', *Springer*, Neural Networks: Tricks of the Trade, Reloaded 2012.

[161] M. Lukoševičius and H. Jaeger, 'Reservoir computing approaches to recurrent neural network training', *Computer Science Review*, vol. 3, pp. 127–149, 3 Aug. 2009, ISSN: 1574-0137. DOI: 10.1016/J.COSREV.2009.03.005.

[162] R. K. Daniels, J. B. Mallinson, Z. E. Heywood, P. J. Bones, M. D. Arnold and S. A. Brown, 'Reservoir computing with 3d nanowire networks', *Neural Networks*, vol. 154, pp. 122–130, Oct. 2022, ISSN: 0893-6080. DOI: 10.1016/J.NEUNET.2022.07.001.

[163] Z. Kuncic and T. Nakayama, 'Neuromorphic nanowire networks: Principles, progress and future prospects for neuro-inspired information processing', *Advances in Physics: X*, vol. 6, 1 2021, ISSN: 23746149. DOI: 10.1080/23746149.2021.1894234.

[164] R. Zhu et al., 'Online dynamical learning and sequence memory with neuromorphic nanowire networks', *Nature Communications*, vol. 14, 1 Dec. 2023, ISSN: 20411723. DOI: 10.1038/s41467-023-42470-5.

[165] M. C. Mackey and L. Glass, 'Oscillation and chaos in physiological control systems', *Science*, vol. 197, pp. 287–289, 4300 1977, ISSN: 00368075. DOI: 10.1126/SCIENCE.267326.

[166] M. Mohri, A. Rostamizadeh and A. Talwalkar, *Foundations of Machine Learning: Second Edition*, F. Bach, Ed. MIT Press, 2018.

[167] C. Korndörfer, *pyESN*, Apr. 2020. https://github.com/cknd/pyESN.

[168] S. Uda, *On the Wireless Beam of Short Electric Waves*. Institute of electrical engineers of Japan, 1927, vol. 20.

[169] T. Kosako, Y. Kadoya and H. F. Hofmann, 'Directional control of light by a nano-optical yagi–uda antenna', *Nature Photonics 2010 4:5*, vol. 4, pp. 312–315, 5 Mar. 2010, ISSN: 1749-4893. DOI: 10.1038/nphoton.2010.34.

[170] X. Y. Xiong, L. J. Jiang, W. E. Sha, Y. H. Lo and W. C. Chew, 'Compact nonlinear yagi-uda nanoantennas', *Scientific Reports*, vol. 6, pp. 1–9, January 2016, ISSN: 20452322. DOI: 10.1038/srep18872.

[171] M. Ramezani et al., 'Hybrid semiconductor nanowire-metallic yagi-uda antennas', *Nano Letters*, vol. 15, pp. 4889–4895, 8 Aug. 2015, ISSN: 15306992. DOI: 10.1021/ACS.NANOLETT.5B00565.

[172] W. Rieger, J. J. Heremans, H. Ruan, Y. Kang and R. Claus, 'Yagi-uda nanoantenna enhanced metal-semiconductor-metal photodetector', *Applied Physics Letters*, vol. 113, 2 Jul. 2018, ISSN: 00036951. DOI: 10.1063/1.5038339.

[173] X. Ni, N. K. Emani, A. V. Kildishev, A. Boltasseva and V. M. Shalaev, 'Broadband light bending with plasmonic nanoantennas', *Science*, vol. 335, p. 427, 6067 Jan. 2012, ISSN: 10959203. DOI: 10.1126/science.1214686.

[174] N. Yu et al., 'Light propagation with phase discontinuities: Generalized laws of reflection and refraction', *Science*, vol. 334, pp. 333–337, 6054 Oct. 2011, ISSN: 10959203. DOI: 10.1126/science.1210713.

[175] G. Banerjee and R. L. Rhoades, 'Chemical mechanical planarization historical review and future direction', *ECS Transactions*, vol. 13, pp. 1–19, 4 Oct. 2008, ISSN: 1938-5862. DOI: 10.1149/1.2912973/XML.

[176] A. Andrishak, B. Jacob, T. L. Alves, C. Maibohm, B. Romeira and J. B. Nieder, 'Free-standing millimeter-range 3d waveguides for on-chip optical interconnects', *Scientific Reports*, vol. 14, pp. 1–9, 1 Dec. 2024, ISSN: 20452322. DOI: https://doi.org/10.1038/s41598-024-69522-0.

Printed by Media-Tryck, Lund 2025 NORDIC SWAN ECOLABEL 3041 0903

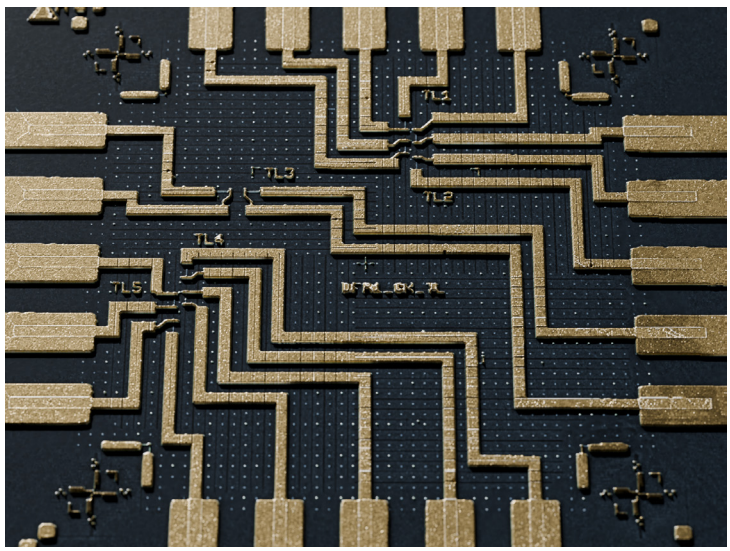

LUND UNIVERSITY

Faculty of Science
Department of Physics

ISBN 978-91-8104-555-0

9 789181 045550